Utilising autophagy modulation to combat cell death resistance in Glioblastoma Multiforme

by

Jurgen Andries Kriel

Thesis presented in fulfilment of requirements for the degree of Master of Science in the Faculty of Science at Stellenbosch University

Supervisor: Dr Benjamin Loos

Co-supervisor: Prof Kristian Müller-Nedebock

December 2016

Declaration

By submitting this thesis electronically, I declare that the entirety of the work contained therein is my own, original work, that I am the sole author thereof (save to the extent explicitly otherwise stated), that reproduction and publication thereof by Stellenbosch University will not infringe any third party rights and that I have not previously in its entirety or in part submitted it for obtaining any qualification.

....
Signature

December 2016

Abstract

Introduction: Globally, Glioblastoma Multiforme (GBM) presents as both the most prevalent and invasive form of Central Nervous System (CNS) malignancy. Patient life expectancy has remained largely unchanged over the past three decades, with a mean survival time of only 15 months. Although many advances have been made in understanding the molecular pathogenesis of GBM, the clinical treatment regimen has not been improved upon. One major commonality between all gliomas is their excessive energy requirements to uphold proliferation. The GBM metabolic profile has been shown to comprise of both oxidative phosphorylation (OXPHOS) and aerobic glycolysis. Moreover, the protein degradation pathway known as autophagy has proved to uphold tumour survival in nutrient limiting conditions. Autophagy modulators have therefore shown much promise to act as adjuvants to chemotherapy, although determining the degree of inhibition and or induction necessary to achieve sensitisation remains a major challenge. We, therefore, hypothesised that glioma cells can be sensitised to undergo cell death by modulating autophagy in order to decrease bioenergetic efficiency and enhance susceptibility to chemotherapy. The aims were thus to: (i) determine the amount of autophagy modulation necessary to sensitise glioma cells to chemotherapy; (ii) assess mitochondrial bioenergetics in terms of topology, dynamics and electron transport system efficiency; (iii) determine the extent of diminished mitochondrial capacity necessary to achieve cell death sensitisation

Methods: An *in vitro* model of GBM was employed utilising the U-118MG glioblastoma cell line. Chemical autophagy modulation was achieved by utilising Rapamycin (inducer) and Hydroxychloroquine (HCQ, inhibitor). Sensitisation was assessed through employing a combination of HCQ with Temozolomide (TMZ) (HT) and Rapamycin pre-treatment followed by HT (RHT). Effective drug concentrations were determined through WST-1 viability assays. Immunoblotting for LC3-II and p62 allowed the determination of autophagic activity, whilst MFN1, MFN2, OPA1 and DRP1 protein levels indicated mitochondrial morphology regulation. Live cell imaging was conducted to assess mitochondrial fission and fusion rate. Image processing algorithms were constructed in Wolfram Mathematica (v. 10.2) to quantify mitochondrial morphometric alterations. Finally, high-resolution respirometry was conducted to assess mitochondrial coupling efficiency and apoptosis onset was assessed by immunoblotting for cleaved caspase 3 and cleaved PARP.

Results and Discussion: Autophagy induction with 50nM Rapamycin enhanced reductive capacity (135.0 ± 6.04 %), whilst inhibition with 50 µM HCQ resulted in a moderate decrease (86.22 ± 2.37 %). U-118MG cells proved sensitive to 24 hour TMZ (250 µM) treatment (80.19 ± 1.76 %), with reductive capacity decreased following HT (75.25 ± 3.493 %). Importantly, RHT treatment decreased viability to 52.65 % (± 1.06 %). This is further supported by significantly enhanced cleaved caspase 3 (146.00 ± 14.78 %) and cleaved PARP (157.60 ± 20.41 %) protein levels for the RHT group. Autophagic degradation was impaired in both the HT and RHT groups, as no significant increase in LC3-II expression was observed before and after Bafilomycin A1 treatment. Decreased mitochondrial fusion rates were observed following HCQ, TMZ, HT and RHT treatment, however, a decrease in both DRP1 and OPA1 was observed for the RHT group only. OXPHOS and ETS capacity were significantly impaired following RHT treatment, with an intermediate amount of network connectivity observed compared to the control and TMZ treatment group. Of note, decreased lactate production was observed in both the HT and RHT treatment groups, indicating decreased glycolysis.

Conclusion: Coordinated upregulation of autophagy followed by its inhibition prior to chemotherapy decreased OXPHOS capacity in GBM to the extent of enhancing apoptotic cell death onset. Impaired ETS coupling was associated with decreased OPA1 and DRP1 protein levels, which possibly contributed to intermediate mitochondrial network connectivity. Decreased lactate production in both modulation groups indicates that both glycolysis and OXPHOS was impaired in GBM cells. Therefore, reduced autophagic degradation likely impaired GBM metabolism and enhanced apoptosis onset.

Opsomming

Inleiding: Multivormige Glioblastoma (GBM) staan internasionaal bekend as die mees algemeen en kwaadaardige sentrale senuwee stelsel (SSS) gewas. Die gemiddelde oorlewingstydperk vir GBM pasiënte is slegs 15 maande en het vir die afgelope 30 jaar onveranderd gebly. Alhoewel baie vordering gemaak is in terme van die molekulêre patogenese van GBM, is daar min verandering gemaak aan kliniese behandelingstrategieë. ‘n Algemene ooreenkoms tussen alle GBM gewasse is hul oormatige energie vereistes om aanhoudende groei te verseker. Die metaboliese profiel van GBM bestaan uit beide oksidatiewe fosforilasie (OKSFOS) en aërobiese glikoliese. Met betrekking tot metabolisme is die proteïen afbraakproses, bekend as autofagie, bewys om kankermetabolisme te ondersteun tydens ‘n tekort aan voedingstowwe. Die vermoë van autofagie moduleerders om op te tree as bevorderingsmiddele vir chemoterapie is onlangs bestudeer, alhoewel die mate van inhibisie of induksie benodig vir effektiewe bevordering van seldood steeds onbepaald bly. Ons hipotese is dus dat autofagie modulasie die bioenergetika van glioomselle tot so ‘n mate sal belemmer dat dit seldood deur middel van chemoterapie sal bevorder. Hierdie studie beoog dus om: (i) die mate van autofagie modulasie wat benodig is vir seldood bevordering te bepaal; (ii) mitochondriese bioenergetika te evalueer in terme van topologie, dinamika en effektiwiteit van die elektronoordragsketting; (iii) te bepaal tot watter mate mitochondriese kapasiteit belemmer moet word om seldood te bevorder.

Metodes: ‘n *In vitro* model van GBM was saamgestel deur gebruik te maak van U-118MG glioblastoma selle. Chemiese autofagie modulasie was uitgevoer deur gebruik te maak van Rapamycin (induseerder) en hydroksiechloroquine (HCQ, inhibitor). Seldood bevordering was geëvalueer deur gebruik te maak van ‘n kombinasie van HCQ en Temozolomide chemoterapie (TMZ) (HT) asook vooraf behandeling met Rapamycin gevolg deur die HT behandelingskedule. Effektiewe dwelmkonsentrasies is bepaal deur middel van die WST-1 sellewensvatbaarheid toets. Proteïen uitdrukking van LC3-II en p62 het die evalueering van autofagiese aktiwiteit moontlik gemaak, terwyl die uitdrukking van MFN1, MFN2, OPA1 en DRP1 gedien het as aanwysers vir mitochondriese morfologiese regulasie en was bepaal deur die westelike kladtegniek. Die spoed van mitokondriese fisie en samesmelting is bepaal deur lewendige sell mikroskopie en beeldverwerking algoritmes is saamgestel in Wolfram Mathemica (v. 10.2) om morfologiese verandering te kwantifiseer. Hoë resolusie respirometrie was toegepas om mitochondriese suurstof verbruik te evalueer. Laastens is proteïen uitdrukking van gekleefde caspase 3 en gekleefde PARP nagegaan om apoptotiese seldood bevordering te evalueer en is bepaal deur middel van die westelike kladtegniek.

Resultate en bespreking: Autofagie induksie deur middel van 50nM Rapamycin het reduktiewe kapasiteit vermeerder (135.0 ± 6.04%), terwyl inhibisie met 50 µM HCQ ‘n matige vermindering in sellewensvatbaarheid veroorsaak het (86.22 ± 2.37 %). U-118MG selle was nie weerstandig teen 24 uur se inkubasie met TMZ (250 µM) nie (80.19 ± 1.76 %), met ‘n verdere afname in reduktiewe kapasiteit veroorsaak deur HT behandeing. Van groot belang is dat RHT behandeling sellewensvatbaarheid tot 52.65 % (± 1.06 %) laat daal het. Hierdie bevinding is verder ondersteun deur ‘n insiggewende vermeerdering in beide gekleefde caspase 3 (146.00 ± 14.78 %) en gekleefde PARP (157.60 ± 20.41 %) proteïenvlakke vir die RHT behnadelingsgroep. Die afbraak vermoë van autofagie was belemmer in beidie die HT en RHT groepe, aangesien geen insiggewende toename in LC3-II uitdrukking opgemerk is voor en na Bafilomycin A1 behandeling nie. ‘n Aansienlike afname in die spoed van mitochondriese samesmelting was aanskou vir die HCQ, TMZ, HT en RHT groepe, alhoewel verminderde proteïen uitdrukking slegs gevind was vir die RHT groep. OKSFOS en elektronoordragstketting kapasiteit was beduidend verminder na RHT behandling, met ‘n intermediêre hoeveelheid netwerkverbindings in vergelyking met die kontrole en TMZ groepe. Laktaat produksie was ook beduidend minder in the HT en RHT behandelingsgroepe, wat ‘n aanduiding is van ‘n belemmerde glikolise.

Gevolgtrekkings: Gekoördineerde induksie van autofagie gevolg deur inhibisie voor blootstelling aan chemoterapie het OKSFOS kapasiteit in GBM selle belemmer en apoptotiese seldood bevorder. Verswakte elektronoordragstketting aktiwiteit was geassosieer met verlaage OPA1 en DRP1 proteïen uitdrukking wat moontlik bygedra het tot die intermediêre hoeveelheid netwerkverbindings. Verlaagde laktaat produksie in beide modulasie groepe dui op verswatke glikolise en oksidatiewe fosforilasie. Die moontlikheid bestaan dus dat verminderde autofagiese aktiwiteit bygedra het tot verswakte GBM metaboliese kapasiteit en het sodoende apoptose veroorsaak.

Acknowledgements

I hereby sincerely thank the following people:

My supervisor, Dr Ben Loos, for his invaluable insights, encouragement and immense amount of patience throughout the course of this project. I would also like to thank him for his undying devotion towards his students. His passion for research and dedication to excellence is a true source of inspiration and has shaped me into the researcher I am today.

My co-supervisor, Prof Kristian Müller-Nedebock, the sincerest gratitude for always providing excellent advice and imaginative, yet concrete insights.

A heartfelt thank you to my parents, Kobus and Barbara Kriel, for their unconditional love and support throughout my studies. I would not have been able to make it this far without you.

NRF-DAAD for funding this project during 2016.

The Department of Physiological Sciences and the Neuro Research Group for constant support and providing a great work environment.

Dr Gerald Maarman and Prof Edward Ojuka for assistance with the oxygraph analysis and providing crucial technical insights.

Phillip Urich, for initial development of the image processing algorithms that enhanced the quality of my thesis greatly.

Punya Bhat, for conducting the glycolysis assays and for keeping me alive in India.

Lize Engelbrecht and the CAF team for technical assistance and training on the confocal microscope.

To Pieke Mans Sêr and the Stellenbosch University Chamber Choir for the music that kept me sane.

My flatmate, Ernest Dall, for providing the copious amounts of coffee and humour necessary to complete this project.

To my darling Lia, for your unwavering emotional support and for being the most radiant source of motivation in the darkest of days.

List of Conferences

Mitochondrial Physiology Society (2015); winner of the best poster presentation.

Physiology Society of South Africa (PSSA) Annual Meeting (2016); winner of the most innovative method award.

Microscopy Society of South Africa (MSSA) Annual Meeting (2016).

Article in preparation to be submitted to the Journal of Cellular Biology; “The effects of combined autophagy modulation on mitochondrial bioenergetics and cell death sensitisation in Glioblastoma Multiforme.”

References

List of figures

List of Tables

List of abbreviations

ADP:	Adenosine Diphosphate
AMPK:	AMP-activated protein kinase
ATG:	Autophagy related genes
ATP:	Adenosine Triphosphate
Baf:	Bafilomycin A1
BAK:	BCL-2 antagonist or killer
BAX:	BCL-2-associated X protein
BCL-2:	B cell lymphoma 2
BH3:	B cell lymphoma 2 (BCL-2) homology 3
BITC:	Brain Tumour Initiating Cells
BSA:	Bovine Serum Albumin
CCCP:	Carbonyl cyanide m-chloro phenyl hydrazine
CNS:	Central Nervous System
CSC:	Cancer Stem Cell
DNA:	Deoxyribonucleic Acid
DMEM:	Dulbecco’s Modified Eagles Medium
DMSO:	Dimethyl Sulfoxide
DRP1:	Dynamin Related Protein 1
EGFR:	Epidermal Growth Factor Receptor
ER:	Endoplasmic Reticulum
ETS:	Electron Transport System
FADD:	Fas Associated Death Domain
FADH:	Flavin Adenine Dinucleotide (Reduced)
FBS:	Foetal Bovine Serum
GBM:	Glioblastoma Multiforme

GFP:	Green Fluorescent Protein
GLUT:	Glucose Transporter
GTPase:	Guanosine Triphosphatase
HCQ:	Hydroxychloroquine Sulphate
HT:	HCQ in combination with TMZ treatment
IDH:	Isocytrate Dehydrogenase
IMM:	Inner Mitochondrial Membrane
LC3:	Protein Light Chain 3
MFF:	Mitochondrial Fission Factor
MFN1:	Mitofusin 1
MFN2:	Mitofusin 2
MGMT:	O^6 methyl guanine methyl transferase
Mito-PA-GFP:	Mitochondria Associated Photoactivateable Green Fluorescent Protein
MOMP:	Mitochondrial Outer Membrane Permeabilisation
MPT:	Mitochondrial Permeability Transition
mTOR:	Mammalian Target of Rapamycin
mTORC1:	Mammalian Target of Rapamycin Complex 1
NADH:	Nicotinamide Adenine Dinucleotide (Reduced)
NSC:	Neural Stem Cell
O_2:	Oxygen
OMM:	Outer Mitochondrial Membrane
OPA1:	Optic Atrophy 1
OXPHOS:	Oxidative Phosphorylation
PARP:	Poly ADP ribose polymerase
PDGFR:	Platelet Derived Growth Factor Receptor
PE:	Phosphatidylethanolamine
PenStrep:	Penicillin and Streptomycin

PKA:	cAMP-dependent protein kinase
PTEN:	Phosphatase and Tensin Homologue on Chromosome 10
RHT:	Rapamycin pre-treatment followed by HCQ and TMZ
ROI:	Region of Interest
ROS:	Reactive Oxygen Species
ROX:	Residual Oxygen Consumption
RTK:	Receptor Tyrosine Kinase
TEM:	Transmission Electron Microscopy
TMPD:	Tetramethyl-p-phenylenediamine dihydrochloride
TMRE:	Tetramethylrhodamine-Ethyl Ester
TMZ:	Temozolomide
TOMM20:	Translocase of Outer Mitochondrial Membrane 20
ULK:	Unc-51-like kinase
VEGF:	Vascular Epithelial Growth Factor
WST-1:	Water Soluble Tetrazolium Bromide

Units of Measurements

A:	ampere
%:	percentage
˚C:	degrees Celsius
µl:	microliter
µg:	microgram
µm:	micrometer
µM:	micromolar
g:	gram
kDa:	kilo Dalton
L:	litre
M:	molar
mg:	milligram
ml:	millilitre
nM:	nanomolar
pmol0$_2$/s*ml/CIV:	picomolar oxygen per second per millilitre normalised to complex IV activity
V:	Volts

Motivation

Globally, Glioblastoma Multiforme (GBM) presents as both the most prevalent and invasive form of Central Nervous System (CNS) malignancy. Patient life expectancy has remained virtually unchanged over the past three decades, with the mean survival time remaining only 15 months. This has been attributed to the highly adaptable nature of these tumours, making cell death evasion and rapid recurrence possible after being exposed to a combination of chemotherapy, radiation and surgical removal. Although many advances have been made in understanding the molecular pathogenesis of GBM, precision medicines have shown little progress due to the large genetic variability between patient tumour samples. Given that they originate from glial cells, one major commonality between all gliomas is their excessive energy requirements to uphold proliferation. Recent work by Marin-Valencia *et al*. (2012) have shown that the GBM metabolic profile is comprised of both oxidative phosphorylation (OXPHOS) and aerobic glycolysis, thereby not relying solely on the infamous “Warburg effect” as previously conceived. Furthermore, the protein degradation pathway known as autophagy has proved to further uphold tumour survival through providing the necessary metabolic intermediates in nutrient limiting or hypoxic conditions. We therefore hypothesised that glioma cells can be sensitized to undergo cell death through modulating autophagy in order to decrease their bioenergetic efficiency and ultimately make them more susceptible to chemotherapy. Both the upregulation and inhibition of autophagy has recently been shown to have promising effects in combination with chemotherapy (Rangwala, *et al*., 2014; Arcella *et al*., 2013), which motivated us to establish whether a specific amount of autophagic flux is necessary to prevent or promote glioma cell death. Furthermore, we attempted to resolve the long standing controversy over whether the biophysical morphology of mitochondrial networks has a significant influence on their electron transport system (ETS) efficiency. Through understanding the interplay between the autophagic and mitochondrial systems, we hope to construct a more coherent bioenergetic profile of GBM capable of enhancing future clinical interventions.

Chapter 1: Literature Review

1.1 Glioblastoma Multiforme

Gliomas represent a collection of tumours arising from glial cells and currently hold a mean international incidence rate of 5 in 100 000 persons (Wesseling *et al*., 2011). Grade IV astrocytomas, referred to as glioblastoma multiforme (GBM), constitute 60-70% of all reported astrocytomas, making it both the most malignant and most prevalent glial cell tumour (Wen & Kesari 2008). This can be attributed to the heterogeneous nature of these tumours, both phenotypically and genetically, resulting in general cellular characteristics such as unrestricted proliferation, neo-vascularisation, extensive invasion of surrounding tissues and resistance to apoptosis. Currently, surgical removal followed by radiation and chemotherapy with Temozolomide (TMZ) constitute the only life prolonging treatment option. In addition to apoptotic resistance, these tumours take advantage of normal astrocytic morphology to intertwine with surrounding brain tissue, making complete surgical removal impossible. Therefore, the patient survival outcome post-treatment remains bleak, with a mean survival time of only 12-15 months and a maximum of 5 years reached by less than 5% of patients (Stupp *et al*., 2009).

According to the latest figures released by the South African Medical Research Council, brain cancer is one of the top 20 causes of cancer related deaths in South Africa, surpassing that of melanoma and kidney cancer with a total of 527 deaths in 2000 (Cancer Association of South Africa, 2000). Given that these statistics are only based on histological diagnoses, and that tumours are not categorised according to subsets, comprehensive primary brain tumour incidence rates remain difficult to obtain for South Africa. However, Ibebuike *et al*. (2013) revealed that in a South African cohort of 151 patients, gliomas accounted for 21.2% of all diagnosed intracranial malignancies.

Developing an effective treatment for GBM therefore remains a global challenge, with many insights to be gathered especially regarding astrocytic tumour metabolism and chemotherapeutic resistance.

1.1.1 The role of astrocytes in neuronal homeostasis

Upon the discovery of glial cells in the early 1850's, their perceived importance was rather underwhelming. Though commonly translated to English as glue, the Greek word *gliok* also refers to slime. Thus, the star-like projections observed between neurons by Golgi (1985) were merely described as support cells of the Central Nervous System (CNS) (Somjen 1988).

Fortunately, as research progressed, the function of astrocytes in particular was found to stretch far beyond that of mere structural support. Through regulating ion homeostasis, exchange of metabolites, and clearance of the neurotransmitters glutamate and gamma-aminobutyric acid (GABA) from the extrasynaptic milieu, astrocytes have been established as crucial role players in intersynaptic communication (Ransom *et al*., 2003; Newman, 2003). Many of these functions were attributed to their characteristic spongiform morphology, which allows for close contact with surrounding neurons and synapses. Regulation of substrates within the extracellular space allows for glial detection and modulation of synaptic activity by signalling to the immediate vasculature for increased blood and substrate delivery (Galeffi & Turner, 2012).

There is, however, evidence that suggests a larger realm of complexity surrounding astrocyte functionality. Studies making use of more sensitive imaging techniques have shown that astrocytic processes do not necessarily overlap with one another, but instead operate within their own specific anatomical domains. Bushong *et al*. (2002) demonstrated that protoplasmic astrocytes in the Stratum Radium function within exclusive territories. Subsequent work by Wilhelmsson *et al*. (2006) found that reactive astrocytes located in the dentate gyrus and cerebral cortex of mice maintained their anatomical position following injury, with no signs of increased activity from neighbouring astrocytic processes. With regards to synapse activity, the ability of astrocytes to modulate synaptic transmission was initially attributed to exocytotic release of glutamate, leading to the '*tripartite synapse'* description by Araque *et al*. (1999). Although elevations in Ca^{2+} have been observed in response to changes in synaptic activity, arguments have been raised as to whether these responses are merely passive. Thus far, astrocytes have been shown to respond selectively to synapses of differing neurotransmitter use and are capable of discriminating between neural networks on the basis of inherently used neurotransmitter (Perea *et al*., 2009). These findings suggest that it is possible for synaptic information to be processed more intuitively through an intricate nonlinear astrocytic response.

Given their immense energy requirements together with a rapidly changing extracellular microenvironment, astrocytes possess the ability to alter their metabolism according to external changes. Astrocytic end-processes are vigorously intertwined with the brain vasculature, making large amounts of glucose readily available. In contrast to the glucose transporter expressed by neurons, GLUT3, astrocytes express the GLUT1 isoform. Thus, it allows astrocytes to transport glucose at a rate 7 times faster than that of normal neurons, resulting in higher glycolytic flux within astrocytic cells (Vannucci *et al*., 1997). Furthermore, these glial cells are capable of storing glucose in the form of glycogen, thereby allowing them to adapt to situations of increased energy demand. This was demonstrated by Hertz *et al*., (2007), where a marked increase in astrocytic utilization of glucose-6-phosphate derived from glycogen was observed under conditions of intense neuronal stimulation and hypoglycaemia.

Although the complexity with which astrocytes govern neural communication has yet to be fully elucidated, their importance to neuro-physiological health is invaluable. Unfortunately, the remarkable metabolic robustness of these cells becomes an extremely debilitating characteristic under oncogenic conditions.

1.1.2 The Pathogenesis of GBM

Although various genetic abnormalities have been associated with astrocytomas (Fig. 1.1), consensus has yet to be reached over a specific gene mutation cluster responsible for GBM onset. Mutations are so variable between tumour samples that researchers have been unable to create a fully representative animal model of GBM. Given this lack of translatable animal models, little progress has been made with regards to effective clinical treatment plans. Consequently, GBM treatment has remained largely unchanged for the past 3 decades.

Fortunately, recent genomic characterization of primary GBM tumour samples has identified key genetic abnormalities that contribute to malignancy. These aberrations were found to act in a coordinated fashion, mainly altering signalling through Receptor Tyrosine Kinase (RTK) pathways and the p53 and RB tumour suppression pathways. Amplifications in the genes encoding for Epidermal Growth Factor Receptor (EGFR) and platelet derived growth factor receptor (PDGFR) are commonly observed in gliomas (Dunn *et al*., 2012). Increased ligand binding and subsequent oligomerisation of these RTKs causes phosphorylation of tyrosine residues on the receptor tails, making recruitment of adaptor proteins possible. One such adapter, Ras, is responsible for initiating the Raf-MEK-ERK kinase cascade which controls the transcription of Vascular Epithelial Growth Factor (VEGF). VEGF is important for angiogenesis, and therefore promotes tumour survival by facilitating neovascularisation during tumourigenesis (Plate *et al*., 1992). Neovascularisation is common for solid tumours, however recent evidence suggests that gliomas produce vasculature *de novo* in a quite unique manner.

Instead of solely relying on VEGF, xenograft studies by Soda *et al*., (2011) demonstrated that new glioma vasculature expressed the same oncogenic profile as that of the implanted tumour which differed substantially from that of host endothelial cells. This display of pluripotency, i.e. the ability to differentiate from glioma cells to endothelial cells, strengthens the long standing hypothesis that gliomas originate from cancer stem cells (CSCs). Neural stem cells (NSCs) are known to be critical during embryogenesis and are also essential for adult tissue repair. Although the long lifespan of these cells makes them more prone to accumulate mutations, p53 and PTEN was found to control cell renewal and differentiation in both NSCs and glioma cells of the sub ventricular zone (SVZ) (Zheng *et al*., 2008). In this regard, Zheng *et al*., (2008) have identified a subpopulation of clonal sub ventricular zone GBM cells capable of giving rise to tumourigenic cells of different molecular and histological characteristics. The SVZ has therefore been postulated to be a site of origin for GBM tumours (Jacques *et al*., 2010).

Although understanding the origin of GBM is of great importance, the malignancy of these tumours is of such a degree that preventative treatment would have no major life prolonging effect. Therefore, targeting tumour metabolism remains a more viable therapeutic target. Increased PI3K activity is brought about by altered RTK signalling and provides an excellent support structure for optimal tumour growth, given its regulatory role in metabolic maintenance and cell-cycle control processes. After recruitment to the plasma membrane, PI3K enables conversion of PIP2 to PIP3, which is necessary for the attraction of Akt. Akt has multiple downstream effectors crucial to cellular homeostasis, including p53, forkhead box O (FOXO), glycogen synthase kinase 3 (GSK3) and mammalian target of Rapamycin complex 1(mTORC1) (Engelman *et al*., 2006; Manning & Cantley 2007). In the context of gliomas, PI3K signal transduction was found to be enhanced by deletions of its inhibitor, phosphatase and tensin homologue on chromosome 10 (PTEN).

Widely regarded as the guardian of the genome, p53 is known to mediate oncosuppression by reacting to DNA-damage through cell cycle arrest and apoptosis induction. It was also shown to be inactivated in the early stages of GBM formation in certain patients (Zheng *et al*., 2008). Akt is capable of inhibiting p53 through activation of MDM2, as well as causing a decrease in G1 progression through inhibition of Foxo and GSK3 (Manning & Cantley, 2007). Another crucial downstream target of Akt is mTORC1, which is responsible for regulating the intracellular recycling process known as autophagy (Edinger & Thompson 2002). Regulation via mTORC1 is achieved by inhibiting the molecular machinery necessary for autophagy initiation when nutrients are readily available. Deregulation of this process results in excessive breakdown of intercellular constituents leading to a substantially increased energy supply. p53 has also been shown to induce autophagy through two of its target genes, Sestrin1 and Sestrin2, capable of inhibiting mTOR through stimulation of AMPK (Maiuri *et al*., 2009). Therefore, p53 can play either an oncosuppressive or supportive role in GBM depending on its level of expression, as suggested by Hermisson *et al*., (2006). Hence, resistance to treatment is context dependent, being influenced by both the genetic composition and metabolic capacity of tumours as well as the type of chemotherapy used. In the context of gliomas, the chemotherapeutic standard is Temozolomide (TMZ), which causes cell death through alkylation-mediated DNA damage (Kitange *et al*., 2009).

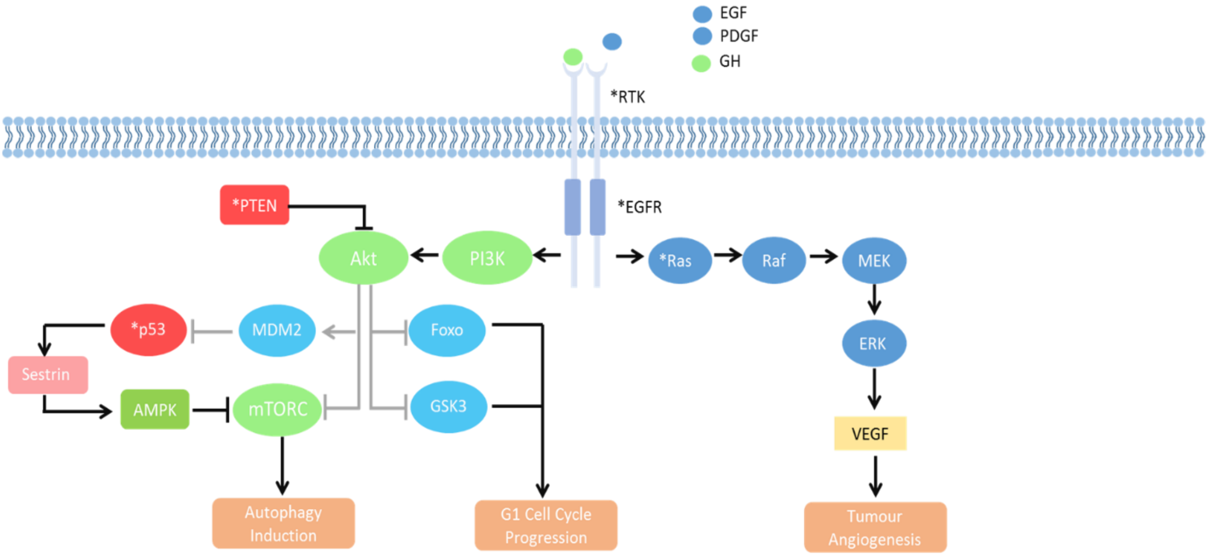

Figure 1.1 Molecular pathogenesis of glioblastoma. Altered Receptor Tyrosine Kinase (RTK) expression enhances recruitment of PI3K enables conversion of PIP2 to PIP3, which is necessary for the attraction of Akt. Akt has multiple downstream effectors, including p53, forkhead box O (FOXO), glycogen synthase kinase 3 (GSK3) and mammalian target of Rapamycin complex 1 (mTORC1). Akt is capable of inhibiting p53 through activation of MDM2, and also causes a decrease in G1 progression through inhibition of FOXO and GSK3. p53 has also been shown to induce autophagy through two of its target genes, Sestrin1 and Sestrin2, capable of inhibiting mTOR through stimulation of AMPK

1.1.3 Epigenetic origins of chemotherapeutic resistance

Epigenetics refers to a change in gene expression brought about by external changes which is independent of an alteration in the sequence of cellular DNA. Methylation of promoter regions can bring about gene silencing by interfering with transcription factor binding. Seeing as methylation commonly occurs in CpG-rich areas, referred to as CpG islands, gene silencing also results from interference with methyl-CpG-binding domain proteins that are responsible for decreased transcription. Gene-specific hypomethylation is common in the genome of gliomas, especially with regards to the O^6 methyl guanine methyl transferase (MGMT) gene, which encodes the DNA repair protein O^6-alkylguanine DNA alkyltransferase (AGT) (Esteller, 2008). Removal of alkyl groups from the O^6 position of guanine is mediated by AGT, the failure of which results in apoptotic cell death (Hermisson *et al*., 2006). Therefore, the regulation of AGT is crucial in the context of glioma cell death, seeing as TMZ is an alkylating agent.

Consequently, tumours resistant to TMZ display unmethylated MGMT promoter regions providing ample transcription levels of AGT capable of counteracting the DNA damage that would normally be caused by TMZ (Hegi *et al*., 2005). It is postulated that initial chemotherapy contributes to MGMT methylation, resulting in cell death, whereas recurring secondary tumour cells are capable of surviving due to their lack of methylation. However, there is currently no alternative treatment for patients who present with resistant primary or secondary tumours, even when the genetic origin is known.

The lack of alternative treatment options given the amount of genetic studies conducted during the past thirty years has sparked global research efforts to the development of clinically translatable therapies that compromise gliomas metabolically.

1.2 Glioma metabolism: Dependence on glucose oxidation and autophagy

Cancer metabolism has predominantly been hallmarked as independent of oxidative phosphorylation (OXPHOS), relying on high rates of aerobic glycolysis for lactate production, known as the “Warburg effect” (Warburg 1956). A growing body of evidence suggests that many tumours are capable of metabolic adaptation through utilization of both glycolysis and OXPHOS, which challenges Warburg’s theory (1959) (Seyfried *et al*., 2011; Jose *et al*., 2011). In line with these findings, gliomas have recently been characterised as being both oxidative and glycolytic, depending on their level of malignancy (Griguer *et al*., 2013; Marin-Valencia *et al*., 2012; Kennedy *et al*., 2013). In the context of chemotherapeutic resistance, glioma cells have been shown to depend on enhanced ETC coupling and autophagy to acquire resistance to TMZ (Oliva *et al*., 2011; Kanzawa *et al*., 2004; Rosenfeld *et al*., 2014; Arcella *et al*., 2013). In light of these findings, the following section will outline the function of mitochondrial bioenergetics and autophagy in the metabolism of both healthy cells and gliomas.

1.2.1 The dynamic role of mitochondria

Mitochondria can be viewed as the “central energetic hub” of the cell, crucial to the integration of pathways controlling both cellular life and death. Through maintaining TCA cycle and OXPHOS activity, ATP is produced from various sources, including glycolysis, glutaminolysis and β-oxidation. Certain biomolecules such as lipids, pyrimidines, heme moieties and some amino acids are also produced through TCA cycling. Conversely, mitochondria are critical initiators of both apoptotic cell death, through mitochondrial outer membrane permeabilisation (MOMP), and necrotic cell death, through mitochondrial permeability transition (MPT). The dynamic nature of these organelles is further revealed by their high degree of adaptability to micro-environmental cues, even undergoing morphological changes in order to alter their bioenergetic output and evade degradation through mitochondrial specific autophagy, referred to as mitophagy. Given these characteristics, it has become increasingly clear that cell death is metabolically regulated (Green *et al*., 2014). Therefore, in order to understand tumourigenic evasion of cell death, the bioenergetics governing cellular life must be understood.

Mitochondria do not function as stagnant organelles. Rather, they operate as a highly energetic reticulum subjected to continuous and highly rapid remodelling through fission and fusion (Fig. 1.2). These events serve as a quality control mechanism by separating damaged mitochondria from those in an interconnected state, thereby ensuring optimal respiratory chain efficiency. Fission and fusion of mitochondria relies on specific guanosine triphosphatases (GTPases) as well as the voltage across the inner mitochondrial membrane, known as the mitochondrial membrane potential ($\Delta\varphi_m$). Due to their association with the tubulin network, mitochondria can undergo either complete or transient fusion. The latter entails membrane fusion followed by an immediate fission event, which can lead to asymmetric fission (Twig *et al*., 2008). Due to their association with the microtubulin network, it has been postulated that these transient or asymmetric events are due to organellar association with adjacent cytoskeletal tracks (Liu *et al*., 2009).

Mitochondrial dynamics are highly dependent on bioenergetic cues. In response to nutrient deprivation, enhanced fusion increases the amount of IMM cristae, thereby increasing respiratory chain efficiency. Although this explains the appearance of fragmented networks during satiety (Liesa & Shirihai 2013), excessive membrane potential dissipation can render fragmented mitochondria incapable of re-fusing, thereby metabolically debilitating the cell (Twig *et al*., 2008). Therefore, interplay between the molecular fission and fusion machinery is tightly regulated to maintain optimal bioenergetic sensing.

All critical fission and fusion mediators are members of the Dynamin superfamily. This is made evident by the homologous GTPase domains observed between the fusion proteins Mitofusin 1 (Mfn1), Mfn2 and Optic atrophy 1 (Opa1), as well as the fission modulator Dynamin related protein 1 (Drp1). Recruitment of cytosolic Drp1 to the mitochondrial membrane is accomplished through interaction with outer mitochondrial membrane (OMM) anchored Fis1. The subsequent formation of ring-like multimeric fission complexes results in the restriction of GTP hydrolysis, resulting in the fission of both the inner and outer membranes (Palmer *et al*., 2011).

During fusion, coalescence of both the IMM and OMM is required (Fig. 1.2). Mfn1 and Mfn2 are localised to the OMM with an N-terminal GTPase and C-terminal heptad repeat region (HR2) exposed to the cytosol. Homo and hetero-oligomeric complex formation of the mitofusins is facilitated by *trans* antiparallel coiled-coil interactions between opposing HR2 domains (Benard & Karbowski 2009). IMM fusion and cristae remodelling is mediated by Opa1. Eight splice variants exist for Opa1, and the balance between long (L) and short (S) isoforms has been reported to alter fusion efficiency. Furthermore, Guillery *et al*., (2008) have shown that Opa1 processing can be modulated by changes in the MMP.

Regulation of mitochondrial dynamics is also crucial to mitochondrial quality control. A critical prerequisite for removal of damaged mitochondria through mitophagy, is the degree of membrane depolarisation Twig *et al.,* (2010).

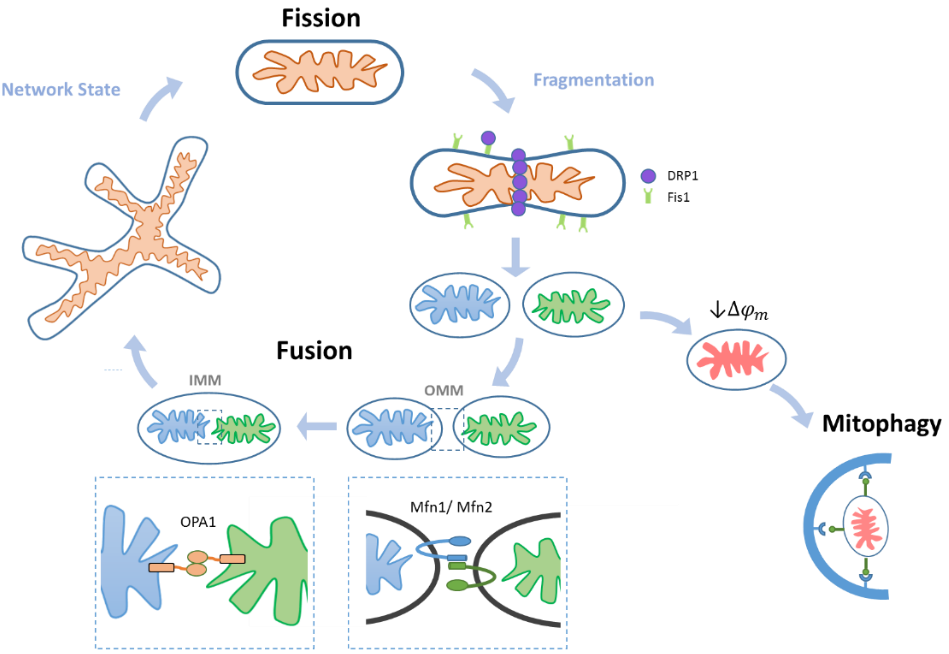

Figure 1.2. Regulation of mitochondrial dynamics. Recruitment of cytosolic Drp1 to the mitochondrial membrane is accomplished through interaction with outer mitochondrial membrane (OMM) anchored Fis1. The subsequent formation of ring-like multimeric fission complexes results in the restriction of GTP hydrolysis, resulting in the fission of both the inner and outer membranes. Fusion of both the inner mitochondrial membrane (IMM) and OMM is required (Fig. 1.2). OMM fusion is facilitated by either Mfn1 or Mfn2, whereas IMM fusion is mediated by OPA1.

Upon reaching the appropriate depolarisation threshold, recruitment of PINK1 to the OMM is initiated. Subsequent binding of Parkin to PINK1 results in OMM ubiquitination, which attracts the autophagic machinery necessary for vacuolar engulfment and subsequent degradation (Karbowski *et al*., 2007; Matsuda *et al*., 2010). Interestingly, Narendra and colleagues (2008) have reported that inhibition of mitochondrial fusion and loss of mitochondrial membrane potential results in Parkin translocation to damaged mitochondria only. The selection of healthy mitochondria into homogenous networks is therefore ensured by the dynamic interplay between fission, fusion and mitophagy, which in turn ensures for optimal respiratory chain efficiency (Fig. 1.2).

1.2.2 Mitochondrial respiration

The Electron Transport Chain (ETC) is located within the IMM and is responsible for driving ATP-synthase activity through maintaining a sufficient proton gradient across the inner mitochondrial matrix. Although ATP is the major chemical constituent that regulates cellular metabolism, the amount of ATP produced is not necessarily indicative of ETC efficiency (Gnaiger *et al.,* 2008). Rather, it is the capacity of the respiratory chain to maintain a profitable phosphate potential or Gibbs free energy to drive ATP synthesis (Devin & Rigoulet, 2007). This phenomenon was first explained in Peter Mitchell's chemiosmotic coupling theory, wherein the capacity of electron transfer to regulate ADP phosphorylation was attributed to a transmembrane protonmotive or chemiosmotic force (Δp_{mt}) (Mitchell, 1961). Importantly, the Δp_{mt} is influenced by both the mitochondrial membrane potential ($\Delta\varphi_m$), and the pH difference across the inner membrane (ΔpH).

Although the net outcome of chemiosmotic coupling is ATP production, cellular ATP requirement does not necessarily coincide stoichiometrically with the reoxidation of reduced equivalents formed as a result of respiratory chain activity. Therefore, the ratio of phosphorylation to oxidation has to be adjusted separately and with great specificity. One of the main physiologic adaptations found to accommodate such regulation is the site of electron supply to the ETC which is affected predominantly by the ratio of NADH to $FADH_2$. Three coupling sites, namely complexes I, III and IV, exist for NADH, whilst only complexes II and IV are involved in $FADH_2$ oxidation (Fig. 1.3). Therefore, metabolic substrate composition (i.e. carbohydrates, fatty acids or amino acids) plays a major role in determining the efficiency of oxidative phosphorylation through the ETC. Fatty-acid β-oxidation, for example, yields equimolar concentrations of NADH to $FADH_2$, whereas acetyl-CoA oxidation through the TCA cycle yields 3 NADH molecules to 1 $FADH_2$.

Altering the expression of key fission and fusion proteins have elucidated the intricate relationship between mitochondrial dynamics and their respiratory capacity. Enhanced Mfn2 expression proved to increase glucose oxidation and membrane potential, whereas Mfn2 knockouts seemed to inhibit pyruvate, glucose and fatty acid oxidation *in vitro* (Pich *et al*., 2005). Similarly, loss of OPA1 expression was found to decrease respiratory complex efficiency and decreased membrane potential (Mishra *et al*., 2014). The detrimental effects of Drp1 deletions have been shown i*n vivo* by Ishihara *et al*., (2009), where Drp1 knockout mice presented with defects in forebrain and synapse development, liver abnormalities and weakened cardiac function.

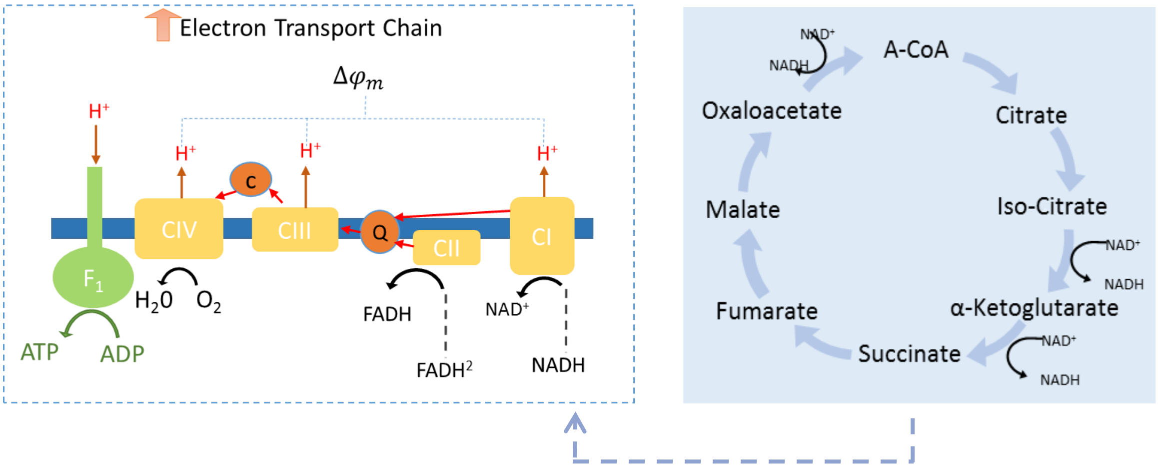

Figure 1.3. TCA cycling maintains electron transport chain efficiency.

1.2.3 Glioma dependence on OXPHOS

By infusing intact human brain tumours with ^{13}C-Glucose and tracking its fate with NMR spectroscopy, Maher *et al*., (2012) observed high degrees of glucose oxidation in malignant gliomas. Utilising a similar method, i*n vivo* analysis of human orthotopic GBM tumours in mice (Marin-Valencia *et al*., 2012) provided evidence that the GBM metabolic phenotype consists of both oxidative and anaerobic pathways. High resolution respirometry further revealed that TMZ resistant glioma cells displayed a larger amount of ETC coupling and decreased ROS production when compared to that of TMZ sensitive cell lines (Oliva *et al*., 2011).

Liquid chromatography mass spectrometry (LC-MS) of patient tumour samples by Deighton *et al*., (2014) revealed the first coherent interactome of mitochondrially associated proteins in GBM. Interestingly, proteins associated with Complex-I activity (ACADM, ACOT7, DECR1, SCP2, for example) were found to be down-regulated, whilst certain proteins involved in amino acid metabolism (AASS, LAP3 and SHMT2) were found to be upregulated. AASS is necessary for the conversion of lysine to glutamate, thereby adding to TCA cycle efficiency through production of α-ketoglutarate. SHMT2 expression was shown to be enhanced by cMyc activity, and therefore plays an oncosupportive role through catalysing metabolism of serine to glycine. In accordance with previous studies, IDH1 and IDH2 expression was also shown to be altered, decreasing production of α-ketoglutarate which results in an increased HIF-1 activity, thereby further contributing to glioma development (Yan *et al*., 2009; Yang *et al*., 2009). Given these contradictory results, it is likely that each tumour has a unique mitochondrial interactome capable of either upholding the metabolism of an established high-grade tumour or enhancing the malignancy of newly formed tumours.

The exact molecular mechanism responsible for preferential metabolic alterations in gliomas remains unclear, although overexpression of the p53-dependent effector Tp53-induced glycolysis and apoptosis regulator (TIGAR) has been observed in starvation models to improve glucose utilization through enhancing mitochondrial respiration and decreasing glycolysis *in vitro* (Wanka *et al*., 2012).

1.2.4 Mitochondrial control of Apoptosis

Mammalian cells have conserved several mechanistically diverse processes that facilitate cell death in response to prolonged disruptions of either intracellular or extracellular homeostasis. These are commonly referred to as forms of programmed cell death (PCD) and includes apoptosis (type I cell death), autophagy (type II cell death) and necrosis (type III cell death) (Galluzzi *et al*., 2016). Although classical cell death descriptions include autophagy as a mode of cell death, its importance in cell metabolism has led many to challenge this view, suggesting that it serves as a facilitator rather than an effector (Green *et al*., 2014). Subsequently, more specialised forms of PCD have been identified that share commonalities with major cell death modes, such as autosis, necroptosis and ferroptosis (Liu & Levine, 2015; Zhang *et al*., 2015; Dixon *et al*., 2016).

The involvement of mitochondria in cell death mechanisms stems from their centrality in metabolic signalling, producing both ATP as well as a variety of critical biomolecules. Two main mitochondrial mechanisms exist for cell death induction. The first being mitochondrial outer membrane permeabilisation (MOMP) which leads to apoptosis, as opposed to mitochondrial permeability transition (MPT) which initiates necrosis (Fig. 1.4). MOMP is initiated through the intrinsic apoptotic pathway. As a result of prolonged exposure to lethal stimuli such as radiation, cytotoxicity or hypoxia, DNA damage and ER-stress ensues, which initiates active B cell lymphoma 2 (BCL-2) homology 3 (BH3)-only proteins through p53 mediated signalling (Shimizu *et al*., 2004; Youle & Strasser, 2008). The BH3-only proteins BID, BAD and BIM subsequently activate either BCL-2-associated X protein (BAX) or BCL-2 antagonist or killer (BAK) to undergo conformational changes necessary to target the mitochondrial outer membrane (Fig. 1.4). The exact mechanism through which BAX and BAK is induced to cause MOMP remains however unclear, although oligomerization of both proteins seems to be a strong pre-requisite, given that mutant BAX and BAK fail to form oligomers and induce MOMP. However, the specific amount of oligomerization of either protein necessary to achieve MOMP has yet to be resolved.

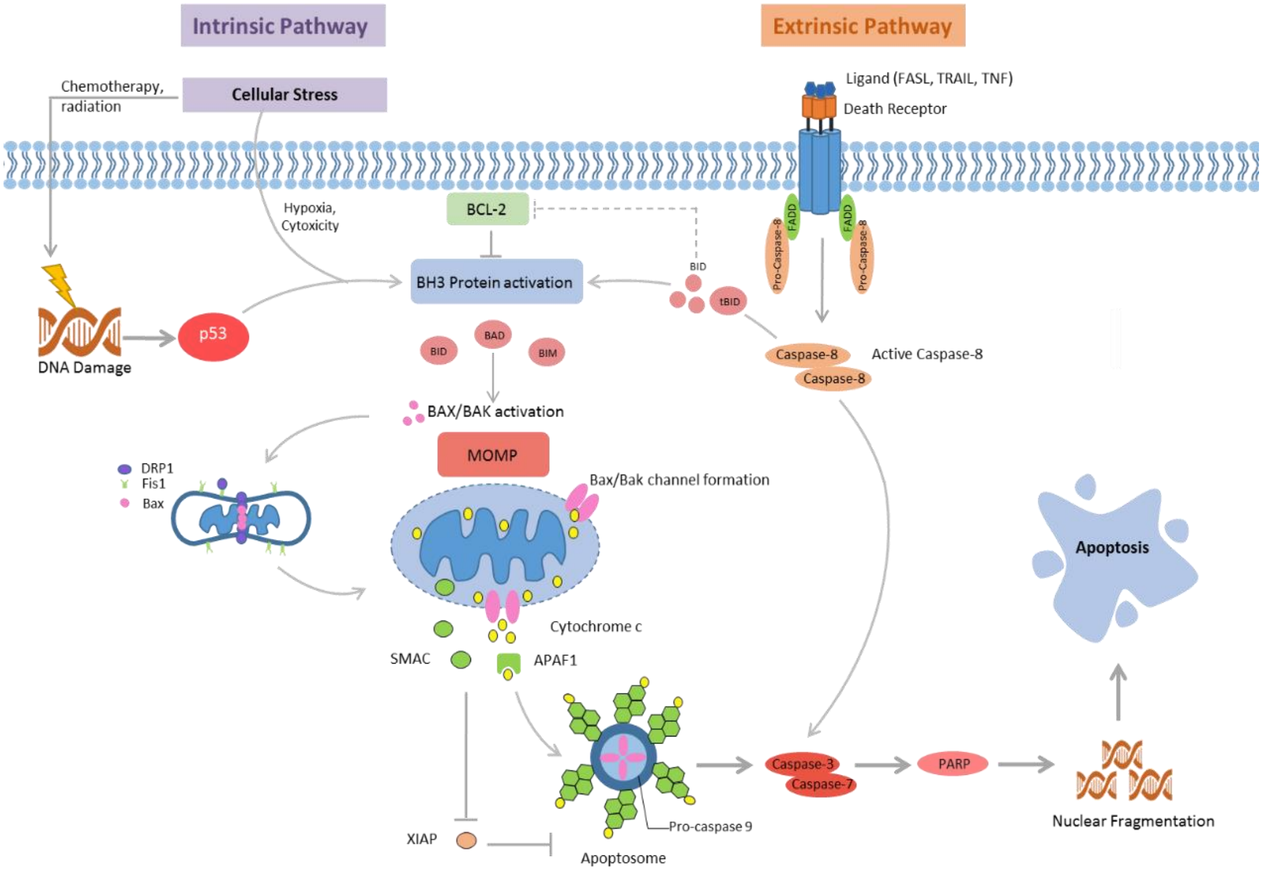

Figure 1.4. Regulation of apoptosis through both the intrinsic and extrinsic pathways. B cell lymphoma 2 (BCL-2) homology 3 (BH3)-only proteins are activated through p53 mediated signalling. The BH3-only proteins BID, BAD and BIM subsequently activate either BCL-2-associated X protein (BAX) or BCL-2 antagonist or killer (BAK) which cause mitochondrial outer membrane permeabilisation (MOMP). Subsequent cytochrome-c release promotes APAF1 oligomerization into the heptameric apoptosome, activating caspase 9, resulting in the cleavage of caspases 3 and 7, inactivating PARP, leading DNA damage and cell death onset. Second mitochondria-derived activator of caspase (SMAC) is released following MOMP, inhibiting the activity of X-linked inhibitor of apoptosis protein (XIAP). Mitochondrial independent apoptosis is dependent on Fas receptor oligomerization and subsequent recruitment of the Fas-associated death domain (FADD) adaptor protein to its intracellular death domain (DD). Procaspase-8 associates with FADD to form the death-inducing signalling complex (DISC), whereby cleaved caspase 8 is formed, responsible for activating caspase-3 and initiating downstream effects similar to MOMP induced apoptosis

Although its initiation is still unclear, MOMP induced cytochrome-c release has been well documented by tracking cytochrome-c linked GFP through Live Cell Imaging (Bouchier-Hayes *et al*., 2008). Interestingly, these studies have shown that MOMP is propagated in a 'wave-like' fashion across the mitochondrial network and can occur as quickly as five minutes following initiation, strengthening the notion that relying on protein expression levels as indicators of highly dynamic events does not portray its true nature. Cytochrome-c release promotes APAF1 oligomerization into the heptameric structure known as the apoptosome, capable of recruiting and activating caspase 9, resulting in subsequent cleavage of caspases 3 and 7 (Riedl & Salvesen 2007). Although many protein substrates are targets for caspase cleavage, inactivation of DNA repair enzymes such as PARP plays a pivotal role in cell death onset. Furthermore, second mitochondria-derived activator of caspase (SMAC) is also released from the MIM following MOMP, inhibiting the activity of X-linked inhibitor of apoptosis protein (XIAP), which normally binds directly to and inhibits caspases 9, 3 and 7 (Murphy *et al*., 2013). Therefore, MOMP enhances both apoptosome formation and inactivates molecular repair enzymes, lending it the popular title as the 'point of no return' of cell death (Loos & Engelbrecht 2009).

Contrary to MOMP, mitochondrial independent apoptosis can also occur and is mediated by the extrinsic signalling pathway. Upon binding of Fas-ligand, the Fas receptor oligomerizes and recruits the Fas-associated death domain (FADD) adaptor protein to its intracellular death domain (DD) region. Procaspase-8 associates with FADD to form the death-inducing signalling complex (DISC), whereby cleaved caspase 8 is formed, responsible for activating caspase-3 and initiating downstream effects similar to MOMP induced apoptosis (Fig. 1.4). Although Fas is ubiquitously expressed in healthy tissues, its expression is upregulated in rapidly proliferating cells to maintain uncontrolled growth. It is therefore of no surprise that highly malignant tumours such as gliomas have been reported to be resistant to Fas-related apoptosis. Importantly, a certain level of cross-talk does exist between the intrinsic and extrinsic pathway. Following caspase 8 cleavage, the BH3-interacting domain death agonist (BID) is activated, the truncated form of which ,tBID, can initiate BH3-protein activation and thereby enhance apoptosis onset (Saggioro *et al*., 2014).

Although dysregulation of the apoptotic pathway is commonly attributed to chemotherapeutic resistance, evidence of how altered interactions within this pathway relates to the ability of GBM to effectively evade cell death is scarce. Utilising a mathematical model to predict cellular susceptibility to cell death onset following caspase cleavage, Murphy *et al*., (2013) were able to successfully predict survival times of patients with long term progression free gliomas. Albeit useful, the model failed to accurately estimate survival time for tumours in the short term progression free patient cohort, which displayed the highest amount of resistance. This highlights the limiting effect of studying tumour cell death mechanisms in isolation from its bioenergetics.

1.3 Autophagy

In order to fully appreciate the role of autophagy in tumour metabolism, the following section will highlight the regulatory mechanisms responsible for autophagic degradation. Much controversy surrounds the involvement of macro-autophagy in tumourigenesis. Its induction during nutrient limiting conditions allows for the additional supply of substrates to uphold cancer metabolism and proliferation, thereby promoting tumour formation (White and Rabinowitz, 2010). On the other hand, monoallelic deletions of critical autophagy associated genes in certain cancer types have led many to regard autophagy as anti-tumourigenic. In the context of gliomas, decreased Beclin-1 expression has been observed (Miracco *et al*., 2007), suggesting decreased autophagic signalling. In this regard, Levine *et al.,* (1999) have shown that Beclin-1 is involved in tumour suppression, reporting higher endogenous expression in healthy breast tissue than in breast tumour samples. Further work by Pattingre *et al*., (2005) indicated that interaction of BCL-2 anti-apoptotic proteins with Beclin-1 can decrease Beclin-1 dependent autophagy. Conversely, TMZ was found to induce autophagy in glioma cells *in vitro*, with cytotoxicity being enhanced by concomitant treatment with the autophagy inhibitor bafilomycin which suggests and increased dependence on autophagy (Kanzawa *et al*., 2004). Inhibition of autophagy, either pharmacologically or through Beclin-1 knockdowns, in primary cell cultures of established solid tumours display less resistance to cytotoxic stimuli than their wildtype counterparts (Boya *et al*., 2005; Amaravadi & Thompson 2007; Galluzzi *et al*., 2010). Genetic inhibition of autophagy in mammary CSCs has also proven to impair tumour formation (Gong *et al*., 2012). In line with these findings, recent clinical trials assessing the effect of concomitant autophagy inhibition with chloroquine have also shown promise in patients with high grade gliomas and melanomas (Rosenfeld *et al*., 2014). Conversely, upregulation of autophagy through Rapamycin treatment has also proven to decrease glioma tumour size *in vivo* (Arcella *et al*., 2013). Given these paradoxical findings, it is necessary to carefully dissect the molecular machinery regulating autophagy and their interaction with apoptotic proteins.

1.3.1 Induction and Regulation

Coined by De Duve. in 1966, autophagy serves to maintain cellular energy homeostasis under nutrient limiting conditions by means of self(auto) -consumption(phagy) (De Duve & Wattiaux 1966). As a result, long-lived or damaged cytoplasmic proteins are degraded providing substrates to the TCA cycle and preventing detrimental protein aggregation.

Three main forms of autophagy exist, namely chaperone-mediated autophagy, micro-autophagy and macroautophagy (Yorimitsu & Klionsky 2005). Chaperone-mediated autophagy occurs via specific motif targeting by the heat shock cognate 70 (Hsc70) chaperone protein in order for lysosomal internalization to occur (Arias & Cuervo 2011). Micro-autophagy is conducted by means of endocytosis resulting in the direct uptake of cytosolic proteins (Singh & Cuervo 2011). Macroautophagy involves the bulk sequestration of cytoplasmic contents into double membrane vesicles, termed autophagosomes (Green & Levine 2014). Macroautophagy (hereafter referred to as autophagy) is currently the best understood of the three processes and has a marked impact on cellular metabolism and cell death. Owing to its evolutionary conservation, more than 30 genes and their respective autophagy related (Atg) proteins are responsible for the formation of functional molecular complexes that constitute the core mammalian pathway of autophagy (Ravikumar *et al*., 2010). These complexes mediate the delivery of cytosolic materials to acidic lysosomes for degradation into energy providing metabolites. Damaged cytoplasmic organelles (mitochondria, endoplasmic reticulum, Golgi apparatus etc.) can also be removed selectively via lysosomal degradation to ensure optimal cellular functionality. Therefore, autophagy can occur either selectively or non-selectively.

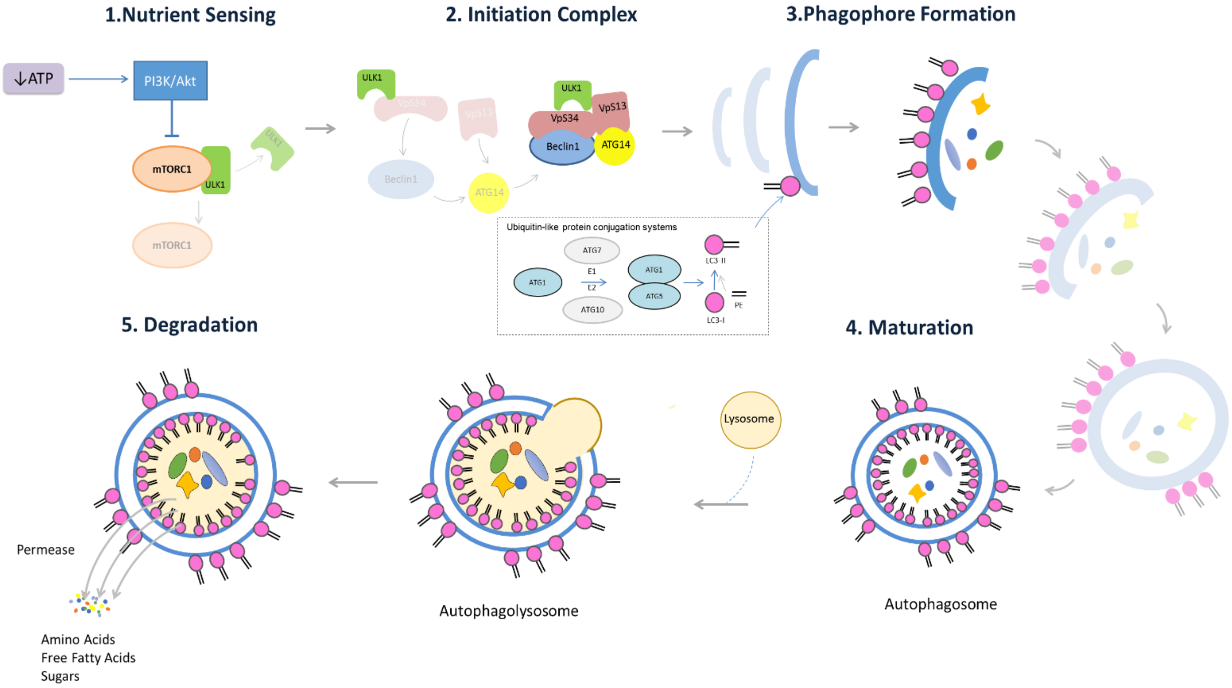

Figure 1.5. Regulation of autophagy

Both situations require the formation of double-membrane vesicles, referred to as autophagosomes, to deliver cytosolic components to the lysosomes (Fig. 1.5). Initiation of autophagosomal formation entails the generation of an isolation membrane from multiple sources such as the endoplasmic reticulum (ER), outer mitochondrial membrane and the plasma membrane (Kroemer *et al*., 2010). Although nutrient deprivation has been shown to stimulate lipid degradation, it has yet to be determined whether other stimuli such as mitochondrial or ER-stress can induce specific membrane formation from these sources. Generation of the isolation membrane is regulated by the initiation complex, referred to as the class III PI3K complex (Lefranc & Kiss 2006). Functioning of the initiation complex is controlled by a pre-initiation complex, termed the unc-51-like kinase (ULK) complex, which responds largely to alterations in cellular metabolism (Ravikumar *et al.,* 2010) (Fig. 1.5).

Nutrient signalling intricately regulates autophagosome formation through three major metabolic pathways. These include cAMP-dependent protein kinase (PKA), AMP-activated protein kinase (AMPK) and the mammalian target of Rapamycin (mTOR) (Loos *et al*., 2013). mTOR-complex 1 (mTORC1) phosphorylates two major components of the ULK complex, ULK1 and Atg13, which prevents it from initiating the formation of the isolation membrane (Yorimitsu and Klionsky, 2005) (Fig. 1.5). Therefore, mTORC1 inhibits autophagy under normal conditions, whereas starvation limits nutrient signalling to mTOR and causes de-repression of the ULK1-complex.

The subsequent depletion of ATP levels as a result of nutrient deprivation also increases ADP and AMP levels, thereby activating AMPK (Mathew and White, 2011). AMPK serves to restore cellular energy levels through autophagy by means of MTOR inhibition and direct phosphorylation of the ULK1 activation site (Green and Levine, 2014). An important function of AMPK signalling is to increase the overall metabolic efficacy of autophagy. This is accomplished by minimising ATP-usage by unnecessary processes (Mihaylova & Shaw 2011). Therefore, by simultaneously increasing the bio-availability of metabolites for ATP generation and conserving ATP usage, the autophagic response to starvation becomes more efficient.

ATP synthesis is also affected by PKA signalling, which phosphorylates the mitochondrial fission related protein DRP1 (Chang & Blackstone, 2007). Fission impairment results in a greater amount of mitochondrial fusion to generate large mitochondrial networks, increasing ATP production (Galloway *et al*., 2012). Fusion of mitochondria also decreases the amount of cytosolic ATP consumed by individual mitochondria to maintain their membrane potential (Liu *et al*., 2009). The increased potential of the mitochondrial network to produce ATP, together with conservational signalling from AMPK further enhances the metabolic efficiency of autophagy.

During mTOR inhibition, mTROC1 dissociates form the ULK-complex, leading to dephosphorylation of ULK1 and Atg13 (Aki *et al*., 2013) (Fig. 1.5). Catalytic activation of ULK1 ensues, resulting in ULK-mediated phosphorylation of Atg13 and FIP2000 (Singh & Cuervo, 2011). The activated ULK-complex elicits its kinase activity on key components of the class III

PI3K initiation complex (Ravikumar *et al.,* 2010). Composed of Vps34, Beclin 1, Vps15 and ATG14L, the formation of this multi-domain complex is necessary for the allosteric activation of Vps34 (Kroemer *et al.,* 2010). Importantly, Vps34 targets phosphatidylinositol to generate phosphatidylinositol-3-phosphate (PI3P) on the isolation membrane (Yorimitsu and Klionsky, 2005). This is the only enzyme that performs such a function in eukaryotes and is crucial to autophagosomal formation.

Attachment of PI3P to the isolation membrane leads to the recruitment of proteins involved in the elongation reaction. Elongation is mediated by two ubiquitin-like protein conjugation systems that function together to generate LC3-II, a proteolipid molecule which makes fusion of the autophagosome to the lysosome possible (Amaravadi *et al*., 2011). LC3-II is composed of protein light chain 3-I (LC-3) and a phosphatidylethanolamine (PE) lipid (Green and Levine, 2014). LC3 is lipidated through the actions of a ubiquitin like protein (UBL) cascade which involves the E1 (ATG7) and E2 (ATG3) ligases as well as ATG4 protease activity (Amaravadi *et al.,* 2011). Proteolytic cleavage of LC3 by ATG4 produces the LC3-I precursor molecule which is bound by the E1 ligase and transferred to the E2 ligase (Kroemer *et al.,* 2010). A different E2 ligase, ATG10, together with E1 facilitates ATG12-ATG5 complex formation which binds to ATG16L1 to initiate E3 ligase activity (Ravikumar *et al.,* 2010).

Finally, the ATG12-ATG5 -ATG16L1 complex facilitates conjugation of LC3-I to PE, producing LC3-II to conclude the elongation reaction (Green & Levine, 2014). Both LC3-II and the ATG12-ATG5-ATG16L1 complex associate with the elongating membrane, although only LC3-II remains attached to the fully matured autophagosome (Ravikumar *et al.,* 2010). Fusion with acidic lysosomes is now possible, allowing for the degradation of cytoplasmic proteins, lipids and carbohydrates into their respective biosynthetic substrates (Fig. 1.5). These substrates are commonly amino acids (AA) and free fatty acids, which feed into the TCA cycle and ETS (Fig 1.3.2).

Degradation has been shown to occur selectively, relying on the interaction between LC3-II and adaptor moieties present on protein aggregates and damaged mitochondria. The best characterised molecule in this process is the p62/SQSTM1 adaptor molecule, which associates with ubiquitinated proteins and interacts with LC3-II during phagophore development to ensure selective engulfment and degradation (Komatsu & Ichimura, 2010).

1.3.2 The role of autophagy in tumourigenesis and apoptosis

It has been proposed that the varying levels of autophagy found in different cancer types may not be as paradoxical as initially conceived. Given that different tissue types have varying levels of autophagic flux i.e. the rate of protein degradation through autophagy (Mizushima *et* *al*., 2004), the level of autopahgic flux present at a given time in tumour cells can be influenced by a majority of factors, including the extent of tumour malignancy, initial basal autophagic flux of pre-cancerous tissue and the experimental method used to assess autophagy (Zhou *et al*., 2012). Seeing as metabolic demand drives initiation of this system, it is possible that autophagosome formation and protein degradation occurs at different rates in different tissue types. This also holds true in the context of tumourigenesis, with autophagic flux possibly being upregulated or decreased in relation to the amount of tumour growth occurring over time (Galluzzi *et al*., 2014).

Pioneering work by Karantza-Wadsworth *et al*., (2007) has demonstrated the protective role of autophagy in maintaining genome integrity in epithelial cells, with an increase in DNA double stranded breaks and gene amplifications observed in beclin1$^{-/+}$ knockout models. Furthermore, cells in which both autophagy and apoptosis were inhibited (through silencing of Beclin-1 and BCL-2) displayed increased susceptibility to undergo necrosis, whereas BCL-2 silencing in autophagy competent cells displayed greater resistance to cell death following metabolic stress. However, when considering that p53 deletions are commonly observed in many cancer types, it can be argued that loss of autophagy likely operates as a secondary driver of tumorigenesis, allowing uncontrolled proliferation to occur following genome instability (Mathew *et al*., 2007). This is further supported by the work of Shimizu *et al*., (2004), wherein double knockout Bax$^{-/-}$ and Bak$^{-/-}$ mouse embryonic fibroblasts displayed a massive surge of autophagy after etoposide induced DNA damage, followed by delayed cell death.

Conversely, the inhibition of autophagy in HeLa cancer cells under nutrient limiting conditions resulted in accelerated cell death onset, which could be delayed by the silencing of either Bax, Bak or caspases 3 and 8, indicating MOMP associated apoptosis (González-Polo *et al*., 2005). Interestingly, the stage at which autophagy is inhibited has been shown to alter cell morphology before undergoing apoptosis. Upstream inhibition of autophagy during the initiation phase by silencing of beclin1 or ATG5 diminishes vacuole formation, with cells displaying classical type I apoptotic morphological features such as membrane swelling and blebbing (González-Polo *et al*., 2005). In contrast, blocking the fusion of autophagosomes with lysosomes by the addition of lysosomal inhibitors (such as chloroquine or bafilomycin A) cause autophagic vacuoles to accumulate, resulting in the manifestation of a mixed type I and type II morphology before death (Boya *et al*., 2005). Therefore, the inhibition of autophagy at either early or late stages of the process, may lead to apoptosis due to the failure of cells to adapt to nutrient limiting conditions.

The detrimental consequences of autophagy inhibition in healthy cells, compared to the variable outcomes in cancer cell lines and *in vivo* models, indicates that although autophagy deficiency may not be a prerequisite for tumour formation, the induction thereof could be invaluable to the uphold of tumour metabolism and progression. A comprehensive comparison between the basal autophagic flux of different cancer types at different progression levels would therefore yield valuable insights into the detrimental consequences of its modulation and requires further research focus.

1.3.3 Autophagic flux modulation in the clinical setting

Seyfried *et al*., (2015) have proposed that the current standard of care treatment for GBM patients are counterintuitive and supports tumour recurrence and progression by enhancing glucose and glutamine availability. Given the evidence supporting the involvement of autophagy in maintaining cancer metabolism and the upregulation of autophagy following chemotherapy, there are currently several early phase clinical trials investigating the effect of coordinate autophagy modulation as a means of cell death sensitisation in GBM.

The addition of chloroquine to conventional treatment has proven to double the survival time of GBM patients to a mean of 24 months, although patient quality of life was severely constrained due to the toxic side effects of excessive chloroquine use (Sotelo *et al.,* 2006; Briceno *et al.*, 2006). However, Amaravadi *et al.,* (2014) have determined effective dosages of hydroxychloroquine to safely achieve autophagy inhibition in GBM patients. Unfortunately, no significant increase in survival was observed for the patient cohort receiving adjuvant therapy with TMZ, stressing the need for less toxic autophagy inhibitors to be used in conjunction with chemotherapy as well as more sensitive techniques to determine the efficacy of chemotherapeutics.

1.4 Characterisation of autophagic flux and mitochondrial dynamics

Systems biology is the study of interactions between all levels of cellular organisation, such as gene expression, protein interactions and metabolic pathways, that contribute to a phenotype of interest. It strives to achieve more than a description of how individual components function, but rather aims to understand how the interplay between different systems allow cells to operate holistically (Mast *et al.,* 2014). This usually involves the utilisation of quantitative experimental methods in order to construct mathematical models capable of predicting cellular responses. The following section will address how components of the autophagic and mitochondrial systems can be better quantified in order to be more suitable for a systems-based model of glioma metabolism.

1.4.1 Quantifying autophagic flux

Although current studies and clinical trials that make use of autophagy modulators show much promise for chemotherapeutic sensitisation, an accurate determination of the extent to which the metabolic efficiency of autophagy is altered by these modulators has yet to be conducted. This can be attributed to the experimental methods employed, which mainly involve Western blotting to assess LC3-II and p62 protein expression and microscopy based techniques such as fluorescence microscopy or transmission electron microscopy (TEM) to quantify the number of autophagosomes present in cells or tissue samples. Though effective to determine the presence of vacuolar accumulation in response to inhibition, utilizing stagnant autophagolysosome counts as a measure of autophagic activity does not portray the true kinetics of this system.

According to the recently published guidelines on measuring autophagic flux by Klionsky *et al.,* (2016), autophagic flux is defined as a measure of autophagic degradation activity. Hence, assessing the amount of autophagolysosomes or LC3-II expression present at a single point in time only indicates that autophagic vacuoles are present, but not the specific turnover rate necessary to achieve degradation. This aspect becomes extremely important in the clinical setting when trying to determine whether autophagy inhibition has been successfully achieved in patient tumours. As is evident from the clinical trials by Amaravadi *et al.,* (2014), inhibitor concentrations derived from TEM based autophagolysosome counts in peripheral blood mononuclear cells did not prove effective in enhancing patient survival time through combination therapy (Fig. 1.7).

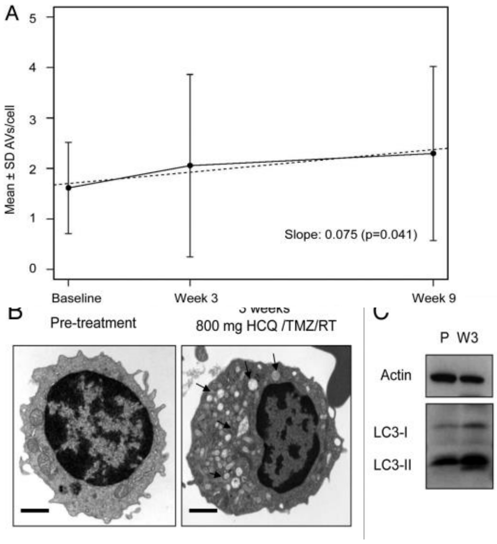

Figure 1.6. Clinical assessment of autophagy modulation. Evidence of autophagy inhibition in patients treated with Temozolomide (TMZ), radiation (RT), and hydroxychloroquine (HCQ) (Amaravadi *et al.,* 2014). (A) Number of autophagic vacuoles (AVs)/cell. (**B**) Representative electron micrographs from a patient treated with chemoradiation and HCQ 800 mg/d for 3 weeks. Arrows indicate AVs. (C) Immunoblotting against LC3 in the lysates of PBMC obtained from the same patient in (B). P, pre-treatment; W3, 3rd week of treatment.

In order to modulate the metabolic efficiency of autophagy in diseases such as cancer, it is necessary to attribute the same kinetic principles of biochemical pathways to that of the autophagic pathway. Metabolic pathways generally operate in a supply-demand fashion, in which a steady state is reached when the net rate of metabolite consumption equals that of its production. According to Loos *et al.,* (2014), the autophagic system can be viewed in the same regard, wherein a steady state of autophagosome production and degradation is reached. This becomes much more apparent when considering that the autophagic system is a stepwise pathway (Fig 1.7).

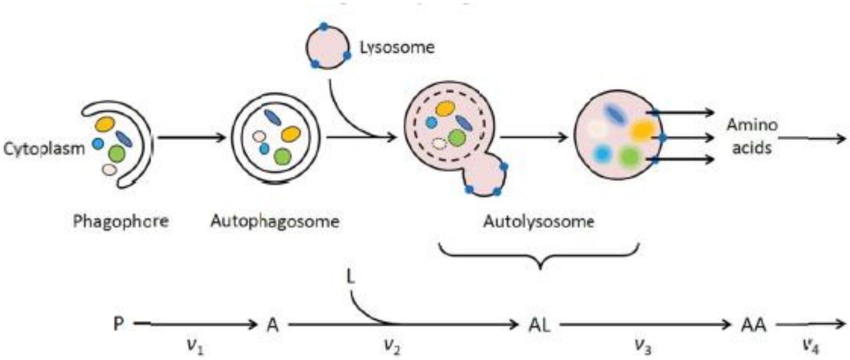

Figure 1.7 Rate attribution to the multistep autophagic pathway.

In a multistep metabolic pathway (Fig 1.7), each individual step occurs at a particular rate *v*. Together, each step is responsible for maintaining a constant flow of material through the pathway. The flux is then the quantitative measure of the rate of this flow during steady state. The autophagosome flux can therefore be quantified experimentally through complete inhibition of one of these steps, for example inhibiting lysosomal fusion, and measuring the initial accumulation rate of the step specific substrate, in this case the amount of autophagosomes accumulated (Loos *et al.,* 2014).

Implementation of such an analysis in the context of cancer metabolism will make determining the exact amount of autophagic modulation necessary to decrease its metabolic efficiency possible, thereby enhancing therapeutic outcome.

1.4.2 Criticality in mitochondrial networks

Assessing the morphological properties of mitochondria requires the integration of both spatial (structural and topological) and temporal (organellar dynamics) aspects. The term mitochondrial ‘network’ therefore refers to the collective mitochondrial dynamics which culminate in the self-organised spatiotemporal behaviour observed under certain conditions (Sornette, 2000). This definition serves to avoid confusion with the description of a network as a set of nodes and vertices as used in graph theory. Mitochondrial networks must also hold the properties of robustness and elasticity, having the ability to continue respiring under conditions of varying substrate availability and adapt the rate of energy production necessary to meet cellular metabolic demands.

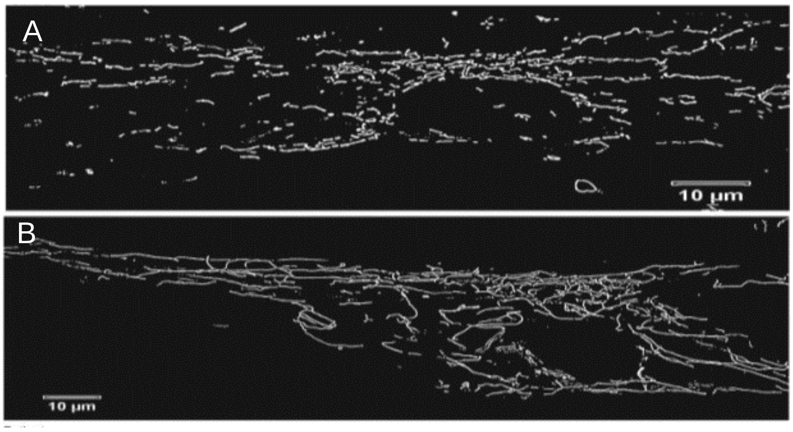

Figure 1.8. Mitochondrial networks of A) Parkin wild type human fibroblasts and B) Parkin mutated human fibroblasts. (Mortiboys *et al.,* 2008).

In terms of structure, Koopman *et al.,* (2005) constructed an algorithm to determine the mitochondrial degree of branching or form factor of mitochondrial networks in human skin fibroblasts. This approach made use of basic fractal geometry to assess the relationship between the perimeter and area values of an entire mitochondrial network. This was subsequently adapted by Mortiboys *et al.,* (2008) to quantitatively distinguish the morphological changes between wild type and parkin mutant fibroblasts (Fig. 1.9).

As seen in Fig. 1.8 B, the degree of branching is significantly enhanced when Parkin recruitment is impaired. Although these images were obtained utilising live cell microscopy, the form factor algorithm as derived by Koopman *et al.,* (2005) does not take the dynamic nature of these networks into account.

Utilising mitochondria associated photoactivateable Green Fluorescent Protein (mito-PA-GFP), Karbowski *et al*., (2004) were able to quantify the rate at which mitochondrial fission and fusion occurs by photobleaching mitochondrial regions of interest and measuring the signal decay over time. Fusion competent mitochondria tagged with the photoconverted GFP variant would be able to fuse with neighbouring mitochondria, thereby moving out of the bleached region of interest, resulting in a subsequent decrease in signal intensity over time (Fig. 1.10).

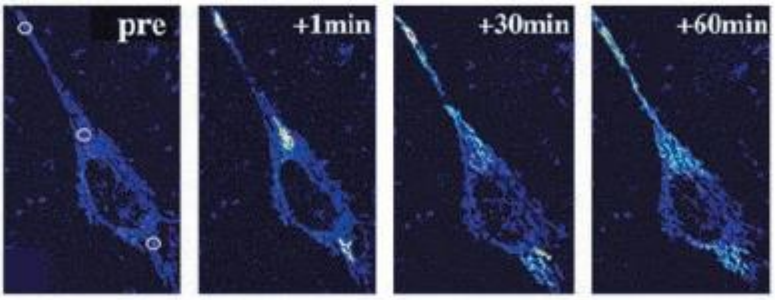

Figure 1.9. Photoactivation of three regions of interest in mito-PA-GFP transfected HeLa cells (Karbowski *et al.,* 2004).

Although the methods utilised by Mortiboys *et al.,* (2008) and Karbowski *et al.,* (2004) are capable of quantifying mitochondrial structure and dynamics respectively, the most crucial assessment of these organellar structures is overlooked: their ability to function as an autopoietic biophysical network. Importantly, the combination of structure and dynamics still fail to represent mitochondrial elasticity. This aspect will prove to be a major aspect of this thesis.

According to Aon *et al.* (2009), mitochondrial networks can be seen as a lattice-like network of nonlinearly coupled elements, the coordinated action which ultimately dictates the global cellular response. Extensive study of metabolic failure in cardiomyocytes has revealed that in response to ischemic injury, oxidative stress or substrate deprivation, mitochondrial networks behave much like other physical or chemically connected systems. According to the principles of percolation theory, subjecting non-linear networks to an excessive work load or failure of its individual parts can move a system close to a critical point (Sornette, 2000).

The conditions of a critical point entail enhanced susceptibility of a network or system to external factors and a strong correlation between its individual components (Sornette, 2000). When assessing altered membrane potential oscillations in cardiomyocytes subjected to an excessive accumulation of reactive oxygen species (ROS), coordinated depolarisation of the entire mitochondrial network was observed. This lead Aon *et al.,* (2009) to postulate that mitochondrial criticality is reached under conditions of bioenergetic instability and that such dynamic instability could be a favourable adaptation to rapid microenvironmental changes.

Although these findings certainly suggest the existence of a mitochondrial critical point, it must be stressed that critical phenomena in natural sciences commonly occur for infinitely large structures or systems. Therefore, establishing the existence of criticality within finite cellular systems remains an active area of investigation.

It remains to be elucidated whether altered mitochondrial morphology and dynamics plays an important role in the context of glioma metabolism. Furthermore, there is a lack of image processing tools capable of quantifying the extent of connectivity present in mitochondrial networks under metabolic stress and shall be addressed in this thesis.

1.5 Aims and Hypothesis

From current literature, we conclude the following: There is currently a lack of life prolonging treatment options for GBM patients. Mitochondrial respiration and autophagy are intricately involved in upholding glioma metabolism and cell death evasion. However, assessing the effects of autophagy modulation on cellular metabolism requires a better characterisation of both autophagic flux and mitochondrial bioenergetics.

We therefore hypothesised that mitochondrial bioenergetic efficiency can be decreased by coordinate autophagy modulation in order to enhance cell death susceptibility in glioma cells.

Our hypothesis will be assessed by the following objectives/aims:

- Determining the amount of autophagy modulation necessary to sensitise glioma cells to chemotherapy.
- Assessing whether a relationship exists between autophagy modulation and mitochondrial bioenergetics in terms of topology, dynamics and electron transport chain efficiency.
- Determining the extent of mitochondrial respiratory impairment necessary to achieve cell death sensitisation.
- Assessing the relationship between morphological regulators, cell death machinery and cellular metabolism.
- Achieving better characterisation of mitochondrial morphometrics in the context of GBM metabolism.

Chapter 2: Materials and Methods

2.1 Reagents and Consumables

2.1.1 Cell line and general consumables

Human U-118 MG (ATCC® HTB15™) grade IV astrocytoma cells were purchased from the American Type Culture Collection (ATCC) and supplemented with Dulbecco's Modified Eagles Medium (DMEM), 1% penicillin/streptomycin (PenStrep) (Life Technologies, 41965062 and 15140122) and 10% foetal bovine serum (FBS) (Scientific Group, BC/50615-HI). Media aliquots were stored at -4°C in 50ml Falcon tubes (EF4663), whilst passaging required 15ml Falcon Tubes (EF4661), which were obtained from SPL Life Sciences. Cells were cultured in 25cm^2 and 75cm^2 non-pyrogenic polystyrene flasks, purchased from Nest Biotechnology (707001 and 708001). Viability assays required the use of 48-well plates (SPL Life Sciences, 30048) and for confocal microscopy NUNC 8-well chambered cover glass dishes (155411) were purchased from Thermo Scientific. 10ml Serological pipettes were obtained from Biochom Biotech (PN10E1).

2.1.2 Treatment and transfection reagents

The autophagy modulating drugs, Hydroxychloroquine Sulfate (HCQ) and Rapamycin, as well as the chemotherapeutic Temozolomide (TMZ) were purchased from Sigma-Aldrich (1327000, R8781 and T2577 respectively). Bafilomycin A_1 was acquired from LKT laboratories (B0025). HCQ and Bafilomycin A_1 were dissolved in H_20, whist Rapamycin and TMZ was prepared in Dimethyl sulfoxide (DMSO) (Sigma-Aldrich, D2650). Lipofectamine p3000 transfection reagent (Life Technologies, L30000015) was used to transiently transfect U-118 MG cells with mitochondrial matrix targeted photoactivateable green fluorescent protein (mito-PA-GFP) (clonally expanded at the Department of Human Genetics, Tygerberg, South Africa).

2.1.3 Western Blotting Reagents

Bradford standards were derived utilizing Brilliant Blue G (27815) and bovine serum albumin (BSA) (Sigma-Aldrich, 10735078001). 12% Gels were cast using a TGX FastCast Acrylamide kit (161-0175) and transferred to 0.2 µm PVDF membranes (midi format) using Trans-Blot Turbo Transfer packs (170-4157) which were enhanced during imaging with an enhanced luminescence (ECL) kit (170-5061), purchased from Bio-Rad. Protease inhibitor tablets were purchased from Sigma-Aldrich (11873580001) and enhanced with Na_3VO_4 (s6508), PMSF (93482) and NaF (Sigma-Aldrich).

2.1.4 Antibodies

Primary antibodies for LC3, cleaved-Caspase3, cleaved-PARP and β-Actin were obtained from Cell Signalling. The mitochondrial primary antibodies OPA-1, Drp1, MFN-1, MFN-2 and secondary antibodies (anti-rabbit and anti-mouse) were purchased from Abcam. Antibody details are outlined in the table below.

Table 2-1. List of antibodies utilised in this study.

Primary Antibodies	Company	Host	Size (kDa)	Dilution
LC3-II	Cell Signalling (2775)	Rabbit	18-kDa	5µL:5000µL
Cleaved-Caspase3	Cell Signalling (9664)	Rabbit	18-kDa	5µL:5000µL
Cleaved-PARP	Cell Signalling (9541S)	Rabbit	89-kDa	5µL:5000µL
SQSTM1/p62	Cell Signalling (56416)	Rabbit	62-kDa	5µL:5000µL
B-Actin	Cell Signalling (4970)	Rabbit	45-kDa	1µL:5000µL
OPA-1	Abcam (ab157457)	Rabbit	89-kDa	5µL:5000µL
Drp-1	Abcam (ab56788)	Mouse	89-kDa	5µL:5000µL
MFN-1	Abcam (ab57602)	Mouse	89-kDa	5µL:5000µL
MFN-2	Abcam (ab56889)	Mouse	89-kDa	5µL:5000µL
TOMM20	Abcam (ab78547)	Rabbit	19-kDa	5µL:5000µL
Secondary Antibodies	**Company**	**Host**	**Dilution**	
anti-rabbit IgG HRP	Abcam (7074S)	Donkey	1µL:5000µL	
anti-mouse IgG HRP	Abcam (7076S)	Donkey	1µL:5000µL	

2.1.4 Oxygraph reagents

High resolution respirometry was carried out using the Oroboros Oxygraph-2k system. All compounds for the mitochondrial respiration medium (MiRO5) were purchased from Sigma-Aldrich unless otherwise specified. MiRO5 medium consisted of EGTA (E4378), $MgCl_2$ (M8266), Lactobionic acid (153516), Taurine (T0625), KH_2P0_4 (Merck, 104873), HEPES (H7523), D-Sucrose (84097) and BSA (10735078001). The substrates, uncouplers and inhibitors used during the coupling control protocol were supplied by Sigma-Aldrich, including L-Glutamic acid (G1626), L-Malic acid (M1000), Pyruvic acid (P2256), Succinate (S2378), Ascorbate (A4034), Tetramethyl-p-phenylenediamine dihydrochloride (TMPD, T3134), Adenosine 5'diphosphate (ADP, A2754), Carbonyl cyanide m-chloro phenyl hydrazine

(CCCP, C2759) and Antimycin A (A8674). Cell permeabilisation was achieved through titration of Digitonin (D141).

2.1.5 Reagents for Lactate Determination

Extracellular L-Lactate was measured by means of a LDH, NAD^+ linked assay. The sample buffer (pH 7.6) consisted of HEPES (150 mM, Sigma-Aldrich) and $MgSO_4$ (15 mM, Merck), made up in dH_2O. NAD^+(4 mM, Sigma-Aldrich) and LDH (4 U/mL, Sigma-Aldrich) was added, together with 320 mM hydrazine (Sigma-Aldrich).

2.2 Experimental Procedures

2.2.1 Cell line maintenance

U-118MG cells were incubated in a humidified incubator (SL SHEL LAB CO_2 Humidified Incubator) in the presence of 5% CO_2 at 37°C. Cells were seeded for experiments when reaching 80% confluency. Passaging entailed rinsing the cell monolayer with DMEM, followed by brief incubation with 0.25% Trypsin-ethylene-diaminetetra-acetic acid (EDTA) until complete detachment of cells was observed. Cells were then centrifuged at 1500 rpm for 3 minutes and reseeded at the following densities; $5X10^3$ U-118 cells per 48 well plate, $5x10^3$ cells per 8 chamber dish, $10X10^6$ U-118 MG (ATCC® HTB15™) cells per $25cm^2$ (White Head Scientific, 500033) and $75cm^2$ tissue culture flask.

2.2.2 Cell Viability Assay

Mitochondrial reductive capacity was measured using water soluble tetrazolium bromide (WST-1) (Roche, 11644807001). Cells were seeded in 48-well plates, whereafter cell culture media containing treatment reagents was aspirated and replaced with 200uL of fresh media. 5uL of WST-1 was added to each well and incubated at 37°C for 80 minutes, after which the 48-well plate was placed in a multiplate reader (EL-800, Bio-Tek instruments Inc.) and absorbance values read at 480 nm. Reductive capacity was calculated in percentage relative to the untreated control group.

2.2.3 Transient Transfection

Cells were seeded at $5x10^3$ U-118 MG cells per 8 chamber dish and transfected with a mitochondria associated photoactivatable green fluorescent protein (mito-PA-GFP) plasmid prior to treatment utilising Lipofectamine ®3000 transfection reagent (Life Technologies, L30000015). Sufficient transfection efficiency was achieved using a plasmid concentration of 200 ng/µL, diluted in Opti-MEM containing P3000 solution (2 µL/µg DNA). The DNA-P3000 complex solution was co-incubated with Lipofectamine® 3000 solution in a 1:1 ratio for 5 minutes to allow for stable complex formation. Cells were incubated with Transfection media (10 µL per chamber) for 48 hours, after which treatment and imaging took place.

2.2.4 Confocal Microscopy

2.2.4.1 Photoactivation Assay

In order to determine the rate at which mitochondrial fission and fusion occurs, the spread of mito-PA-GFP from a subset of mitochondria throughout the mitochondrial network was tracked over time, as previously described by Karbowski *et al*. (2004), using a Carl Zeiss Confocal Elyra S1 microscope with LSM 780 technology. Transfection with mito-PA-GFP and staining with tetramethylrhodamine-ethyl ester (TMRE) (Life Technologies, T669) allowed for visualisation of the mitochondrial network.

Following transfection, U-118MG cells ($10x10^3$ U-118 MG cells per 8 chamber dish) were treated accordingly and stained with TMRE. For each cell, 2-3 small regions of interest (ROI) of the cross-section area in a single focal plane was selected for photoactivation. Once selected, these regions were exposed to 403 nm laser stimulation at 100% intensity, resulting in the activation of mito-PA-GFP observed at 60x magnification. Following the more recent guidelines by Karbowski *et al.,* (2014), only regions that displayed an increase in signal intensity of at least twice that of the initial intensity were tracked over time. Mito-PA-GFP signal distribution out of the ROI was observed under 488 nm excitation and a live cell time lapse was constructed with images acquired every second for 300 cycles (10 minutes) and an iteration speed of 15. Image processing was conducted with ZEN software (black edition, 2011, version 7.04.287). A detailed example of how signal decay results from individual fission and fusion events are illustrated in Fig. A2 (Appendix A, Supplementary Results).

2.2.4.2 Morphometrics

To assess the morphometric characteristics of mitochondrial networks, live cell confocal microscopy was conducted with z-stacks taken every 30 seconds for 10 minutes (Carl Zeiss LSM 780) in order to produce three dimensional mean intensity projections for image analysis. TMRE working solution (1:1000 dilution) was prepared by adding 1 µL of TMRE to 1 mL of growth media. Prior to imaging, media was removed followed by treatment with 200 µL TMRE working solution. Image processing was conducted in Wolfram Mathematica (Version 10.2).

A list of all functions and algorithms used have been included in Appendix A, image lists were binarized using the built in “Morphological Binarize” function and thresholded accordingly. The function “ClusterCount” assessed the number of clusters present within the network, whilst “ClusterAreas” and “ClusterPerimeters” assessed the total area and geometric perimeter of each cluster. In order to correct for non specific thresholding, the functions “ExtractLargestCluster”, “DeleteSmallestCluster” and “DeleteLargestCluster” were used to delete excessively small or large clusters which did not coincide with the mitochondrial network.

To assess the degree of connectivity within the mitochondrial networks, the total number of vertices (determined with "CountVertices") was devided by the total amount overlapping vertices (determined with "ConnectedComponents") within a graph like structure (processed with "MorphologicalGraph"). To determine whether cluster values coincide with circular or filamentous structures, a power law function was fit to a log[Area] log[Perimeter] plot. Processing of control image lists are given in Appendix A (A3. Image Processing).

2.2.5 Western Blotting

2.2.5.1 RIPA (Radio-Immunoprecipitation) Buffer for Protein Extraction

RIPA buffer consisted of 20 mM Tris-HCl (pH 7.4), 137 mM NaCl, 10% Nonidet-P40 and 10% Na-deoxycholate. On the day of protein extraction, 42 µL of Complete EDTA-free protease inhibitor tablet solution was added to 1 mL of RIPA, followed by addition of 1mM PMSF, 1 mM Na_3VO_4 and 1 mM NaF phosphatase inhibitors. 25 cm^2 flasks were rinsed with PBS and incubated with 200 µL RIPA solution for 5 minutes on ice. Thereafter, cells were scraped, transferred to 2 mL Eppendorf tubes and sonicated at an amplitude of 5mA. The supernatant was decanted into a fresh tube and centrifuged at 8000rpm at 4°C for 10 minutes. Cell lysates were decanted into a third set of tubes and stored at -20°C.

2.2.5.2 Bradford Protein Determination

Protein concentration was determined using a Bradford Assay (Bradford 1976). The Bradford stock solution consisted of 500 mg Coomasie Brilliant Blue G250 and 500ml phosphoric acid, dissolved in 95% ethanol and adjusted to a final volume of 1 L with ddH_2O. A 1:5 working solution was used for protein determination. A BSA (200 µg/mL) standard curve was constructed in the range of 0-20 ug/mL to determine protein concentrations. For the samples, 5uL lysate was diluted in 95uL dH_2O. 900uL of Bradford working solution was added to each standard or sample tube, vortexed briefly and incubated at room temperature for 5 minutes. Absorbance values were read at 595nm using a Cecil C8 2021 spectrophotometer.

2.2.5.3 Sample Preparation

5 ml of Laemmli's loading buffer was prepared by diluting 1 ml Tris-HCL (0.5M; pH 6.8), 0.8 ml glycerol, 1.6 ml of 10% SDS (sodium dodecyl sulfate), and 0.4 ml of 0.05% Bromophenol blue in dH2O. A working solution of Laemmli's loading buffer was prepared by adding 150 µl of β-mercaptoethanol to 850 µl of Laemmli's loading buffer and by mixing thoroughly. Appropriate volumes (µl) of protein sample were added to Eppendorf tubes so as to obtain 50 µg of each protein sample per tube. The appropriate volume of Laemmli's loading buffer

(1/3 the volume of protein) was added to each sample. Samples were boiled for 5 minutes at 95˚C, centrifuged briefly, and placed immediately on ice.

2.2.5.4 Sodium-Dodecyl-Sulfate-Polyacrylamide Gel Electrophoresis (SDS-PAGE) and Western Blot Analysis

The gels used for SDS-PAGE consisted of a 12% resolving and 4% stacking component, which were prepared as per the manufacturer's protocol (Bio Rad Mini-Protean ® TGX ™ fast cast system). Gels were set at room temperature and secured onto an electrode assembly, which was placed inside a Mini-Protean Tetra cell tank. The buffer chambers were filled with running buffer (diluted 1:10 with dH_2O). 3 µl of Blue DyeX protein marker was loaded into the first well, followed by the appropriate sample volume. After connecting the electrode assembly to a power supply (BIO-RAD Power Pac 1000), proteins were separated at 100V for approximately for 20 minutes through the stacking component, followed by a charge of 150V for approximately 40 minutes, with a constant current of 400mA. Proteins were transferred from the gel onto a PVDF (polyvinydilene difluoride) membrane using BIO-RAD Trans-Blot transfer packs and a BIO-RAD Trans-Blot turbo transfer system. Membranes were blocked for 60 minutes in 5% non-fat milk made up in 1X TBS-T (Tris-buffered saline and 1% Tween20) for 1 hour to reduce non-specific binding, followed by a 3 X 5 minutes rinse step with 1X TBS-T. Incubation with primary antibodies overnight at 4˚C ensued using the dilutions outlined in table 2.1. Membranes were subsequently rinsed in TBS-T for 3 X 5 minutes and incubated in the appropriate secondary antibody for 60 minutes at room temperature. After another 3 X 5 minutes rinse step, the membrane was treated with 200 µl of enhanced chemiluminescence (ECL) reagent (peroxide buffer and enhancer solution prepared in a 1:1 ratio). Band intensities were detected with a BIO-RAD Chemidoc MP imaging system using *Image Lab* software (version 4.1). Band intensities of proteins were expressed as a percentage relative to band intensities of untreated control cells.

β-actin was used as a loading control for all membranes and TOMM20 was used in conjunction to serve as an additional loading control for the mitochondrial proteins Mfn1, Mfn2, Opa1 and Drp1. When required, membranes were stripped for 5 minutes with 0.2 M NaOH (sodium hydroxide) and rinsed for 3 X 5 minutes with TBS-T, followed by a blocking step of 1 hour with 3% non-fat milk. Incubation with either B-Actin or TOMM20 primary antibody (1:1000) occurred overnight at 4˚C. Membranes were incubated in anti-rabbit HRP linked secondary antibody and developed with ECL reagents as previously described.

2.2.5.7 Bafilomycin A1 Treatment and Western Blot Analysis of LC3 and P62

Bafilomycin A1 impairs the fusion of lysosomes with autophagosomes by inhibiting H^+ATP-ase activity. A 100 µM stock solution was prepared in DMSO and diluted to 400nM in normal growth media. Cells were seeded in 25 cm^2 flasks at a density of $10X10^6$ cells and treated accordingly, followed by incubation with 400nM Bafilomycin 4 hours prior to protein extraction. RIPA protein extraction, Braford analysis, sample preparation and Western Blot analysis of LC3, P62 and B-Actin was performed as described above.

2.2.6 Oxygraph Analysis

2.2.6.1 Air Calibration

A two-point calibration was conducted for each polarographic oxygen sensor (POS) at air saturation levels with the experimental temperature set to 37°C. Continuous stirring of sample free Miro5 respiration medium in contact with air allowed for air saturation levels to be reached. 2,5mL of medium was added to each chamber with the stirrers switched on, followed by the slow insertion of the stoppers (containing the injection capillaries) to their volume calibrated position. After siphoning off the excess media, the stoppers were lifted using the stopper spacer tool in order to leave a gaseous volume above the liquid medium for final air calibration. Stabilization was reached after 30 minutes, with the oxygen consumption slope reaching close to an average of ±1 $pmol.s^{-1}.ml^{1}$ at an oxygen concentration of 200 nmol/ml. Using the DatLab software (version 6.1.0.7), a section of the oxygen slope was selected in real time and marked as R1 for air calibration.

2.2.6.3 Cell Permeabilisation

After trypsinisation, cells were counted and resuspended in Miro5 solution. A total of 500 000 cells were added to each O2K chamber containing 2mL of Miro5 medium. After stabilisation of the O_2-slope, Succinate (10 mM), ADP (5 mM) and Rotenone (0.5uM) were added. 30 minutes was necessary for adequate stabilisation to occur. In order to determine an effective permeabilisation concentration, incremental titrations of 0.5 mM Digitonin followed. After the first titration, no increase in oxygen consumption was observed. However, a marked increase was caused by the second 0.5 mM titration. The third Digitonin titration, accumulating to 1.5 mM in total, resulted in a steady decline in the O_2-slope, indicating that permeabilisation was achieved. In order to assess whether mitochondrial membrane integrity was compromised, 1 mM of cytochrome-c was added. No increase in oxygen flux was observed, indicating that 1.5 mM of Digitonin was a safe concentration to use for permeabilisation. The corresponding O_2 consumption trace is provided in Appendix A (Supplementary Results, Fig. A1).

2.2.6.4 Coupling Control Protocol

The Electron Transfer System (ETS) and oxidative phosphorylation (OXPHOS) capacity was determined through stepwise titration of specific substrates and inhibitors. In accordance with the Oroboros guidelines (Gnaiger, 2014), the resulting O_2 flux values were utilized to calculate Routine respiration (R), the amount of proton leak (LEAK-state), OXPHOS capacity through Complex I and Complex II, Residual Oxygen Consumption (ROX) and complex IV activity for normalisation. Following permeabilisation with 1.5 mM Digitonin, Pyruvate (5 mM), Malate (2 mM) and Glutamate (10 mM) were added to determine the LEAK state. Complex I activity was measured through addition of 2 mM ADP and combined Complex I & II activity was determined by titration of 10 mM Succinate in the presence of ADP. ETS capacity was determined through subsequent titration of 0.5 µM CCCP until a maximal oxygen flux was reached, which was taken as the maximal ETS capacity. Correcting for ROX involved the addition of complex III inhibitor Antimycin-A and the resulting flux value was subtracted from all final values. The ROX-corrected values were then normalized to the total amount of mitochondria represented by total complex IV activity, measured by addition of TMPD (0.5 µM), which was kept in a reduced state by co-titration with Ascorbate (2 mM (Larsen *et al*., 2012).

2.2.7 Lactate Determination

U-118MG cells were seeded in 6 well plates at a density of 10 X 10^5 cells per well. After treatment, 2 mL of culture medium was taken from each well for lactate determination. Protein extraction and Bradford quantification was performed as previously described. Lactate determination required addition of 5 µl sample or lactate standard (0-5 mM) to 95 µl PBS (1 mM), NAD^+ (4 mM), LDH (4 U/mL) and hydrazine (320 mM) in a 96-well plate, incubated for 90 minutes at 37°C. Absorbance values were read at 340 nm using a BioTek Powerwave 340 spectrophotometer.

2.2.8 Proposed treatment groups

This study will make use of 5 treatment groups in addition to the control. The effects of Rapamycin, HCQ and TMZ will be assessed in isolation, with treatment times and drug concentrations determined through WST-1 viability assays. Following viability assays, two combination groups will be assessed. The first being HCQ in combination with TMZ (HT) and the second entailing pre-treatment with Rapamycin following the HT treatment regimen.

Chapter 3: Results

3.1 The effect of autophagy modulation on cell viability

WST-1 viability assays were performed after incubating glioma cells with varying concentrations of Rapamycin (RAPA) for 6 hours and Hydroxychloroquine (HCQ) for 6 and 12 hours.

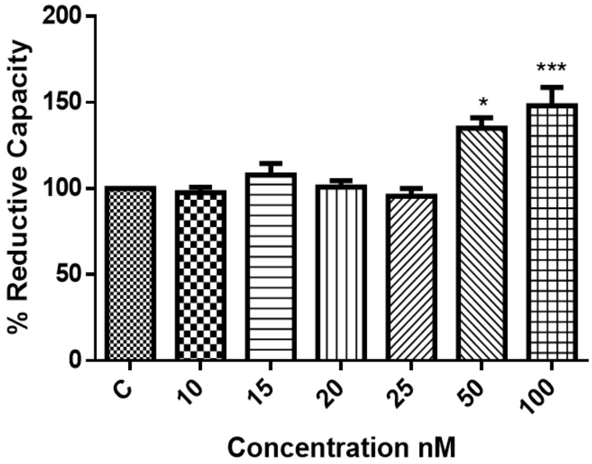

Figure 3.1. WST-1 viability assay of U-118 MG cells treated with 10, 15, 20, 25, 50 and 100 nM of Rapamycin for 6 hours. n=3, *p <0.05 vs Control, ***p<0.001 vs Control.

Rapamycin significantly enhanced reductive capacity at concentrations of 50 and 100 nM (135.0 ± 6.04%; 148.1 ± 10.66%, p<0.05), whilst moderate concentrations (10-25 nM) left cell viability unchanged when compared to the control (Fig. 3.1).

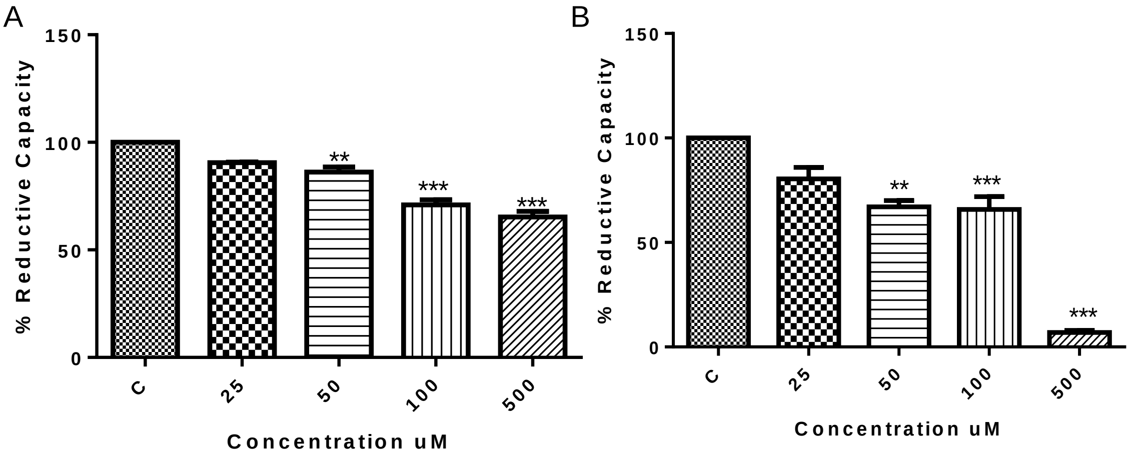

Figure 3.2. WST 1 viability assays of U-118MG cells treated with 25, 50, 10C and 500μM of hydroxychloroquine (HCQ) for A) 6 hours and B) 12 hours. n=3, **p < 0.01 vs Control, ***p<0.001 vs Control.

A significant decrease in reductive capacity was observed after 6 hours of 50, 100 and 500 µM HCQ treatment (86.22 ± 2.37%, 70.96 ± 2.29% and 65,27 ± 2.70% respectively, p<0.01) (Fig. 3.2 A), with exacerbated effects observed after prolonged incubation for 12 hours (67.09 ± 3.03%, 65.77 ± 6.20%, 6,96 ± 0.96%, p<0.01) (Fig. 3.2 B).

A 6 hour incubation period in the presence of 50 nM of Rapamycin and 50 µM of HCQ was therefore chosen for all subsequent treatments. Of note, incubation with Rapamycin followed by HCQ resulted in a significant decrease in reductive capacity compared to that observed for the 50 µM HCQ group (75.95 ± 2.91%, p<0.01)

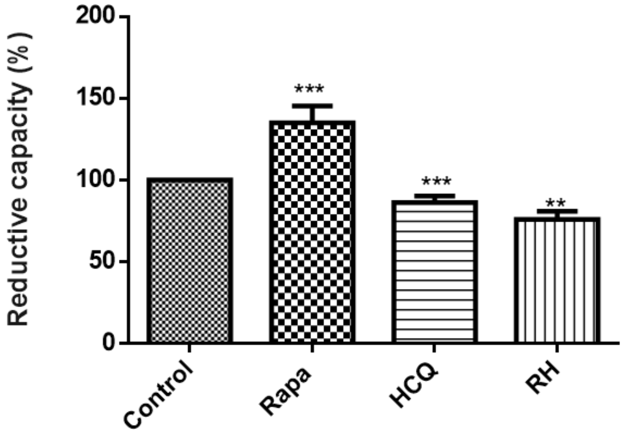

Figure 3.3. WST 1 viability assays of U-118MG cells treated with 50 nM Rapamycin (Rapa) and 50 µM Hydroxychloroquine (HCQ) for 6 hours respectively and in combination (RH). n=3, **p < 0.01 vs Control, ***p<0.001 vs Control.

3.2 The effect of TMZ on cell viability

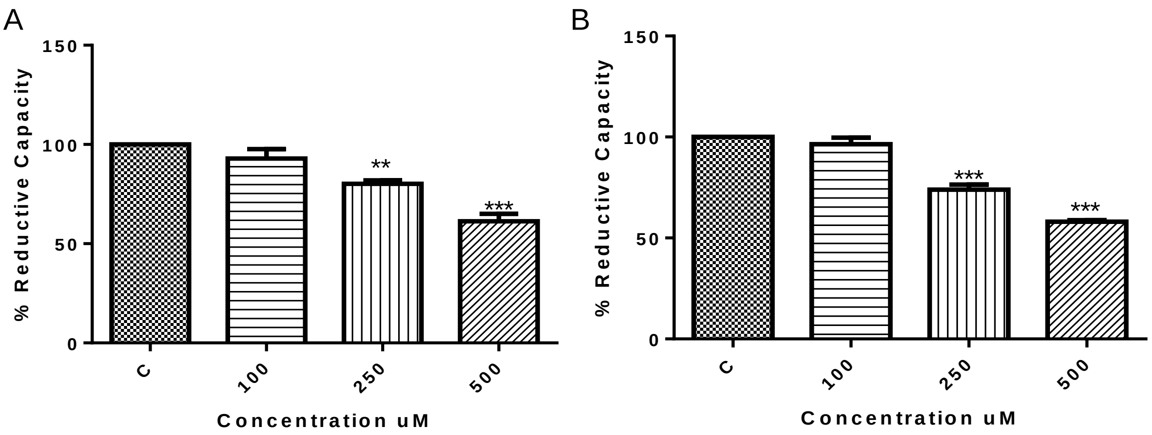

Figure 3.4. WST 1 viability assays of U-118MG cells treated with 100, 250 and 500 µM of Temozolomide (TMZ) for A) 24 hours and B) 48 hours. n=3, **p < 0.01 vs Control, ***p<0.001 vs Control.

Incubating glioma cells for 24 hours with 250 and 500 µM TMZ lead to significantly decreased cell viability (80.19 ± 1.76%, 61.34 ± 3.77%, p<0.01) (Fig. 3.4 A) when compared to the untreated control, with no additive effect observed after 48 hours (73.99 ± 2.47%, 58,02 ± 0.76%, p<0.01) (Fig. 3.4 B). This indicates that although the U-118MG cell line was sensitive to chemotherapy, failure to reach more than a 50% decrease in reductive capacity after prolonged incubation made it possible to investigate the sensitisation effects of adjuvant treatments. Three adjuvant treatment groups were investigated. The first was co-incubation of 50 µM HCQ with 250 µM TMZ for 6hours, after which 18 hours of 250 µM TMZ treatment ensued (HTMZ). The second group entailed 6 hours of RAPA pre-treatment, followed by 18 hours of 250 µM TMZ (RTMZ). Lastly, a dual modulation adjuvant group was tested, which consisted of 6 hours Rapamycin pre-treatment, followed by co-incubation of 50 µM HCQ with 250 µM TMZ for 6 hours and 18 hours of 250 µM TMZ treatment (RHT).

3.3 Rapamycin pre-treatment exacerbates HCQ mediated decrease in viability

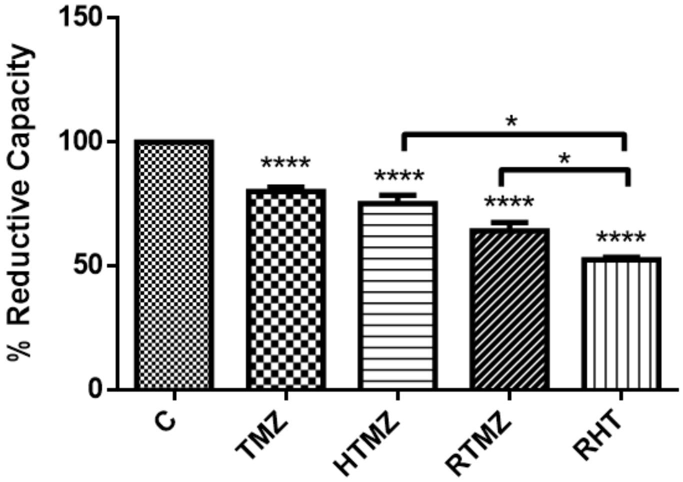

Figure 3.5. WST1 viability assay for Control, TMZ (250 µM), HCQ (50 µM) + TMZ (250 µM) (HTMZ) and Rapa (50 nM) + HCQ (50 µM) + TMZ (250 µM) (RHTMZ). N=6, ****p < 0.0001.

Combined treatment with HCQ decreased reductive capacity significantly when compared to the control (75.25 ± 3.49%, p<0.0001), although no significant difference was observed in comparison to TMZ treatment (80.19 ± 1.76%). However, pre-treatment with the autophagy inducer Rapamycin significantly decreased cell viability when compared to the TMZ group (64.26 ± 3.39%). Dual modulation proved to have the most prominent effect, with a substantial decrease in reductive capacity observed when compared to both individual modulation groups and the TMZ group (52.65 ± 1.056%, p<0.05) (Fig. 3.5). Of note, dual modulation led to a decrease in the percentage reductive capacity, which was of the same level as that of cells treated for 48 hours with TMZ (250 µM). Furthermore, this sensitization effect was achieved through the use of Rapamycin and HCQ concentrations which were not inherently highly toxic to glioma cells *in vitro*.

Seeing as many clinical trials currently focus on the adjuvant use of HCQ with chemotherapy, the HCQ adjuvant group was selected in addition to the dual modulation group for further analyses.

3.4 Treatment groups based on viability data

Table 3.1 outlines the concentrations and incubation times of the 6 treatment groups of interest which were chosen for all subsequent experiments.

Table 3.1 Treatment times and concentrations to be used in all subsequent experiments

Treatment	Incubation Time	Concentration
Control	-	-
Rapamycin (Rapa)	6 hours	50 nM
Hydroxychloroquine (HCQ)	6 hours	50 µM
Temozolomide (TMZ)	24 hours	250 µM
HCQ + TMZ (HT)	HCQ + TMZ: 6 hours TMZ: 18 hours	50 µM + 250 µM 250 µM
Rapa + HCQ + TMZ (RHT)	Rapa: 6 hours HCQ + TMZ: 6 hours TMZ: 18 hours	50 nM 50 µM + 250 µM 250 µM

3.5 The effect of dual modulation on autophagic flux

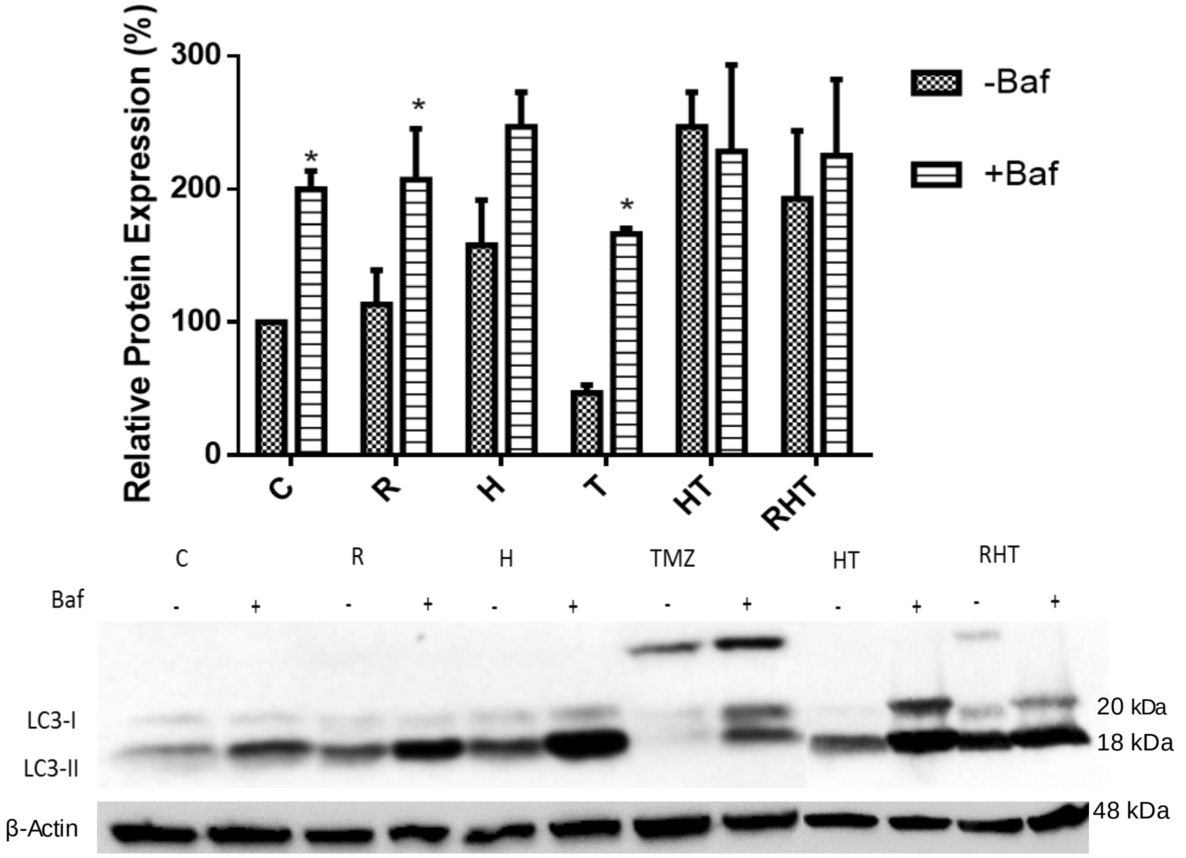

Figure 3.6. Representative Immunoblot of LC3-I and LC3-II levels before and after Bafilomycin (Baf) treatment (400 nM, 2 hours) for Control, 50 nM Rapamycin (Rapa), 50 µM Hydroxychloroquine (HCQ), 250 µM Temozolomide (TMZ), HCQ (50 µM) + TMZ (250 µM) (HT) and Rapa (50 nM) + HCQ (50 µM) + TMZ (250 µM) (RHT) treatment groups. N=3, * $p < 0.05$ vs corresponding Baf negative group.

Inhibition of lysosomal fusion through Bafilomycin (Baf) treatment results in the accumulation of autophagosomal vacuoles, which can be measured by quantifying the relative levels of LC3-II protein present in the lysate. Quantifying the change in LC3-II expression before and after incubation with Baf (400 nM) indicates the relative amount of autophagosome production present in a population of cells, serving as an indicator of the rate of protein degradation through autophagy i.e. autophagic flux. Significantly increased LC3-II protein levels were observed for the Baf positive Control (200 ± 13.70%), Rapamycin (207.10 ± 38.23%) and TMZ (166.4 ± 4.1%) groups when compared to their corresponding Baf negative expression levels, indicating basal and increased flux. No significant increase was observed in the presence of Baf for the HCQ, HT and RHT groups when compared to their Baf untreated LC3-II expression levels (Fig. 3.8.), indicative of a decreased degradation rate.

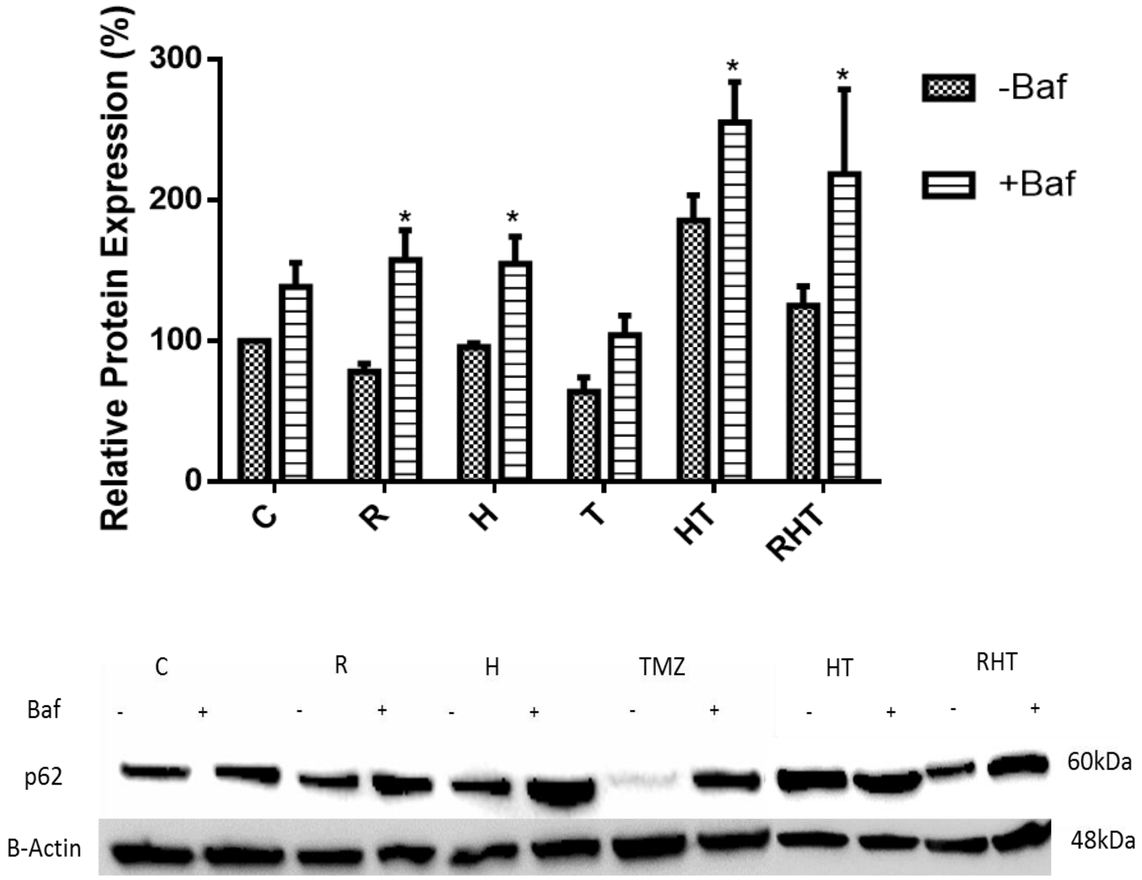

Figure 3.7. Representative Immunoblot of p62 expression levels before and after Bafilomycin (Baf) treatment (400 nM, 2hours) for Control, 50 nM Rapamycin (Rapa), 50 µM Hydroxychloroquine (HCQ), 250 µM Temozolomide (TMZ), HCQ (50 µM) + TMZ (250 µM) (HT) and Rapa (50 nM) + HCQ (50 µM) + TMZ (250 µM) (RHT) treatment groups. N=3, * $p < 0.05$ vs corresponding Baf negative group.

Accumulation of p62 protein is indicative of decreased protein degradation through autophagy, since p62 is associated with ubiquitinated proteins marked for degradation. Similar to LC3, enhanced p62 signal following Baf treatment is indicative of enhanced protein clearance through autophagy. Significant p62 accumulation was not observed in the presence of Baf for the control group, although both Baf treated Rapamycin and HCQ treatment groups showed significantly increased relative p62 expression levels (157.50 ± 21.18%, 154.90 ± 19.29%). TMZ did not alter p62 degradation, although less p62 expression was observed for Baf untreated cells compared to control (51.08 ± 2.99%). However, pre-treatment with HCQ enhanced p62 accumulation in both the Baf untreated and Baf treated HT groups compared to control (185.60 ± 17.96%; 255.40 ± 28.71%). Pre-treatment with Rapamycin, followed by HCQ and TMZ decreased basal p62 expression to control levels (125.20 ± 13.56%), with significantly enhanced accumulation observed in Baf treated group (218.70 ± 60%).

3.6 Induction of cell death through coordinate autophagy modulation

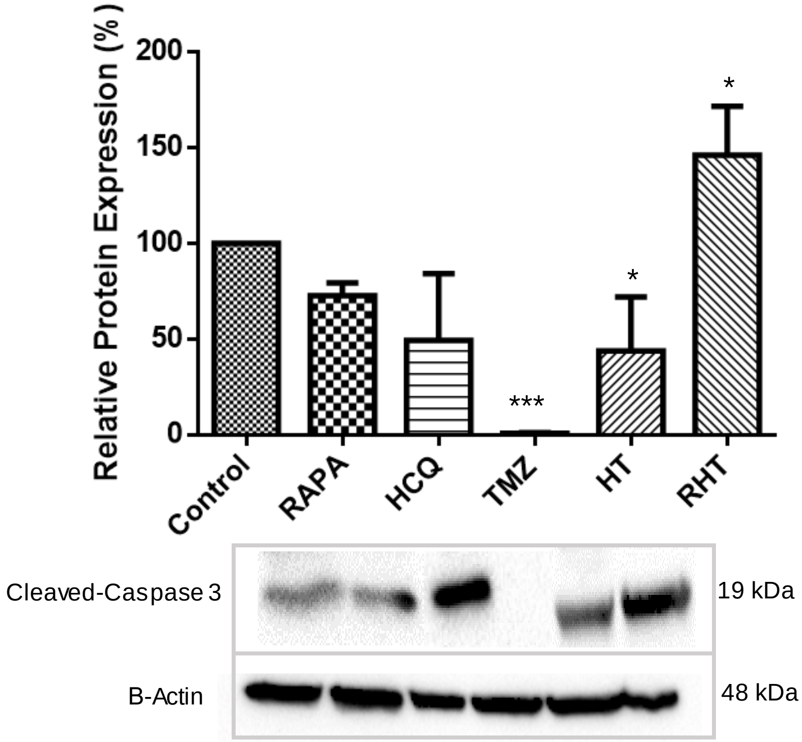

Figure 3.8. Representative Immunoblot of relative cleaved caspase-3 expression levels for Control, 50 nM Rapamycin (Rapa), 50 µM Hydroxychloroquine (HCQ), 250 µM Temozolomide (TMZ), HCQ (50 µM) + TMZ (250 µM) (HT) and Rapa (50 nM) + HCQ (50 µM) + TMZ (250 µM) (RHT) treatment groups. N=3, * p < 0.05 vs corresponding Baf negative group. N=3. * p < 0.05, *** p,0.001.

Relatively unaltered cleaved caspase-3 expression was observed for Rapamycin (50 nM) (72.70 ± 3.84%) and HCQ (50 µM) (49.35 ± 20.12%) treatment groups. Surprisingly, cleaved caspase-3 expression was diminished following 24 hours incubation with TMZ (250 µM) (0.90 ± 0.20%, p<0.001). HCQ pre-treatment (50 µM, 6hours) followed by TMZ (250 µM, 24 hours) decreased expression (43.90 ± 16.27%). However, inducing autophagy with Rapamycin (50 nM) 6 hours prior to incubation with HCQ (50 µM, 6 hours) and TMZ (250 µM, 24 hours) resulted in significantly increased cleaved caspase-3 protein levels (146.00 ± 14.78%, p<0.05), suggesting that apoptosis induction was only occurring in the RHT treatment group.

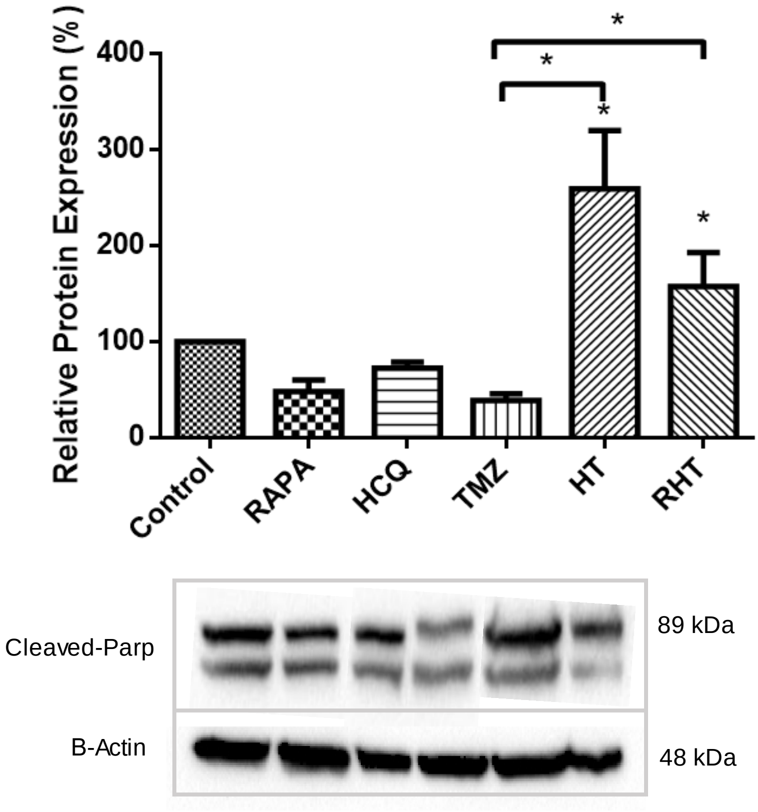

Figure 3.9. Representative Immunoblot of relative cleaved-PARP expression levels for Control, 50 nM Rapamycin (Rapa), 50 µM Hydroxychloroquine (HCQ), 250 µM Temozolomide (TMZ), HCQ (50 µM) + TMZ (250 µM) (HT) and Rapa (50 nM) + HCQ (50 µM) + TMZ (250 µM) (RHT) treatment groups. N=3. .* $p < 0.05$

Cleaved-PARP protein levels were unaltered when upregulating autophagy with Rapamycin (50 nM) (48.19 ± 6.95%) as well as after inhibition of autophagy with HCQ (50 µM) (143.4 ± 1.095%). 24 hours incubation with TMZ (250 µM) (38.88 ± 3.94%) also did not alter cleaved-PARP expression. However, co-incubation of HCQ (50 µM) with TMZ (250 µM) for 6hours significantly enhanced cleaved-PARP expression (259.1 ± 34.99%). Pre-treatment with Rapamycin (50 nM) for 6hours, followed by HCQ (50 µM) and TMZ (250 µM) treatment for 6 and 24 hours respectively also increased cleaved-PARP protein levels significantly (157.6 ± 20.41%).

3.7. Autophagy modulation and chemotherapy disrupted mitochondrial fission and fusion dynamics

In order to assess the rate of mitochondrial fission and fusion, the decay in signal intensity using a 403 nm laser activated mito-PA-GFP was observed at 488 nm and tracked over time (Karbowski *et al*., 2004). Representative images of photoactivated regions are displayed in Fig. 3.10. - 3.15. for each treatment group. Corresponding look up tables (LUT) are also shown, indicating the amount of signal intensity present at 1, 5 and 10 minutes post activation (Fig. 3.10-3.15). Fluorescence intensity was measured every second for 600 seconds and plotted over time as the percentage of initial signal intensity post activation (Fig. 3.10-1.15 B).

Linear regression through signal decay curves indicated that the fastest signal dissipation rate was displayed by the control (-0.127 ± 0.011) and Rapamycin (-0.136 ± 0.009) groups, indicating functional fission and fusion (Fig. 3.16 and 3.17). This is further supported by Fig. 3.10 and 3.11B, showing that the percentage fluorescence intensity reached below 50% after 300 seconds. However, signal dissipation rate was significantly impaired in the HCQ (-0.085 ± 0.011), TMZ (-0.079 ± 0.011), HT (-0.083 ± 0.011) and RHT (-0.090 ± 0.011) groups with a 50% decrease only observed after the full 600second time lapse suggesting that mitochondrial fission and fusion was impaired (Fig. 3.12-3.15B). Of note, although a large degree of fragmentation was observed in the HCQ (Fig. 3.13) HT (Fig. 3.14) and RHT (Fig. 3.15) groups, the same decay curve was obtained for the intermediately fragmented network of the TMZ group (Fig 3.14 and 3.15).

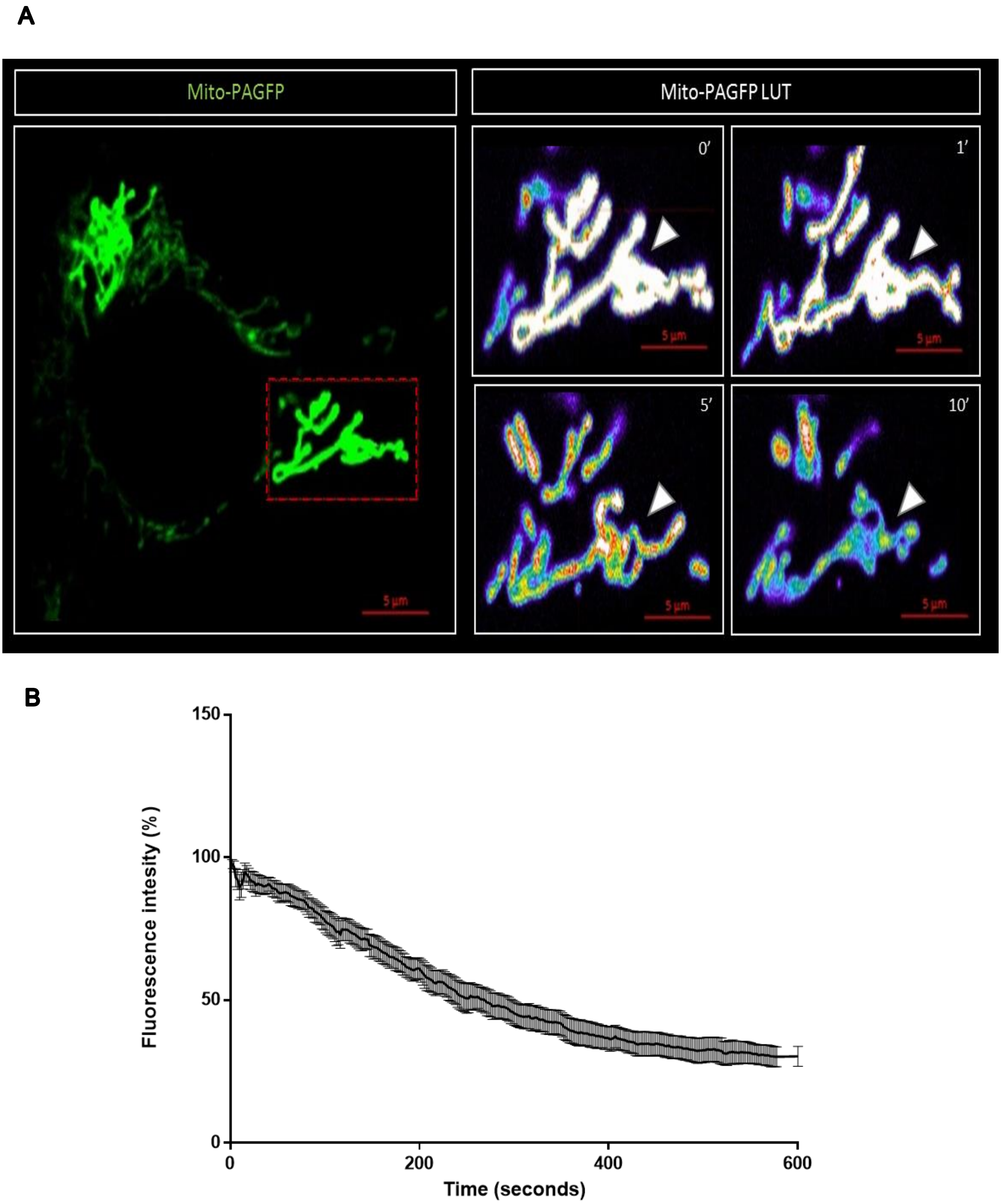

Figure 3.10. Photoactivation assay of control cells. A) Representative image of mito-PA-GFP transfected cells (60X magnification, scalebar 5µM) with the activated region outlined in red enhanced to display LUT intensities at 0, 1, 5 and 10 minute intervals post activation. B) Decrease of mito-PA-GFP signal over time, represented as percentage of the initial signal intensity. N=6.

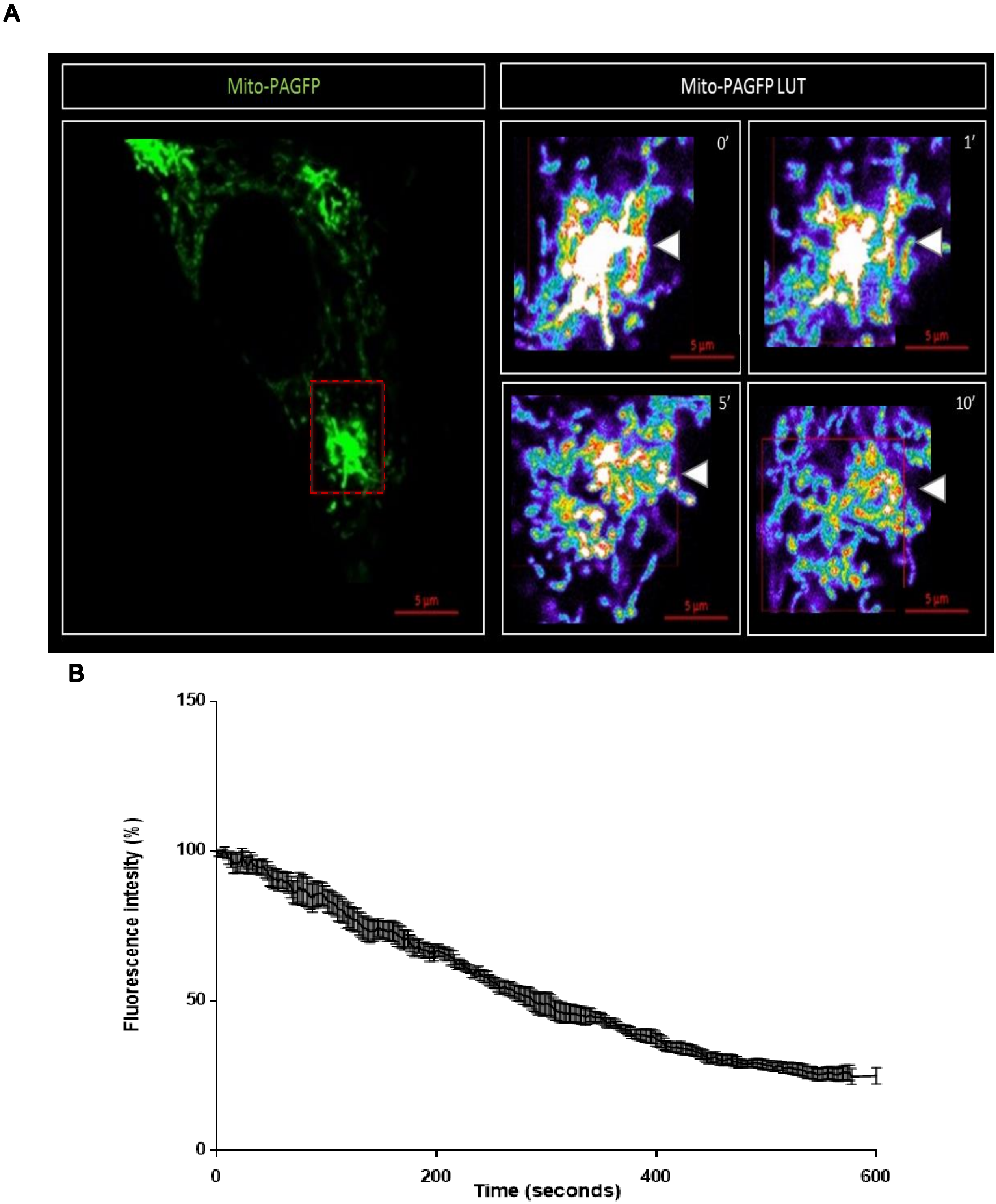

Figure 3.11. Photoactivation assay of cells treated with Rapamycin. A) Representative image of mito-PA-GFP transfected cells (60X magnification, scalebar 5μM) with the activated region outlined in red enhanced to display LUT intensities at 0, 1, 5 and 10 minute intervals post activation. B) Decrease of mito-PA-GFP signal over time, represented as percentage of the initial signal intensity. N=6.

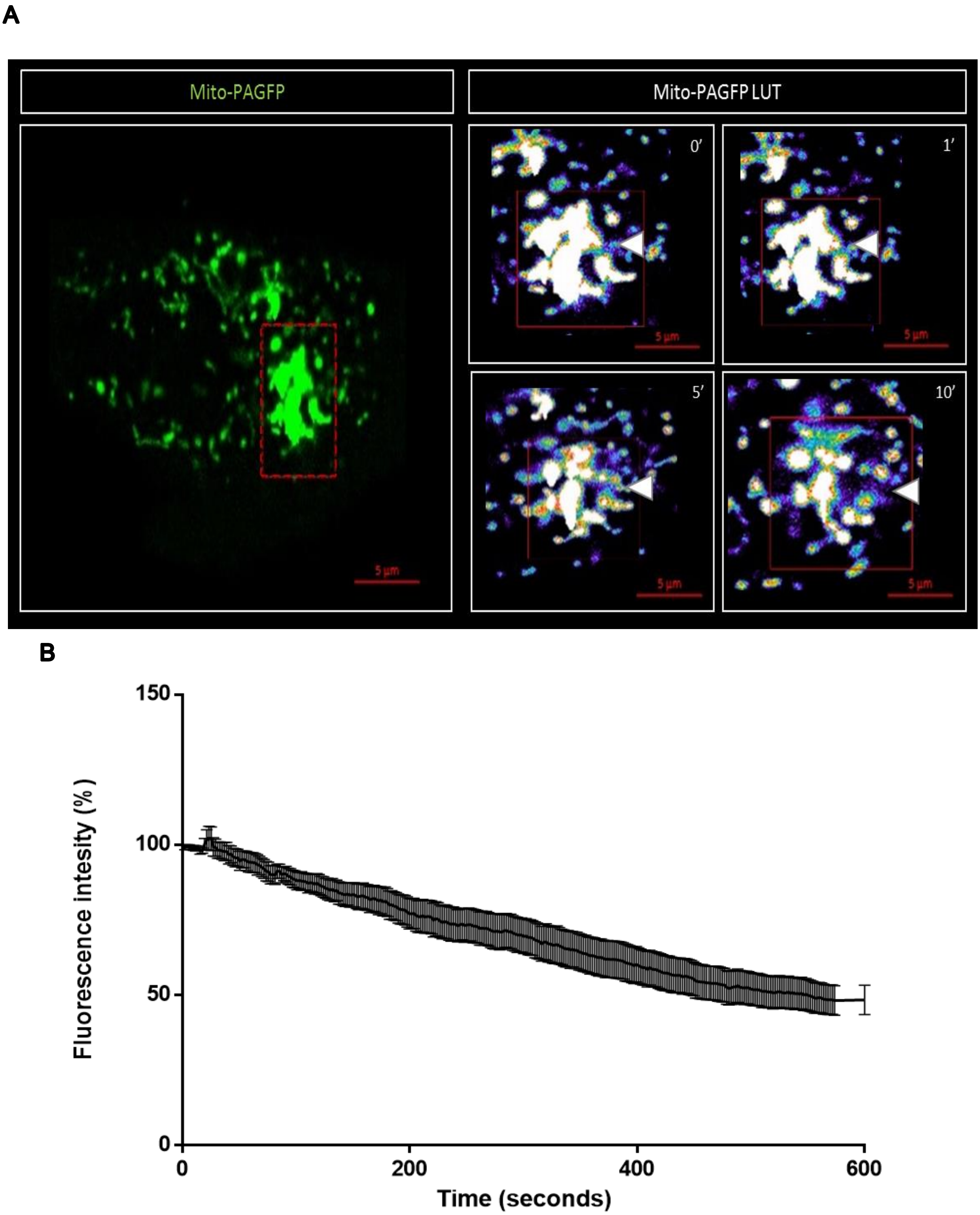

Figure 3.12. Photoactivation assay of HCQ treated cells. A) Representative image of mito-PA-GFP transfected cells (60X magnification, scalebar 5μM) with the activated region outlined in red enhanced to display LUT intensities at 0, 1, 5 and 10 minute intervals post activation. B) Decrease of mito-PA-GFP signal over time, represented as percentage of the initial signal intensity. N=6.

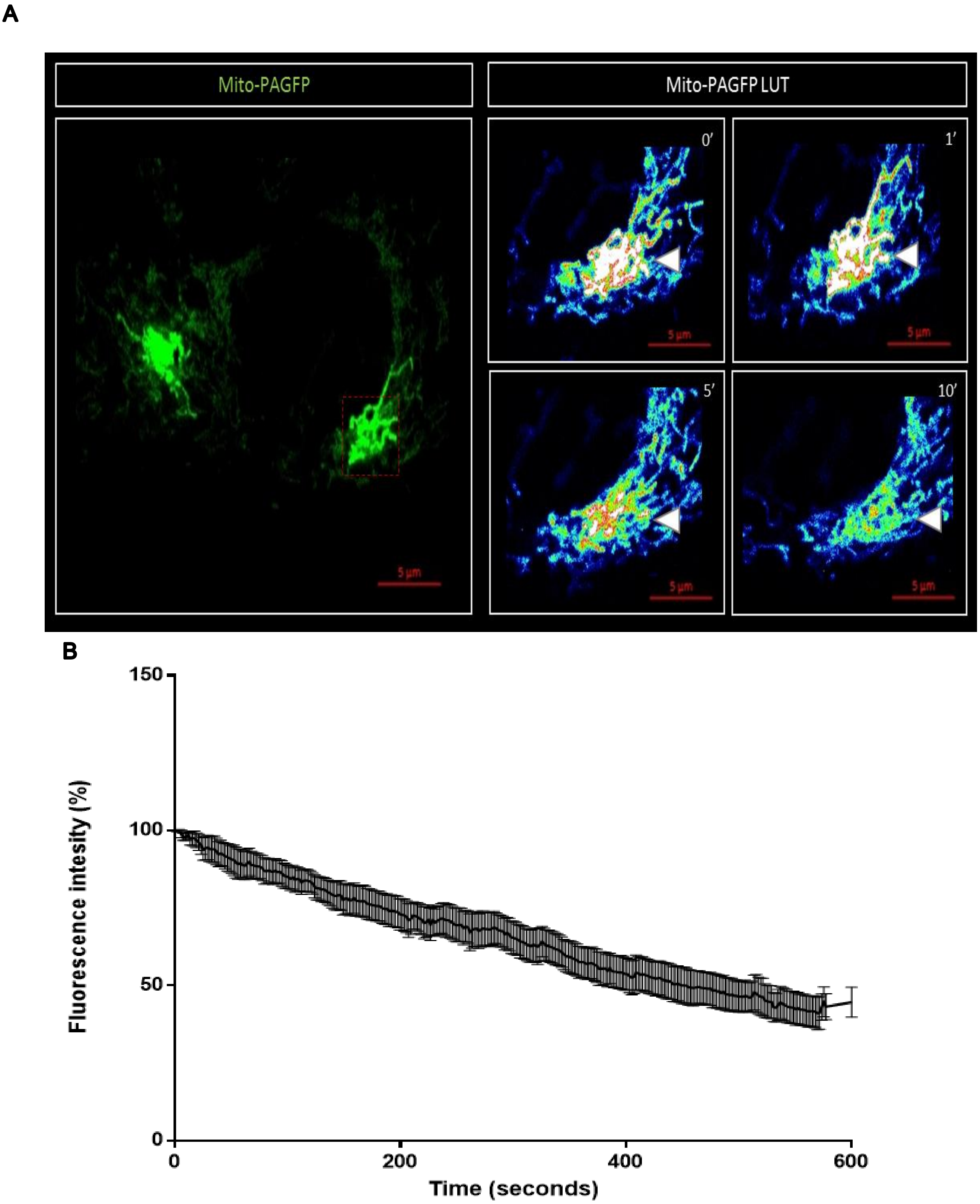

Figure 3.13. Photoactivation assay of TMZ treated cells. A) Representative image of mito-PA-GFP transfected cells (60X magnification, scalebar 5µM) with the activated region outlined in red enhanced to display LUT intensities at 0, 1, 5 and 10 minute intervals post activation. B) Decrease of mito-PA-GFP signal over time, represented as percentage of the initial signal intensity. N=6.

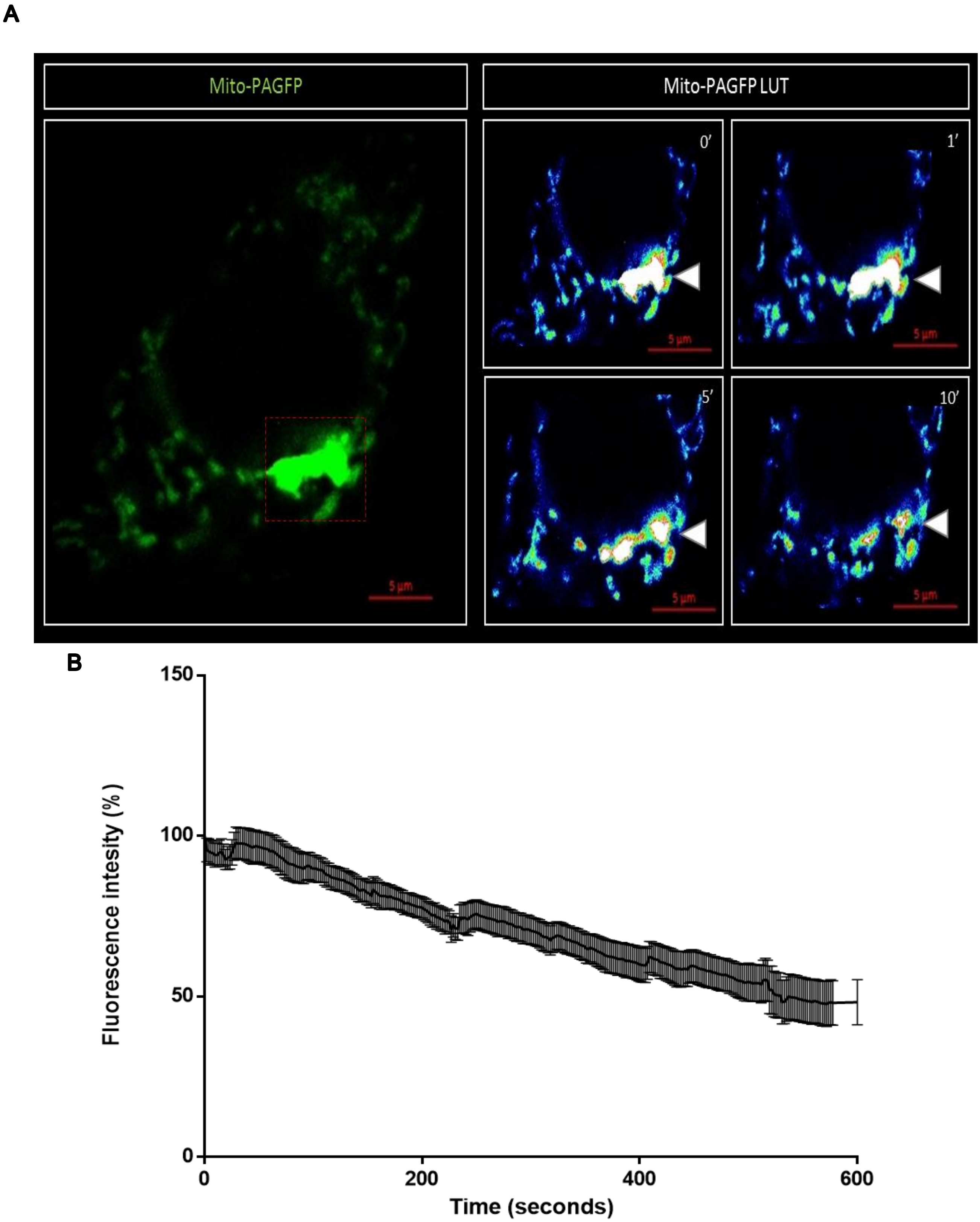

Figure 3.14. Photoactivation assay of cells pretreated with HCQ followed by TMZ. A) Representative image of mito-PA-GFP transfected cells (60X magnification, scalebar 5µM) with the activated region outlined in red enhanced to display LUT intensities at 0, 1, 5 and 10 minute intervals post activation. B) Decrease of mito-PA-GFP signal over time, represented as percentage of the initial signal intensity. N=6.

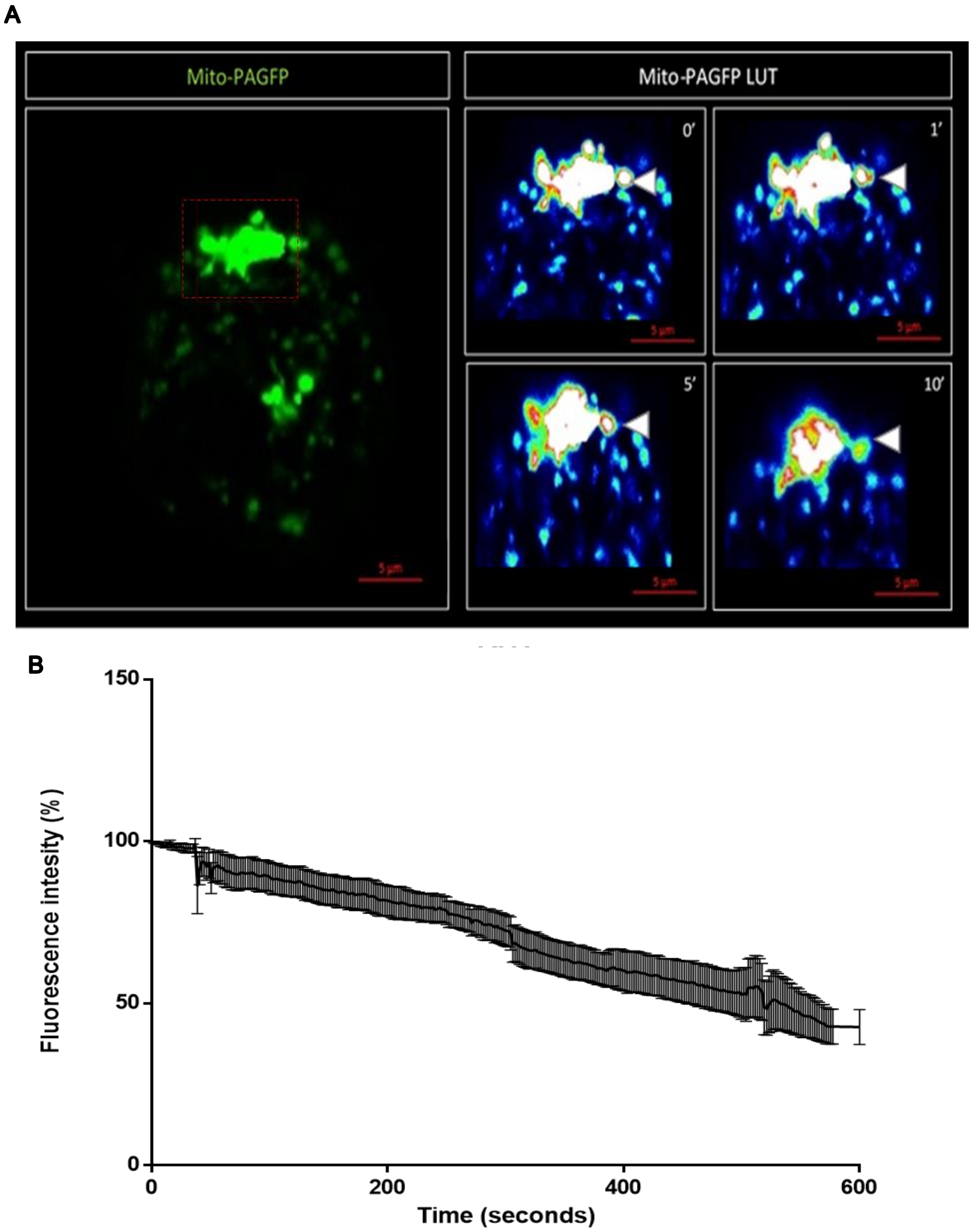

Figure 3.15. Photoactivation assay of cells pretreated with Rapamycin followed by co-incubation of HCQ with TMZ for 6hours followed by 18hours of TMZ treatment. A) Representative image of mito-PA-GFP transfected cells (60X magnification, scalebar 5µM) with the activated region outlined in red enhanced to display LUT intensities at 0, 1, 5 and 10 minute intervals post activation. B) Decrease of mito-PA-GFP signal over time, represented as percentage of the initial signal intensity. N=6.

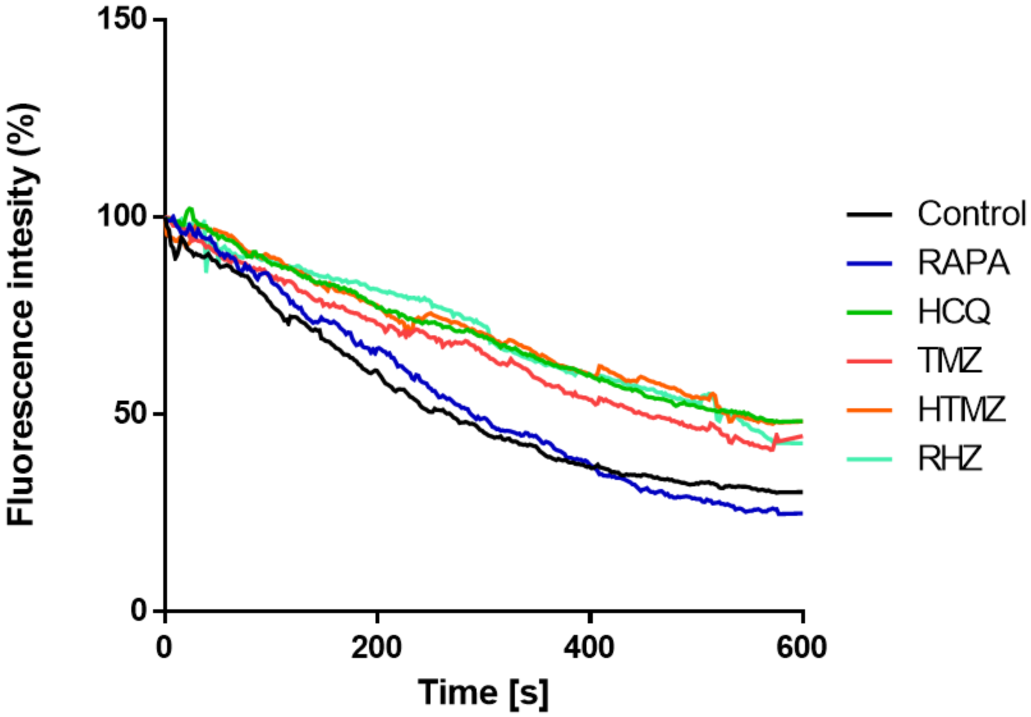

Figure 3.16. Line graph of all treatment groups. N=6

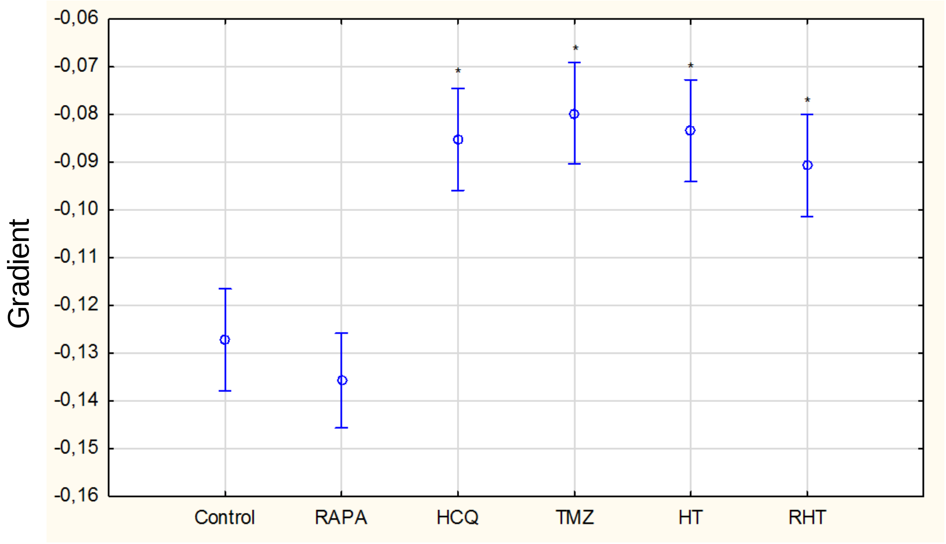

Figure 3.17. Slope comparison of linear regressions through signal decay curves. N=6 *p <0.05 vs control.

3.8 The effect of autophagy modulation on mitochondrial morphometrics

Power laws are functional relationships between two quantities, where a relative change in one quantity is related to a relative proportional change the power of the other. Importantly, in a power law, this occurs independently of the original size of these quantities. Power laws therefore express scale invariance. Therefore, in order to quantify the morphological changes within mitochondrial networks, the power law relationship between the outer perimeter and inner area of each network cluster was assessed. This was achieved by plotting the logarithm of these two measurements against one another and fitting a linear curve through each scatter plot. A linear curve would therefore indicate that a power law relationship between these measurements exists. Given the equation $y = a\,x^{k}$, taking the logarithm on both sides yields:

$$\log\, y = \boldsymbol{k} \log\, x + \log\, a$$

Substituting $X = \log\, x$ and $Y = \log\, y$, as would be presented by a log-log graph, yields the equation for a straight line

$$Y = kX + c$$

Therefore, subsequent comparison of the mean linear gradients between the mitochondrial networks of each treatment group would indicate the amount of scale invariance attributed to each network.

With regards to the pure network properties of the mitochondrial networks, a highly connected network would theoretically contain few clusters with a large amount of overlapping vertices, whereas fragmented networks would have many different clusters, but less overlapping vertices. This, however, only holds true if each mitochondrial network consisted of the same amount of membrane structures or, in this case, “vertices”. In addition, intermediately connected networks also exist, consisting of both a high cluster and vertex count. Therefore, in order to effectively determine the connectivity of these networks, the ratio of the total number of vertices to the number of connected clusters for a given graph was assessed, providing a “connectivity index” as shown in Fig. 3.25.

The mitochondrial networks of U-118MG cells under control conditions yielded an average of 93.20 (± 28.13) clusters, which were found to be highly connected with a connectivity index (CI) of 76.68 (± 4.53) (Fig. 3.18 A, B). Less individual clusters were found for the Rapamycin treatment group (31.67 ± 8.883) (Fig. 3.19 A and B), although the overall connectivity was unaltered (CI 59.71 ± 5.49) (Fig. 3.25). HCQ treatment resulted in a significant increase in fragmentation, with an average of 185.20 (± 19.65) unconnected clusters (11.70 ± 2.33 CI vs Control, $p < 0.05$) (Fig. 3.20 B and 3.25). Significantly more clusters were also observed in cells treated with TMZ (226.4 ± 48.63 vs Control, $p< 0.05$), which were considerably less connected than the control (28.90 ± 4.35 CI). HCQ pre-treatment followed by incubation with TMZ lead to a decreased cluster count (99.67 ± 15.25), with networks being significantly more connected than the TMZ treatment group (45.65 ± 6.15 vs TMZ, $p < 0.05$), but less than the control (45.65 ± 6.15 vs Control $p < 0.05$). Rapamycin pre-treatment followed by HT decreased the number of mitochondrial network clusters significantly to 18.33 (± 3.00), although they displayed the same intermediate degree of connectivity as that of the HT group (42.68 ± 5.56 vs Control and TMZ, $p < 0.05$).

Comparing the degree of scale invariance, a power law relationship was present for all treatment groups in terms of their area and perimeter measurements (Fig. 3.24. A and B). Importantly, the RHT group yielded a larger power law relationship of 0.95 (± 0.0061), suggesting that a more equal distribution of large and connected clusters was present (Fig. 3.19 A and B). Of note, the gradients of the HCQ (0.78 ± 0.018) and TMZ (0.80 ± 0.005) networks presented with the lowest gradients (Fig. 3.24 A and B), indicative of smaller area and perimeter values due to the large amount of fragmentation.

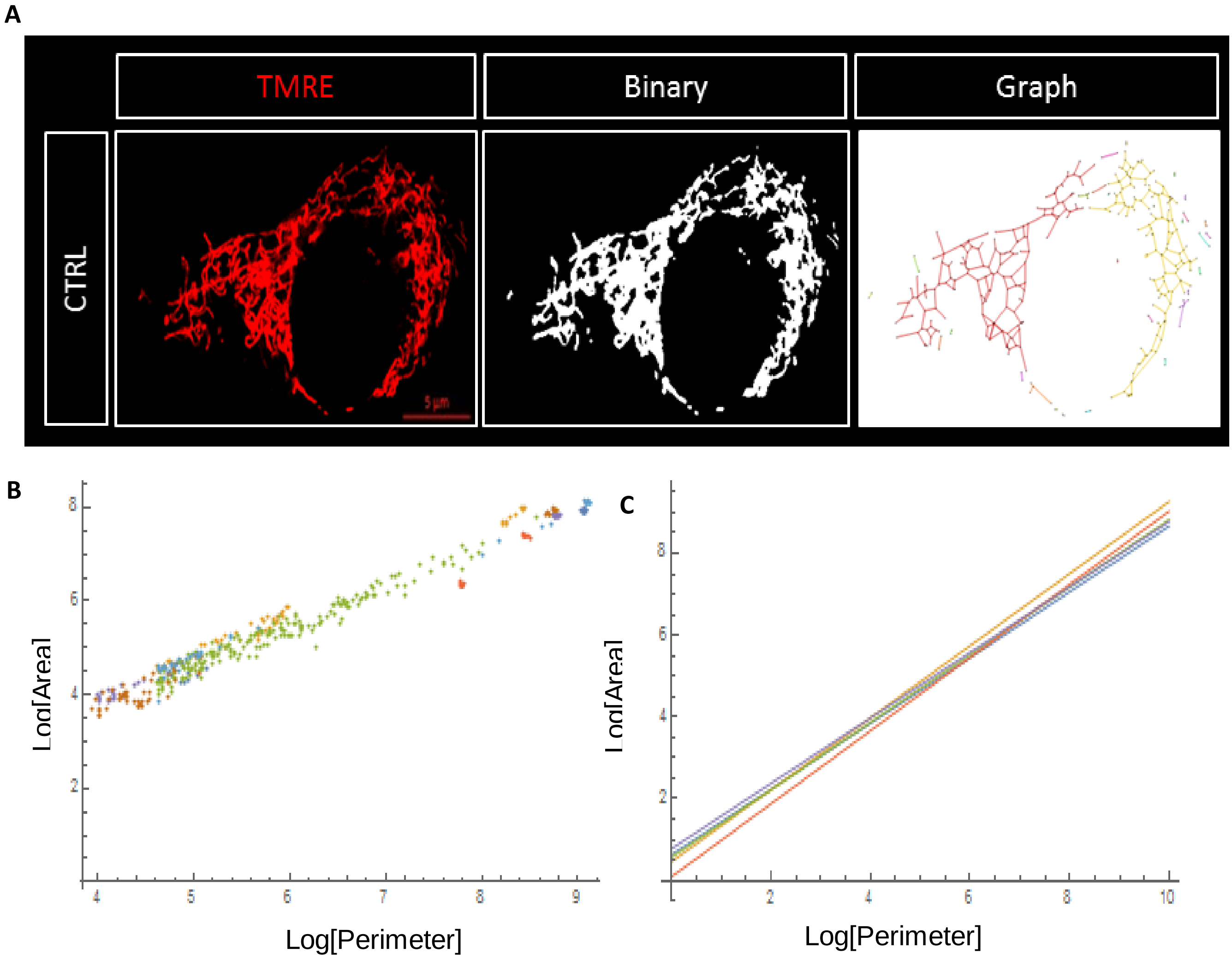

Figure 3.18. Morphometric analyses of Control U-118MG mitochondrial networks. A) Maximal intensity projections of glioma cells stained with TMRE (red) at 60X magnification (scale bar 5μM) B) Scatter plots of individual log[area] and log[perimeter] values for each identified cluster. C) Power Law curve fitting to scatterplots in B. N=6.

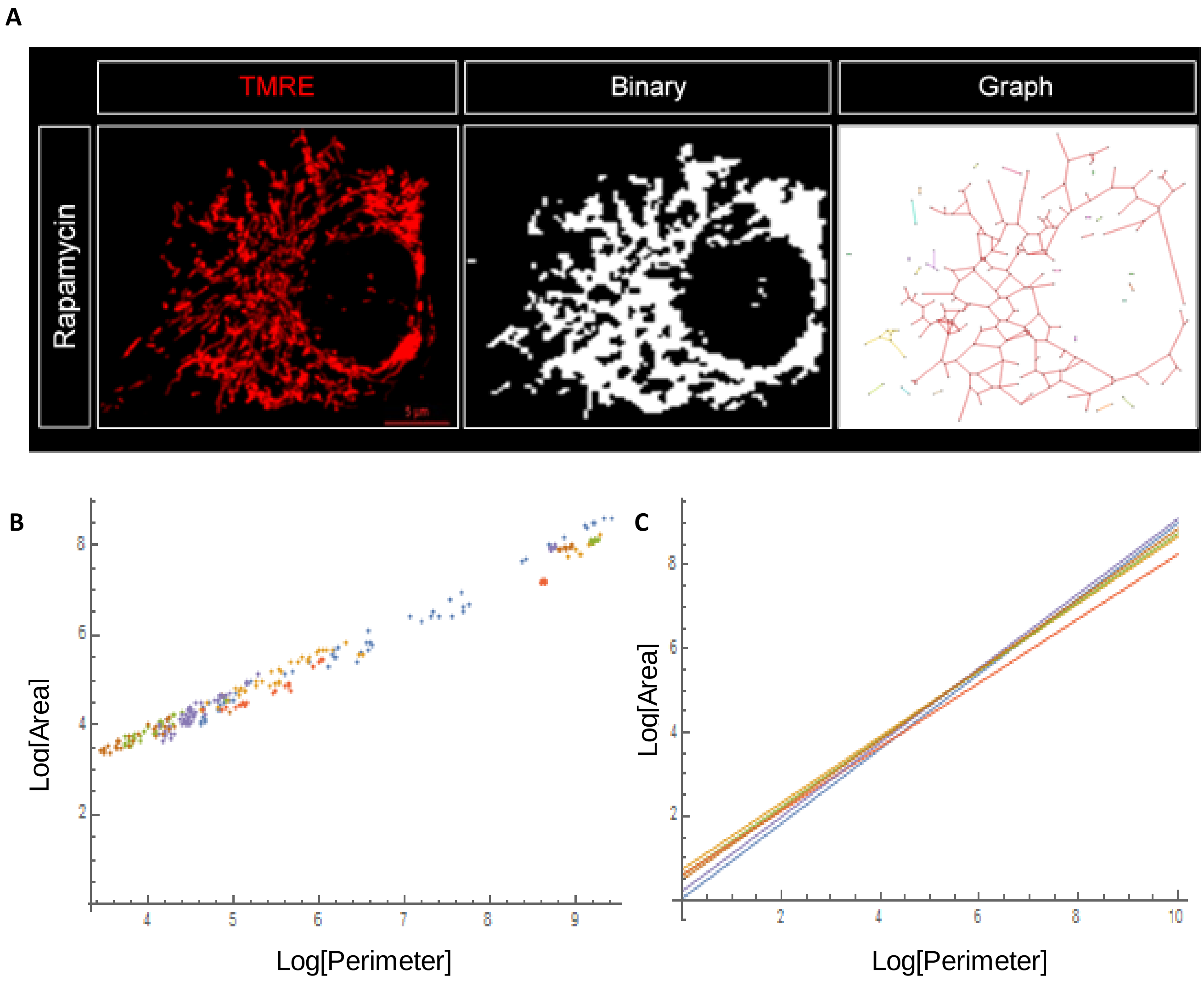

Figure 3.19. Morphometric analyses of Rapamycin treated U-118MG mitochondrial networks. A) Maximal intensity projections of glioma cells stained with TMRE (red) at 60X magnification (scale bar 5μM) B) Scatter plots of individual log[area] and log[perimeter] values for each identified cluster. C) Power Law curve fitting to scatterplots in B. N=6.

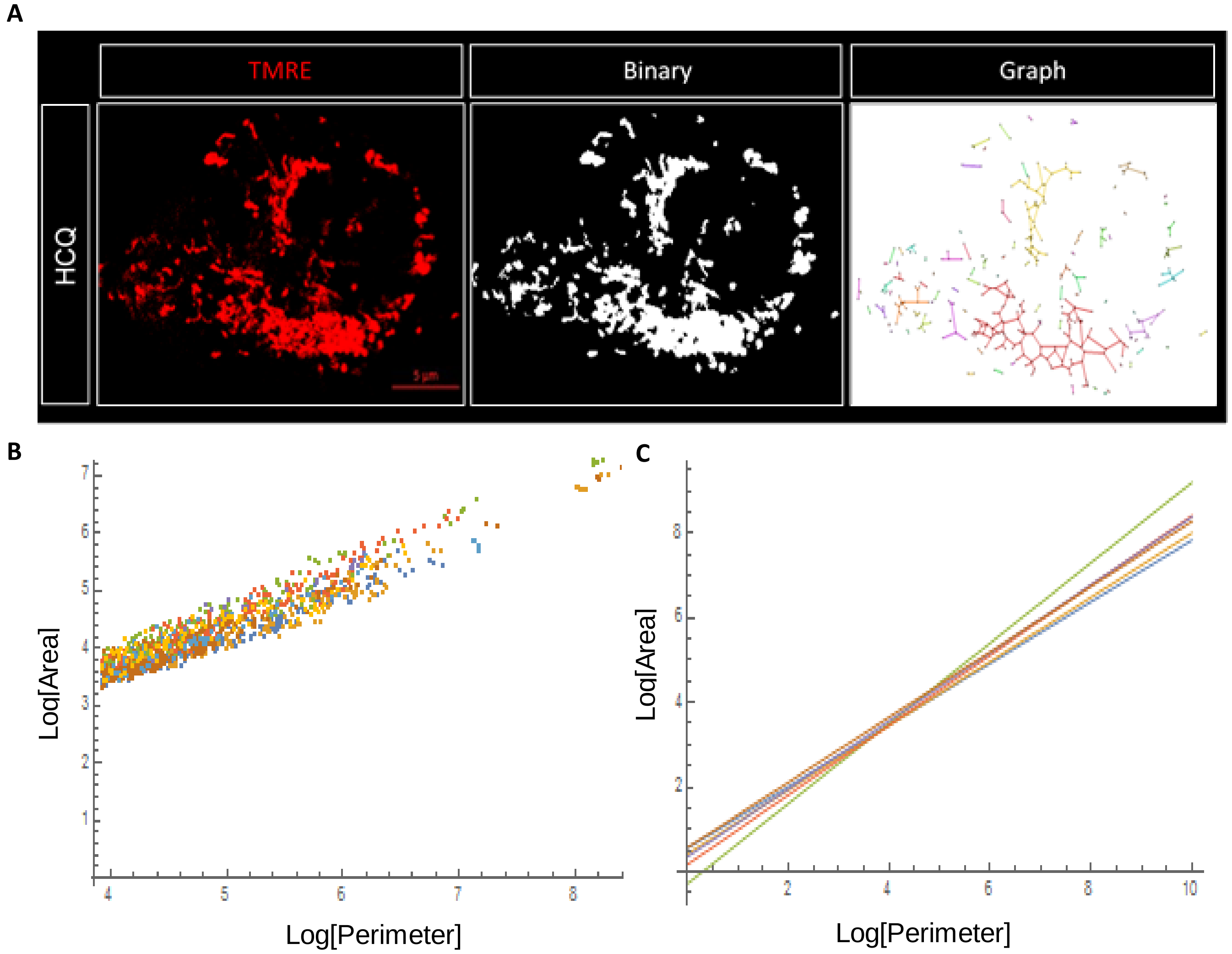

Figure 3.20. Morphometric analyses of HCQ treated U-118MG mitochondrial networks. A) Maximal intensity projections of glioma cells stained with TMRE (red) at 60X magnification (scale bar 5µM) B) Scatter plots of individual log[area] and log[perimeter] values for each identified cluster. C) Power Law curve fitting to scatterplots in B. N=6.

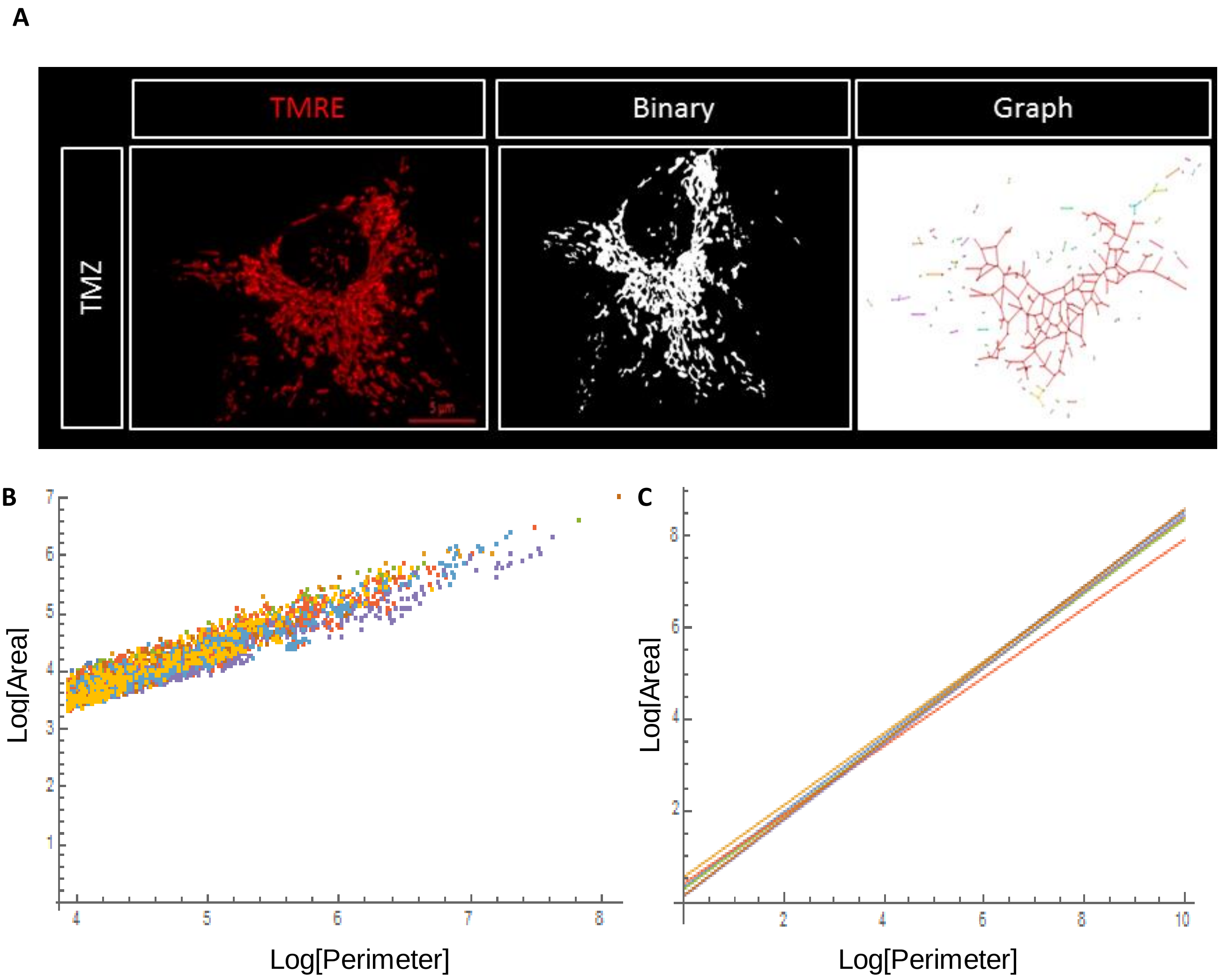

Figure 3.21. Morphometric analyses of TMZ treated U-118MG mitochondrial networks. A) Maximal intensity projections of glioma cells stained with TMRE (red) at 60X magnification (scale bar 5µM) B) Scatter plots of individual log[area] and log[perimeter] values for each identified cluster. C) Power Law curve fitting to scatterplots in B. N=6.

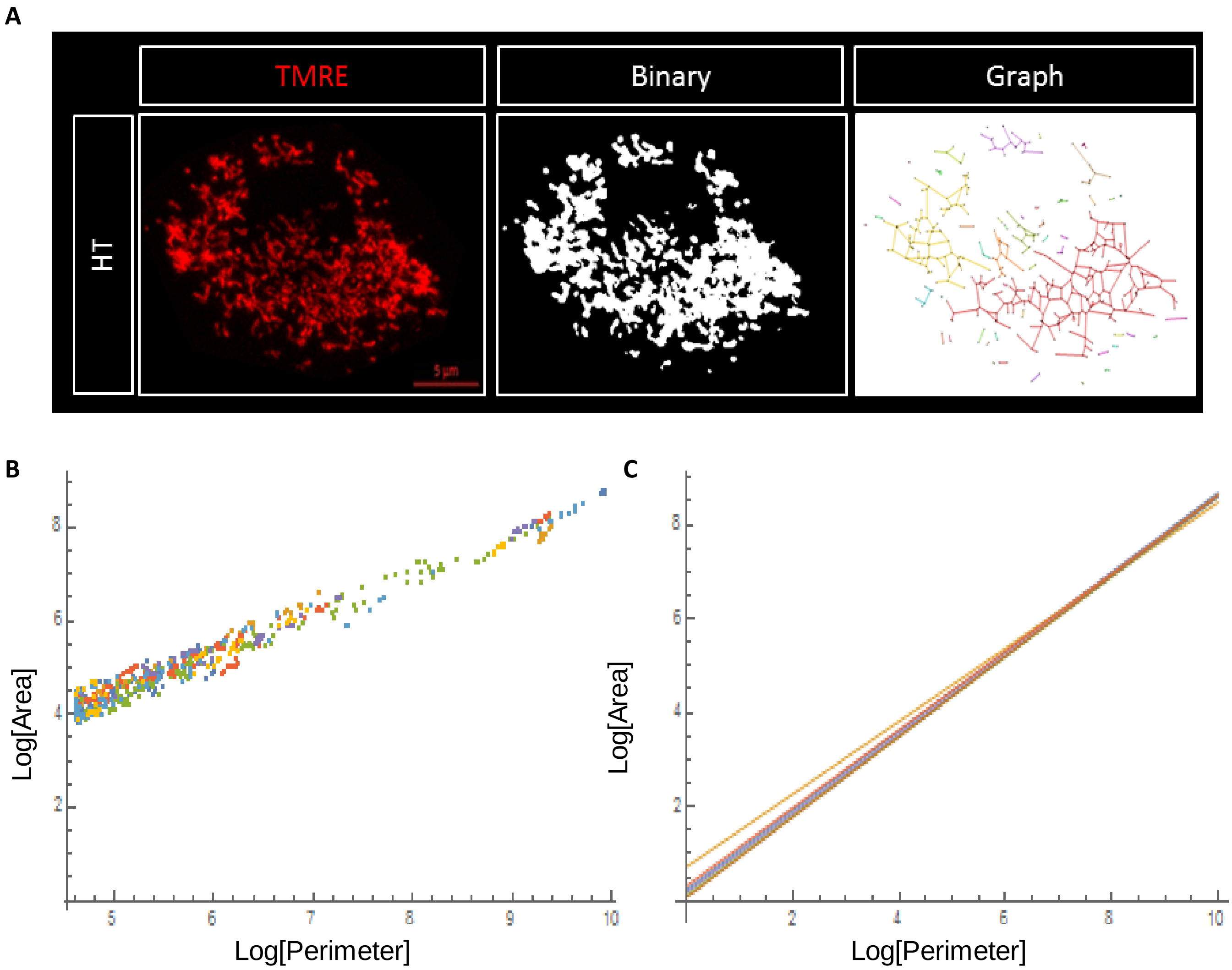

Figure 3.22. Morphometric analyses of U-118MG mitochondrial networks treated with HCQ and TMZ (HT). A) Maximal intensity projections of glioma cells stained with TMRE (red) at 60X magnification (scale bar 5μM) B) Scatter plots of individual log[area} and log[perimeter] values for each identified cluster. C) Power Law curve fitting to scatterplots in B. N=6.

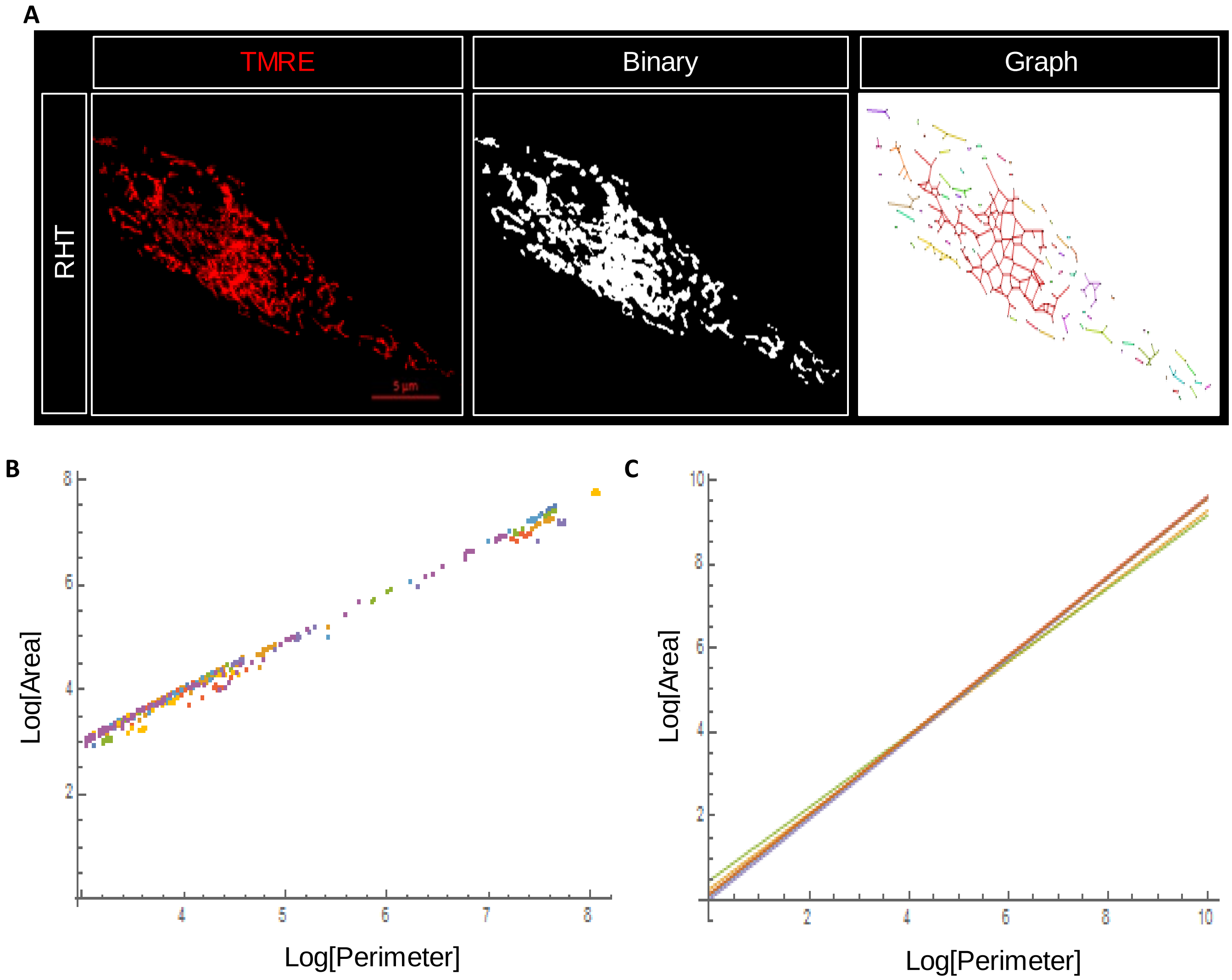

Figure 3.23. Morphometric analyses of U-118MG cells treated with Rapamycin, HCQ and TMZ (RHT). A) Maximal intensity projections of glioma cells stained with TMRE (red) at 60X magnification (scale bar 5μM) B) Scatter plots of individual log[area] and log[perimeter] values for each identified cluster. C) Power Law curve fitting to scatterplots in B. N=6.

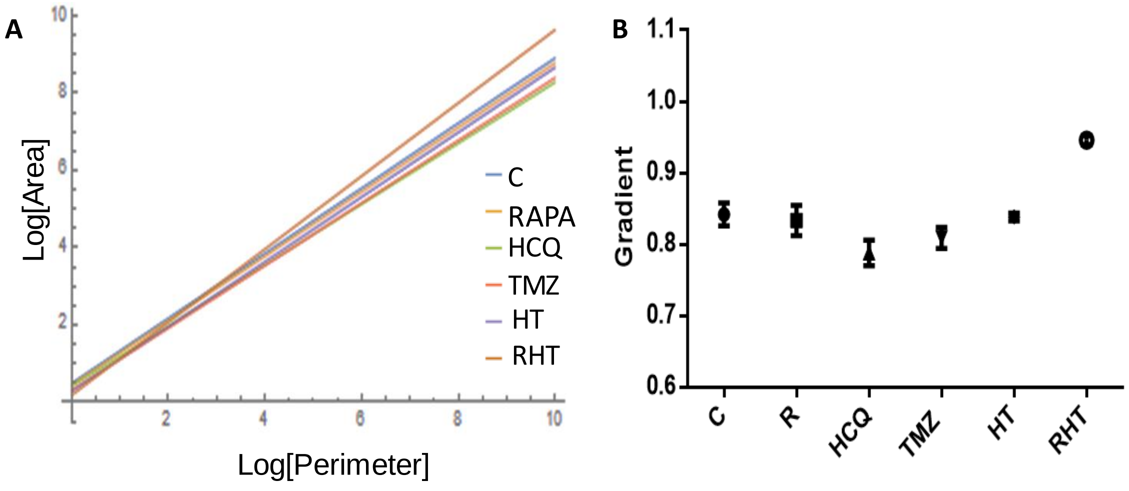

Figure 3.24. Power law comparison displayed as A) Line graphs and B) their respective mean gradients for Control (C), Rapamycin (R), Hydroxychloroquine (HCQ), Temozolomide (TMZ), HCQ and TMZ in combination (HT) and Rapamycin, HCQ and TMZ in combination (RHT) treatment groups. N=6.

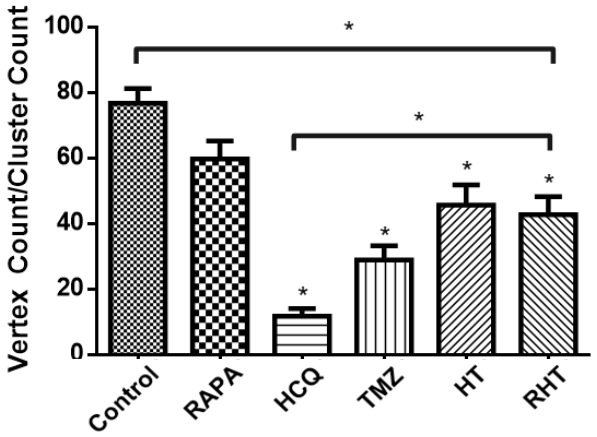

Figure 3.25. Connectivity Index (Vertex Count/Cluster Count, CI) values for Control (C), Rapamycin (R), Hydroxychloroquine (HCQ), Temozolomide (TMZ), HCQ and TMZ in combination (HT) and Rapamycin, HCQ and TMZ in combination (RHT) treatment groups. N=6, $*p < 0.05$.

3.9 Assessing the effect of autophagy modulation on mitochondrial morphology regulators

In order to determine the molecular mechanisms responsible for the changes in dynamics and morphology observed in sections 3.5 and 3.6, the expression of key fusion and fission proteins was assessed through Western Blot analyses. These include the fusion proteins MFN1 (Fig.3.22), MFN2 (Fig.3.23) and OPA-1 (Fig. 3.24) as well as the fission protein DRP1.

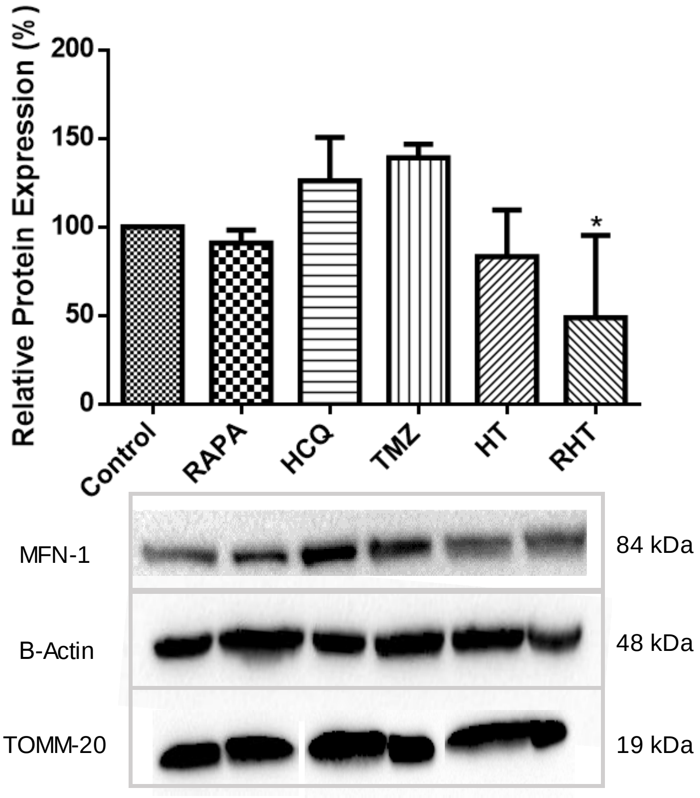

Figure 3.26. Representative Immunoblot of relative Mitofusin 1 (MFN1) protein levels for Control, 50 nM Rapamycin (Rapa), 50 µM Hydroxychloroquine (HCQ), 250 µM Temozolomide (TMZ), HCQ (50uM) + TMZ (250 µM) (HTMZ) and Rapa (50 nM) + HCQ (50 µM) + TMZ (250 µM) (RHT) treatment groups. N=3. * $p < 0.05$.

MFN1 protein levels remained unaltered following 50 nM Rapamycin (90.96 ± 4.231%), 50 µM HCQ (126.2 ± 14.13%) and 250 µM TMZ (139.1 ± 4.406%) treatment (Fig.3.22). Pre-treatment with HCQ (50 µM) for 6 hours (83.30 ± 15.17%) had no effect on MFN1 expression. However, 6hour pre-treatment with Rapamycin (50 nM) followed by HCQ (50 µM) and TMZ (250 µM) treatment decreased MFN1 expression significantly compared to the control (48.70 ± 26.88, $p<0.05$).

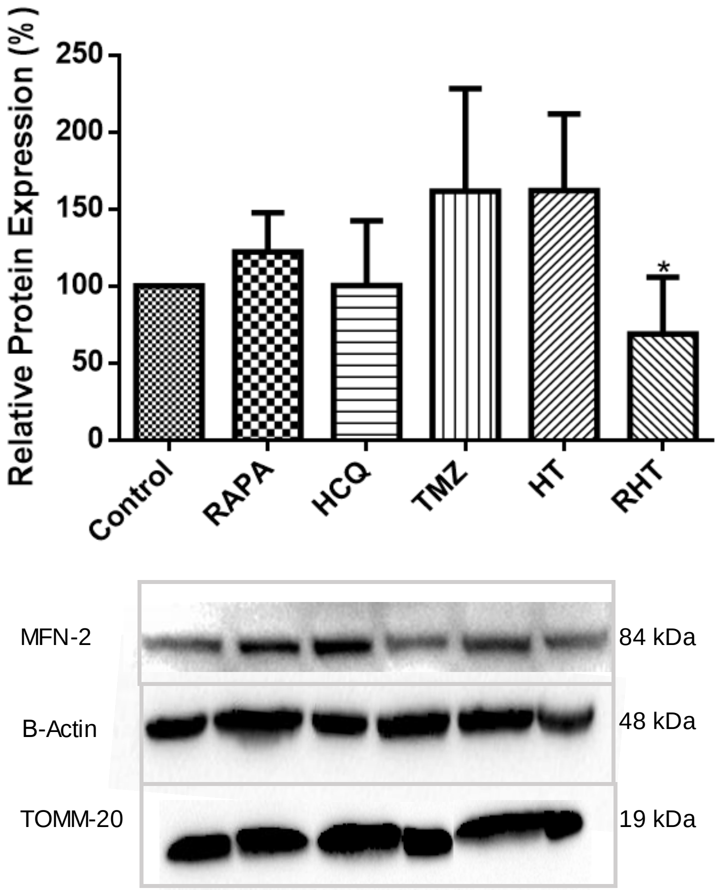

Figure 3.27. Representative Immunoblot of relative Mitofusin 2 (MFN2) protein levels for Control, 50 nM Rapamycin (Rapa), 50 µM Hydroxychloroquine (HCQ), 250uM Temozolomide (TMZ), HCQ (50uM) + TMZ (250uM) (HTMZ) and Rapa (50 nM) + HCQ (50uM) + TMZ (250uM) (RHT) treatment groups N=3. * $p < 0.05$.

MFN2 expression levels followed much the same trend as MFN1, with unaltered signal intensities observed for Rapamycin (122.1 ± 14.67%), HCQ (100.4 ± 24.25%), TMZ (161.5 ± 38.55%) and HT (161.9 ± 28.76%) treatment groups. A moderate, yet significant decrease in MFN2 expression was observed after 6hour pre-treatment with Rapamycin (50 nM) followed by incubation with HCQ (50 µM) and TMZ (250 µM) compared to control cells (68.91 ± 21.20%, $p<0.05$).

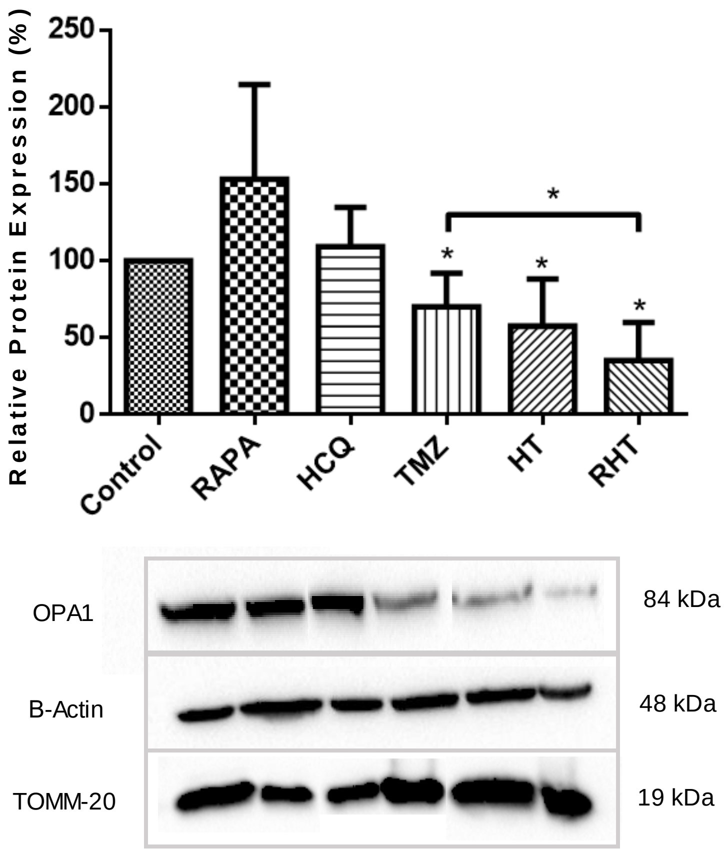

Figure 3.28. Representative Immunoblot of relative optic atrophy 1 (OPA1) protein levels for Control, 50 nM Rapamycin (Rapa), 50 µM Hydroxychloroquine (HCQ), 250 µM Temozolomide (TMZ), HCQ (50 µM) + TMZ (250 µM) (HTMZ) and Rapa (50 nM) + HCQ (50 µM) + TMZ (250 µM) (RHT) treatment groups N=3. * $p < 0.05$.

50 nM of Rapamycin did not alter OPA-1 expression levels (153.1 ± 35.52%), nor did 50 µM HCQ (109.2 ± 14.88%). However, 24 hours of TMZ (250 µM) treatment decreased OPA-1 protein levels significantly compared to Control (70.15 ± 12.60, $p < 0.05$), with the same effect observed for the 6 hour HCQ (50 µM) pre-treatment group (57.57 ± 17.74%, $p<0.05$). Upregulating autophagy for 6 hours with Rapamycin (50 nM) prior to incubation with HCQ (50 µM) and TMZ (250 µM) decreased OPA-1 expression considerably compared to both the control and TMZ groups (35.32 ± 14.16%, $p < 0.05$).

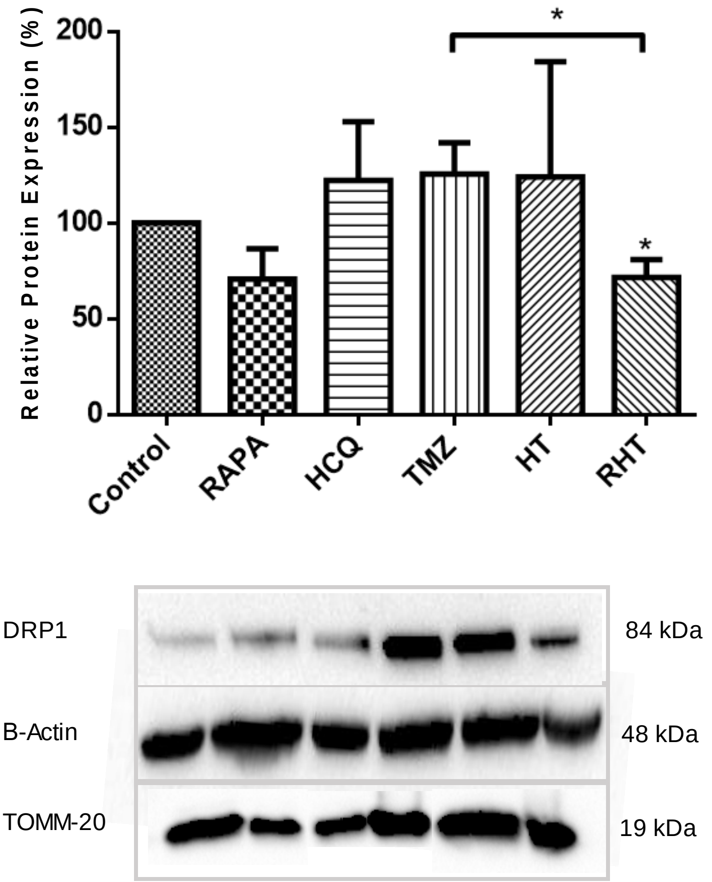

Figure 3.29. Representative Immunoblot of relative Dynamin related protein (DRP1) levels Control, 50nM Rapamycin (Rapa), 50 µM Hydroxychloroquine (HCQ), 250 µM Temozolomide (TMZ), HCQ (50 µM) + TMZ (250 µM) (HTMZ) and Rapa (50 nM) + HCQ (50 µM) + TMZ (250 µM) (RHT) treatment groups. N=3. * $p < 0.05$.

Induction of autophagy for 6hours with Rapamycin (50 µM) did not alter DRP1 protein expression (70.71 ± 9.21%), nor did 6hours of autophagy inhibition with HCQ (50 µM) (122.2 ± 17.77%). The same was observed following 24 hours incubation with TMZ (250 µM) (125.60 ± 9.42%) and 6hours co-incubation with HCQ (50 µM) (124.2 ± 34.73%). However, pre-treatment with Rapamycin (50 nM), followed by co-incubation with HCQ (50 µM) and TMZ (250 µM) decreased DRP1 expression significantly compared to the control (71.64 ± 5.32%, $p<0.05$).

3.10 The contribution of mitochondrial respiratory capacity to GBM resistance and cell death onset.

In order to generate a bioenergetic profile comprising of key metabolic states, a coupling control protocol was applied to permeabilised U-118MG cells and assessed through high resolution respirometry. These include the routine endogenous respiration, the amount of proton leak after addition of the NADH-linked substrates (pyruvate, malate and glutamate) (LEAK state), complex I activity after addition of a non-saturating ADP concentration (OXPHOS_PGM), combined complex I & II activity after addition of succinate (OXPHOS_PGMS) and electron transfer system (ETS) capacity by inducing maximal O_2 flux at optimal protonophore concentrations. All values were corrected for residual oxygen consumption (ROX) so as to limit the effect of any oxidative side reactions which might result from the addition of TCA substrates or ETS inhibitors. These final results were also normalised to the total amount of mitochondria, which is determined by addition of TMPD to yield a maximal complex IV response. Displayed in Figures 3.26 - 3.31 are representative traces of cell respirometry (Fig. 3.26 - 3.31 A), the corresponding O_2 flux values corrected for residual oxygen consumption (ROX) and normalised to TMPD (Fig. 3.26 - 3.31 B) and their flux control ratios (FCR) (Fig. 3.26 - 3.31 C).

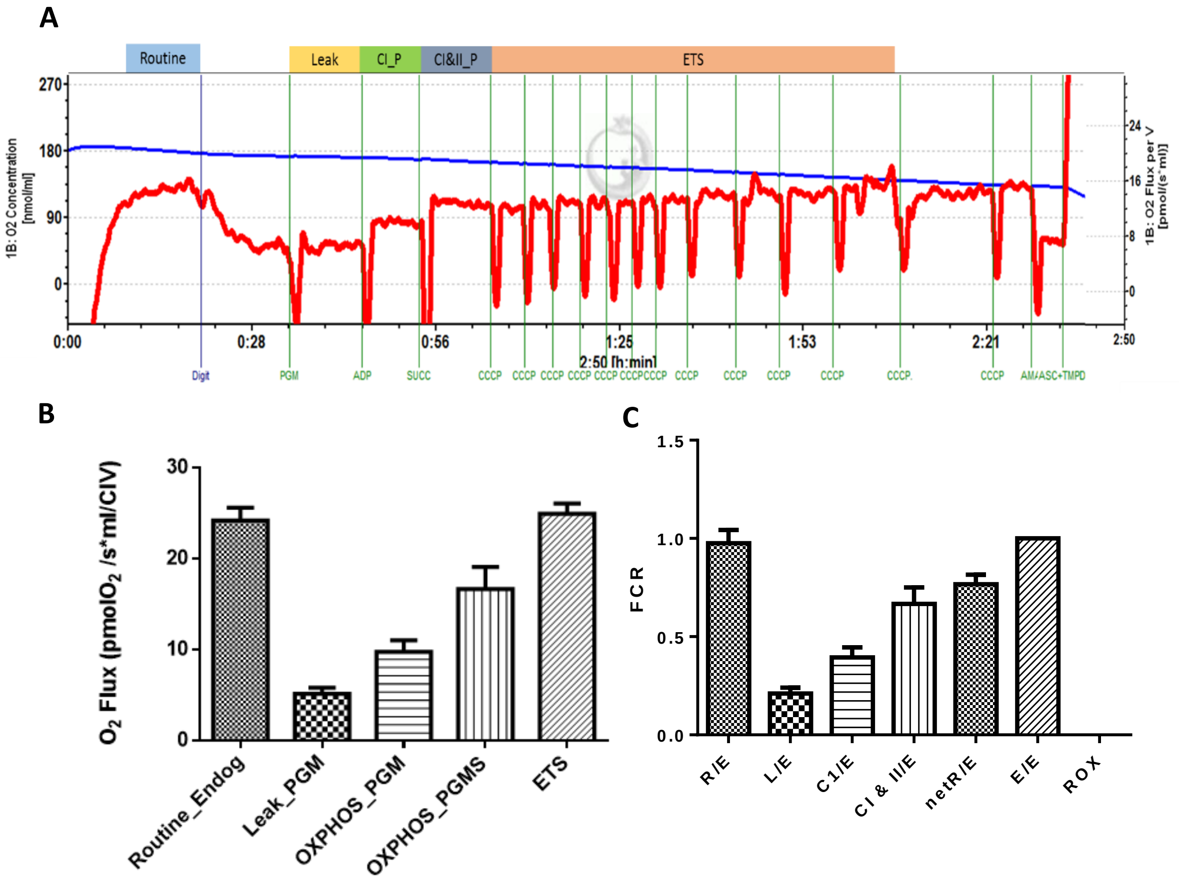

Figure 3.30. High Resolution respirometry of control U-118MG cells. A) Representative trace of intact cell respirometry shown as O_2 flux (J_{O2}) per volume of cell suspesion (pmol/(s*ml)) (500 000 cells/ml). B) O_2 Flux values corrected for residual oxygen consumption (ROX) and normaliised to TMPD for the following metabolic states; Routine respiration (R) , Leak state (L), OXPHOS through complex I (OXPHOS_PGM), OXPHOS through Complex I&II (OXPHOS_PGM) and Electron Transfer System capacity (ETS). C) Flux control ratios representing each metabolic state ratioed to ETS capacity. N=3.

The ratio of each respiratory state to its corresponding ETS capacity is represented as a flux control ratio, indicating how close these states operate to the total respiratory efficiency of the ETS. For glioma cells under control conditions, endogenous routine respiration was observed to operate close to their maximal ETS capacity at 25.75 pmolO_2/s*ml/CIV (±1.171), yielding a R/E ratio of 0.98 (± 0.07) (Fig. 3.12 C). A small amount of proton leak was observed (4.84 pmolO_2/s*ml/CIV ± 0.8574) with an L/E ratio of 0.21 (± 0.03). The netR/E flux control ratio ((R-L)/E) is a useful index to estimate the amount of ETS capacity utilised to drive phosphorylation-related respiration (i.e. ATP synthesis). A netR/E ratio of 0.78 (± 0.05) was observed, suggesting that 78% of maximal ETS capacity is utilised for ATP production. OXPHOS through Complex I was observed at 10.71 pmolO_2/s*ml/CIV (± 1.248), and 14.54 pmolO_2/s*ml/CIV (±1.580) in combination with Complex II.

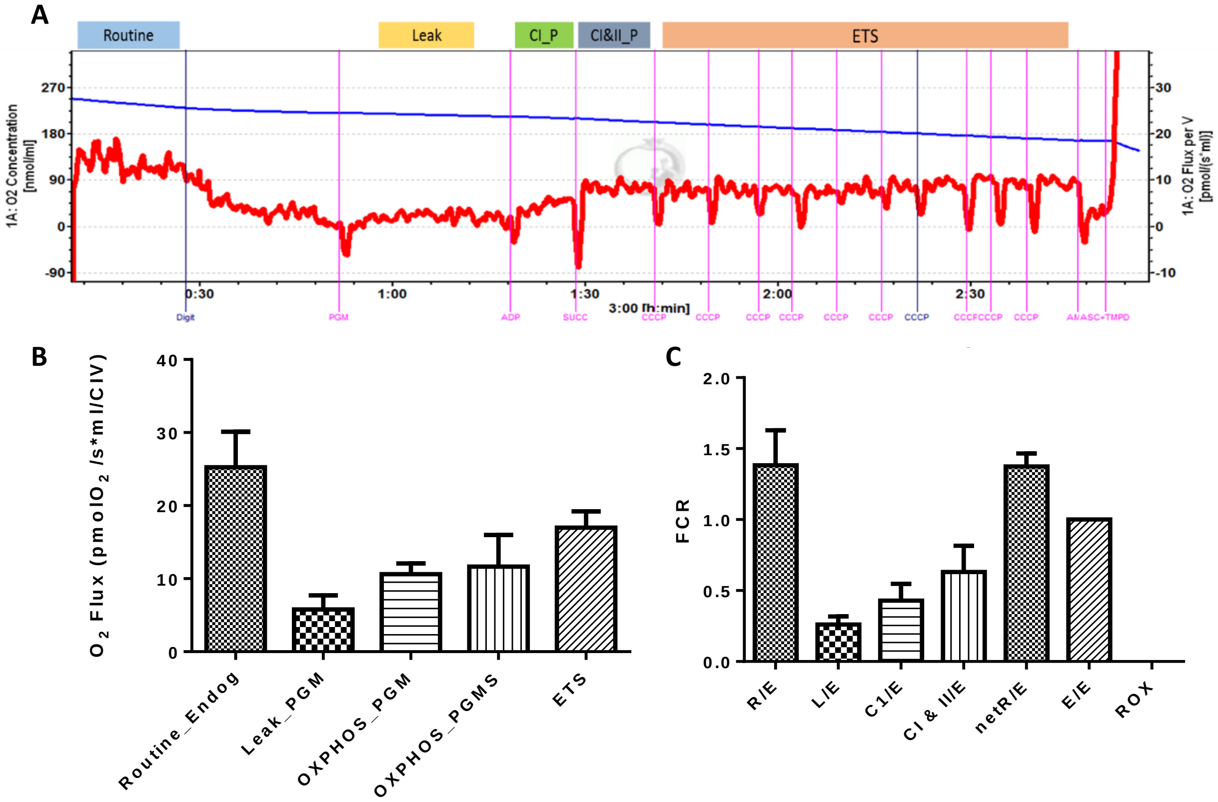

Figure 3.31. High Resolution respirometry of Rapamycin treated U-118MG cells. A) Representative trace of intact cell respirometry shown as O_2 flux (J_{O2}) per volume of cell suspesion (pmol/(s*ml)) (500 000 cells/ml) B) O_2 Flux values corrected for residual oxygen consumption (ROX) for the following metabolic states; Routine respiration (R) , Leak state (L), Complex I activity (C1), Complex I&II activity (C2), Electron Transfer System capacity (ETS). C) Flux control ratios representing each metabolic state ratioed to ETS capacity. N=3.

Rapamycin treatment did not drastically alter Routine oxygen consumption flux (21.35 ± 4.07 pmolO_2/s*ml/CIV) (Fig. 3.13. B). However, a maximum ETS response above that of the routine could not be reached (16.98 ± 2.23 pmolO_2/s*ml/CIV) yielding a mean R/E ratio beyond maximum ETS capacity of 1.38 (± 0.25) (Fig. 3.13 C). Given that Leak levels also remained unchanged (4.34 ± 1.99 pmolO_2/s*ml/CIV), an L/E ratio of 0.26 (± 0.06) was maintained. The netR/E value of 1.37 (± 0.093) indicates a 37% increase in phosphorylation associated respiration. This is clearly observed in the representative trace (Fig 3.13 A), where a maximal flux value above that of the routine could not be reached after uncoupling CCCP titrations. OXPHOS through Complex I (10.61 ± 1.47 pmolO_2/s*ml/CIV) and CI & II (11.66 ± 4.32 pmol0_2/s*ml/CIV) also remained similar to that of control values.

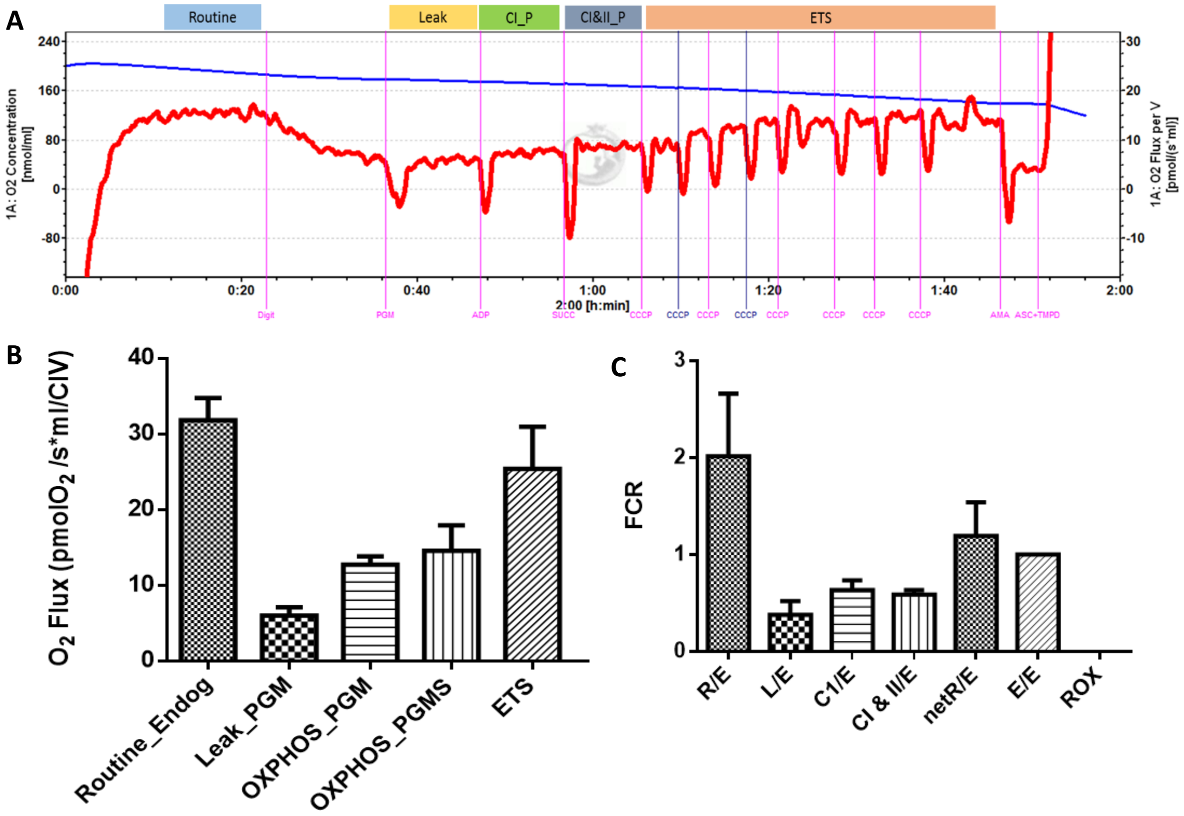

***Figure 3.32**.* High Resolution respirometry of HCQ treated U-118MG cells. A) Representative trace of intact cell respirometry shown as O_2 flux (J_{O2}) per volume of cell suspesion (pmol/(s*ml)) (500 000 cells/ml) B) O_2 Flux values corrected for residual oxygen consumption (ROX) for the following metabolic states; Routine respiration (R) , Leak state (L), Complex I activity (C1), Complex I&II activity (C2), Electron Transfer System capacity (ETS). C) Flux control ratios representing each metabolic state ratioed to ETS capacity. N=3.

A routine respiration rate of 31.83 pmol02/s*ml/CIV (± 2.908) was observed for the HCQ treatment group, which is well above its ETS capacity of 25.39 pmol02/s*ml/CIV (± 5.562) (Fig3.14 A and B). The Leak state was, however, increased to 6.03 pmol02/s*ml/CIV (± 1.0871), resulting in a L/E value of 0.38 (± 0.14), indicating increased dyscoupling of the ETS. Given the increase in proton leak, the netR/E ratio remained lower than that of the Rapamycin group (1.193 ± 0.35). OXPHOS through CI was found to be 12.75 pmol02/s*ml/CIV (± 1.070) and 14.56 pmol02/s*ml/CIV (± 3.362) in combination with CII.

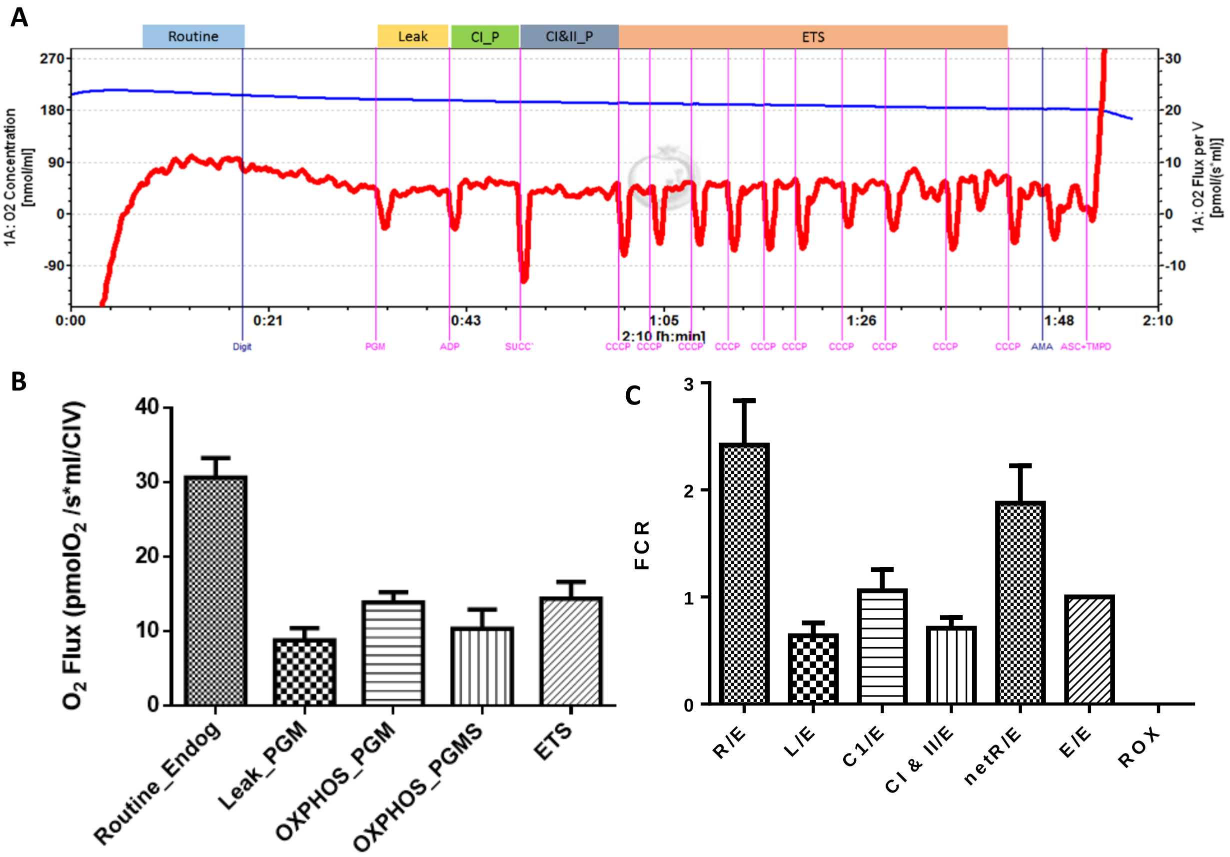

Figure 3.33. High Resolution respirometry of TMZ treated U-118MG cells. A) Representative trace of intact cell respirometry shown as O_2 flux (J_{O2}) per volume of cell suspesion (pmol/(s*ml)) (500 000 cells/ml) B) O_2 Flux values corrected for residual oxygen consumption (ROX) for the following metabolic states; Routine respiration (R) , Leak state (L), Complex I activity (C1), Complex I&II activity (C2), Electron Transfer System capacity (ETS). C) Flux control ratios representing each metabolic state ratioed to ETS capacity. N=3.

TMZ treatment further uncoupled the ETS, yielding a R/E value of 2.4 (± 0.41) with a Routine respiration of 32.04 pmolO_2/s*ml/CIV (± 3.148) and ETS response of 16.52 pmolO_2/s*ml/CIV (± 1.080). The leak state was also increased to 10.53 pmolO_2/s*ml/CIV (± 1.482), resulting in a L/E ratio of 0.64 (± 0.12). Even though a large leak state was observed, the netR/E ratio remained extremely high at 1.88 (± 0.35), which is 88% above its maximal ETS respiratory capacity. A more pronounced ADP response through Complex I was also observed (15.02 ± 1.504 pmol02/s*ml/CIV) compared to CI&II (11.89 ± 2.926 pmolO_2/s*ml/CIV).

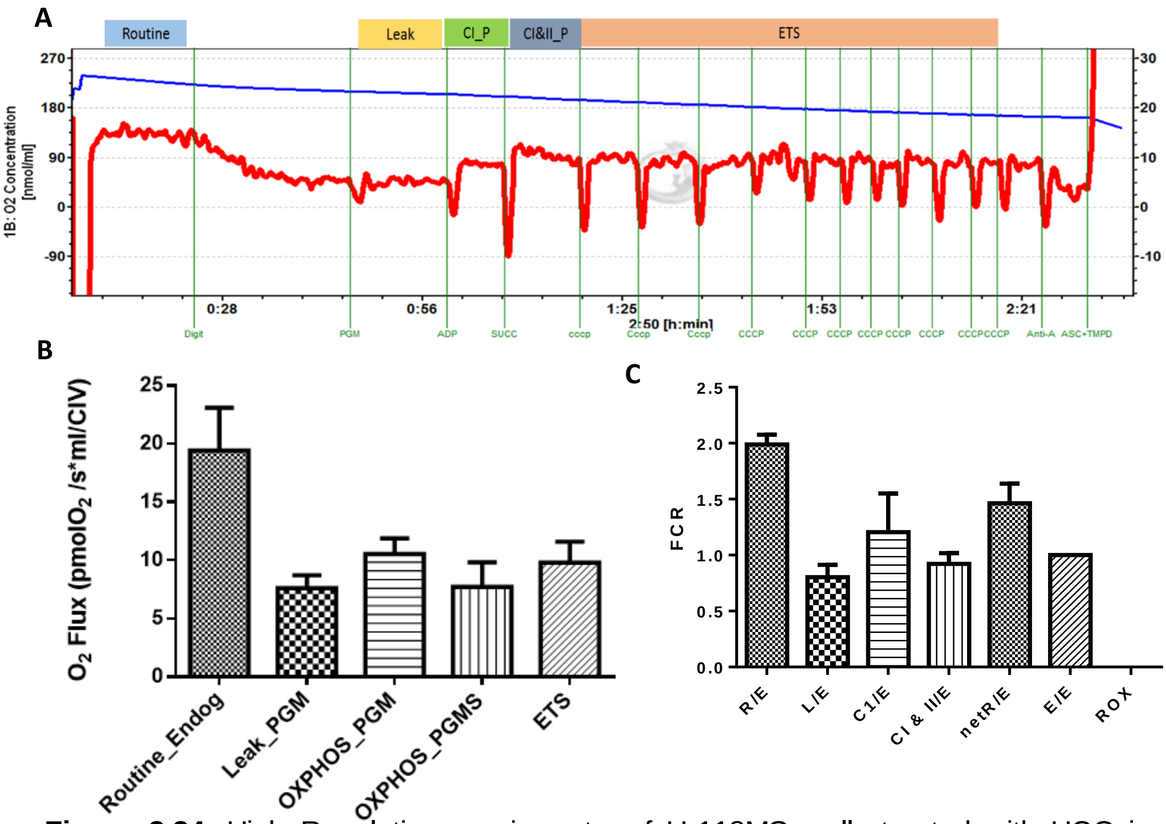

Figure 3.34. High Resolution respirometry of U-118MG cells treated with HCQ in combination with TMZ A) Representative trace of intact cell respirometry shown as O_2 flux (J_{O2}) per volume of cell suspesion (pmol/(s*ml)) (500 000 cells/ml) B) O_2 Flux values corrected for residual oxygen consumption (ROX) for the following metabolic states; Routine respiration (R) , Leak state (L), Complex I activity (C1), Complex I&II activity (C2), Electron Transfer System capacity (ETS). C) Flux control ratios representing each metabolic state ratioed to ETS capacity. N=3.

Protonophore titrations did not yield a maximal respiration beyond that of the Routine state for the HT combination group (Fig 3.30 A), resulting in a high R/E ratio of 1.85 (± 0.35). A large L/E value of 0.80 was achieved, characteristic of excessive ETS uncoupling, leading to a netR/E value of 1.463 (± 1.463), suggesting that metabolic uphold of Routine respiration operates well beyond the maximal ETS capacity. Both an ADP and Succinate response was observed, although the mean CI activity was higher than that of CI & II, with values of 10.53 pmolO_2/s*ml/CIV (± 1.345) and 7. pmolO_2/s*ml/CIV (± 2.109) respectively.

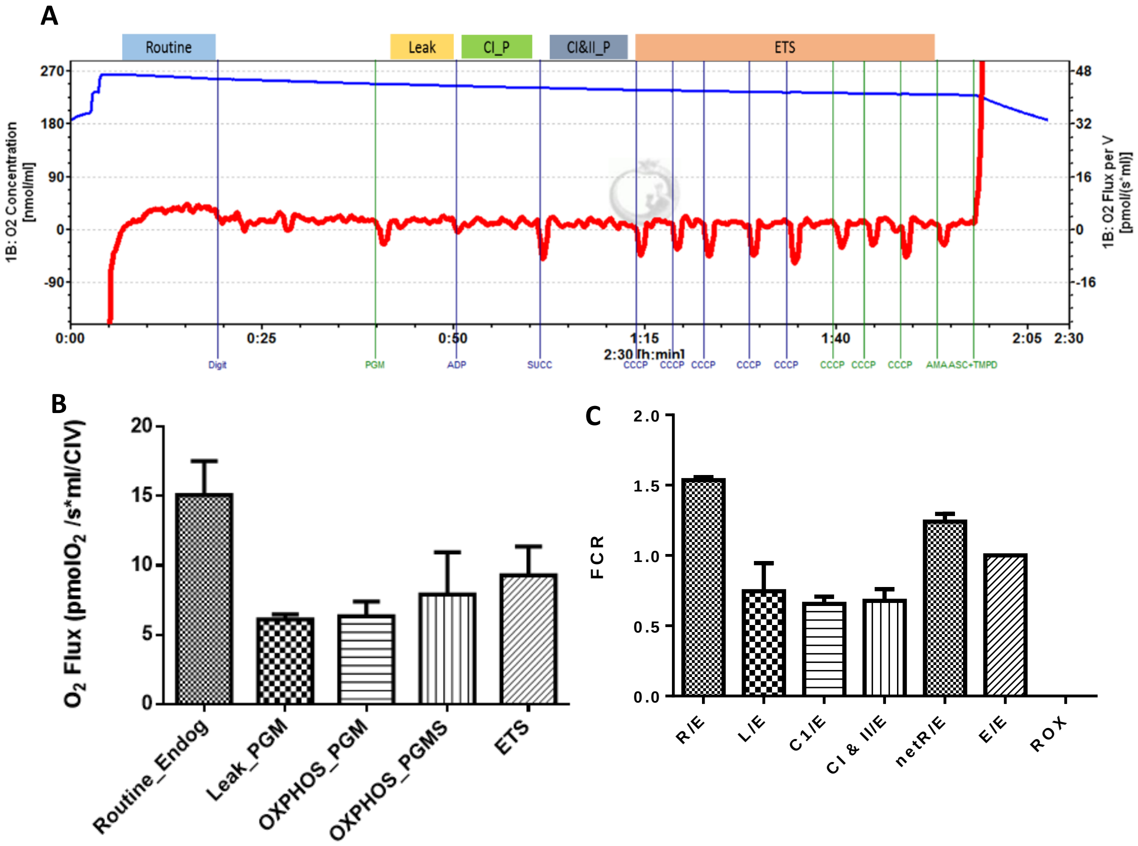

Figure 3.35. High Resolution respirometry of U-118MG cells treated with Rapamycin followed by HCQ in combination with TMZ A) Representative trace of intact cell respirometry shown as O_2 flux (J_{O2}) per volume of cell suspesion (pmol/(s*ml)) (500 000 cells/ml) B) O_2 Flux values corrected for residual oxygen consumption (ROX) for the following metabolic states; Routine respiration (R) , Leak state (L), Complex I activity (C1), Complex I&II activity (C2), Electron Transfer System capacity (ETS). C) Flux control ratios representing each metabolic state ratioed to ETS capacity. N=3.

A significant response for CCCP, ADP and Succinate could not be achieved for the RHT treatment group (Fig. 3.31). Routine respiration remained above maximal ETS (15.10 ± 2.431 pmolO_2/s*ml/CIV), although the high Leak state (6.11 ± 0.3616 pmolO_2/s*ml/CIV) decreased the netR/E value to 1.24 (± 0.055). The RHT group consequently exhibited a dyscoupled ETS, utilizing its maximal capacity to maintain phosphorylation associated respiration, whilst the high Leak state is indicative of possible membrane damage.

Therefore, induction of autophagy prior to combined inhibition proved to effectively reduce the metabolic dependence of glioma cells on mitochondrial respiration when exposed to TMZ.

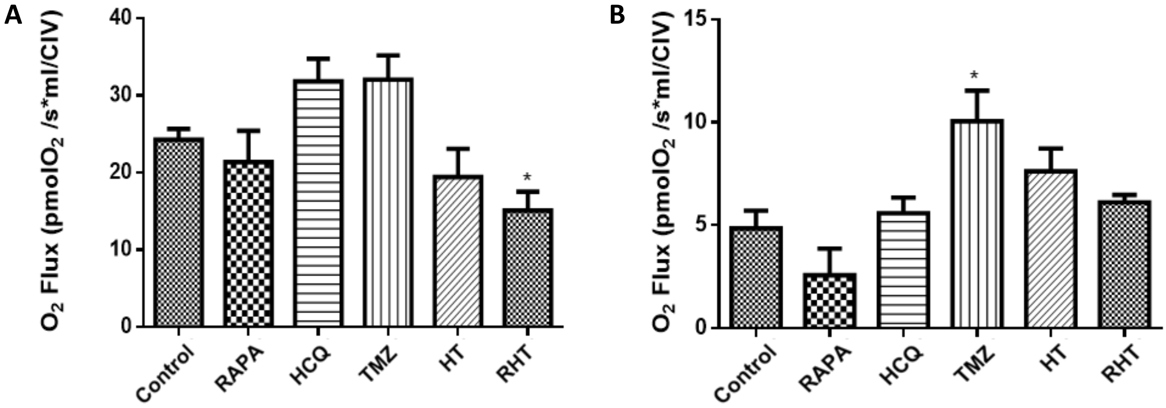

Figure 3.36. A) Routine and B) Leak state O$_2$ Flux values for Control, Rapamycin (Rapa), Hydroxychloroquine (HCQ), Temozolomide (TMZ), HCQ in combination with TMZ (HTZ) and Rapamycin pre-treamtnet followed by HCQ in combination with TMZ (RHT). N=3, *$p < 0.05$.

Comparison of oxygen consumption rates indicates that Routine respiration (Fig. 3.36A) was unperturbed following 50 nM Rapamycin (21.35 ± 4.07 pmol0$_2$/s*ml/CIV), 50 µM HCQ (31.83 ± 2.91 pmol0$_2$/s*ml/CIV) and 250 µM TMZ (32.04 ± 3.15 pmol0$_2$/s*ml/CIV) treatment compared to the untreated control group (25.11 ± 1.58 pmol0$_2$/s*ml/CIV). However, a significant decrease in Routine respiration was observed for the Rapamycin pre-treatment group (RHT) in comparison to both the untreated control and TMZ treatment group (15.10 ± 2.43 pmol0$_2$/s*ml/CIV, $p < 0.05$). The oxygen consumption flux for the HCQ pre-treatment group (HT) was significantly decreased compared to cells treated with TMZ (19.43 ± 3.66 pmol0$_2$/s*ml/CIV, $p < 0.05$), but not in comparison to the untreated control.

Proton leak, as indicated by Fig. 3.36B, was significantly enhanced following TMZ treatment only (10.06 ± 1.482 pmol0$_2$/s*ml/CIV, $p < 0.05$ vs Control 4.847 ± 0.8574), with stable O$_2$ flux observed for all other groups (Rapa 2.563 ± 1.29 pmol0$_2$/s*ml/CIV; HCQ 5.59 ± 0.75 pmol0$_2$/s*ml/CIV; HT 7.32 ± 1.11 pmol0$_2$/s*ml/CIV; RHT 6.11 ± 0.37 pmol0$_2$/s*ml/CIV).

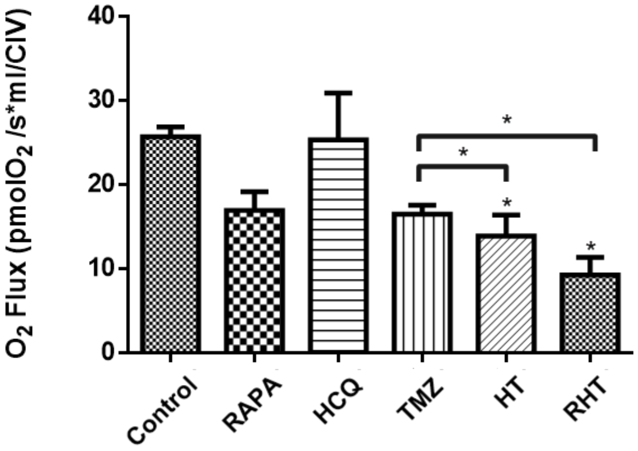

Figure 3.37. Maximal ETS response associated O_2 Flux values for Control, Rapamycin (Rapa), Hydroxychloroquine (HCQ), Temozolomide (TMZ), HCQ in combination with TMZ (HTZ) and Rapamycin pre-treamtnet followed by HCQ in combination with TMZ (RHT). N=3, $^*p < 0.05$.

The maximal CCCP response was not altered significantly by autophagy induction with 50 nM Rapamycin (16.98 ± 2.23 $pmol0_2$/s*ml/CIV), autophagy inhibition with 50 µM HCQ or treatment with 250 µM TMZ compared to control cells (25.75 ± 1.17 $pmol0_2$/s*ml/CIV)) (Fig. 3.37). However, HCQ pre-treatment in combination with TMZ (HT), as well as Rapamycin pre-treatment (RHT) in combination with HT decreased the maximal ETS capacity to 13.91 $pmol0_2$/s*ml/CIV (± 2.51) and 9.29 $pmol0_2$/s*ml/CIV (±2.089) compared to both the control and TMZ treatment groups ($p < 0.05$)

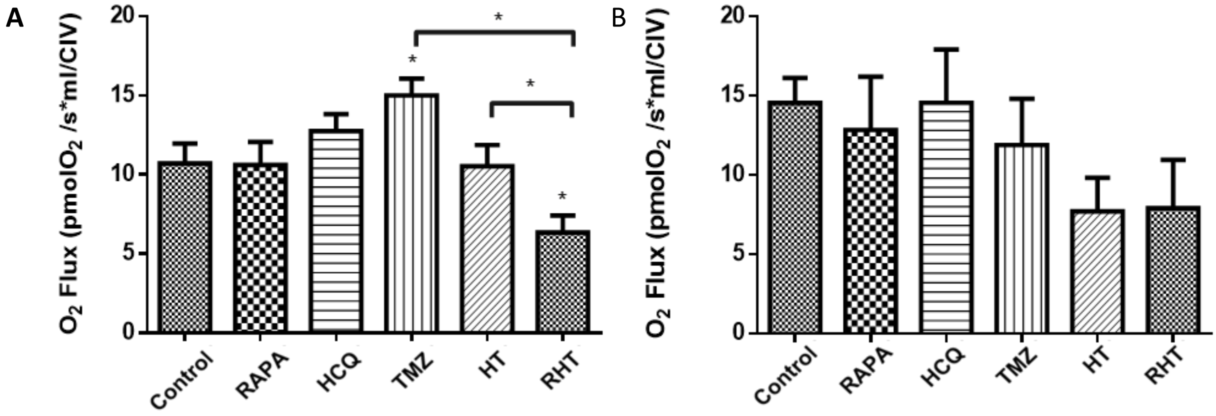

Figure 3.38. A) OXPHOS through Complex I and B) OXPHOS through Complex I&II associated O_2 Flux values for Control, Rapamycin (Rapa), Hydroxychloroquine (HCQ), Temozolomide (TMZ), HCQ in combination with TMZ (HTZ) and Rapamycin pre-treatment followed by HCQ in comination with TMZ (RHT). N=3, *$p < 0.05$.

OXPHOS through Complex I was unperturbed by treatment with 50 nM Rapamycin (10.61 ± 1.47 pmolO_2/s*ml/CIV) and 50 µM HCQ (12.75 ± 1.070 pmolO_2/s*ml/CIV) compared to control cells (10.71 ± 1.25 pmolO_2/s*ml/CIV) (Fig. 3.38 A). Similarly, the additive effect of OXPHOS through complex II was not enhanced in these groups after addition of Succinate (Rapa 12.84 ± 3.37; HCQ 14.56 ± 3.36 vs Control 14.54 ± 1. pmolO_2/s*ml/CIV). OXPHOS through complex I was significantly enhanced following 24 hours incubation with TMZ (250 µM) (15.02 ± 1.05 vs Control 10.71 ± 1.25 pmolO_2/s*ml/CIV, $p < 0.05$), though oxygen consumption decreased to control levels following pre-treatment with HCQ (10.53 ± 1.35). Upregulating autophagy for 6 hours with Rapamycin (50 nM) prior to incubation with HCQ (50 µM) and TMZ (250 µM) caused a significant decrease in Complex I associated OXPHOS compared to Control, TMZ and HT treatment groups (6.35 ± 1.07 vs Control 14.54 ± 1.58, TMZ 15.02 ± 1.05 and HT 10.53 ± 1.35 pmolO_2/s*ml/CIV, $p < 0.05$), suggesting that OXPHOS plays a critical role in glioma chemotherapeutic resistance and can be impaired through coordinated autophagy modulation. However, after addition of Succinate, the additive effect of OXPHOS through Complex II was not enhanced in these groups (TMZ 11.89 ± 2.93; HT 7.71 ± 2.11 and RHT 7.91 ± 3.05 pmolO_2/s*ml/CIV).

3.11 Autophagy modulation in combination with TMZ decreased lactate production.

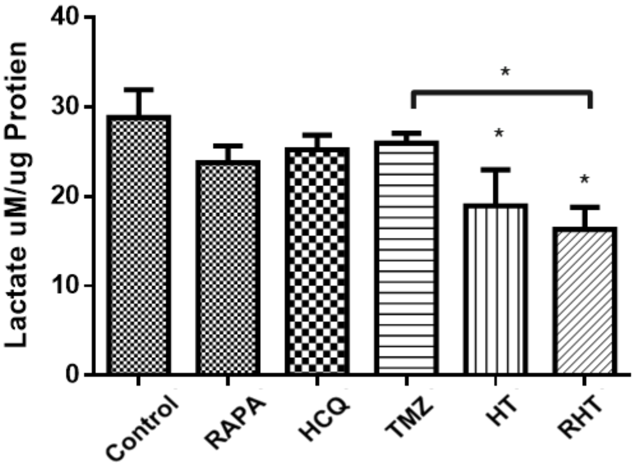

Figure 3.39. Concentration of Lactate in growth medium under control conditions (C), after treatment with Rapamycin (Rapa), Hydroxychloroquine (HCQ), Temozolomide (TMZ), HCQ in combination with TMZ (HTZ) and Rapamycin pre-treatment followed by HCQ in combination with TMZ (RHT). N=3, *p < 0.05.

In order to assess anaerobic glycolysis, the concentration of lactate produced per mg of protein in culture media was assessed under control conditions, lactate production was measured at 30 µM/µg (± 3.11 µM/µg), which remained unaltered after upregulation of autophagy with Rapamycin (50 nM) (23.78 ± 1.87 µM/µg), inhibition with HCQ (50 µM) (25.22 ± 1.63 µM/µg) and treatment with TMZ (250 µM) for 24 hours (25.95 ± 1.20 µM/µg). Pre-treatment with HCQ (HT) and Rapamycin (RHT) decreased lactate production significantly to 18.95 µM/µg (± 4.03 µM/µg vs Control p < 0.05) and 16.31 µM/µg (± 2.47 µM/µg vs Control, p< 0.05).

3.12 Form and Function

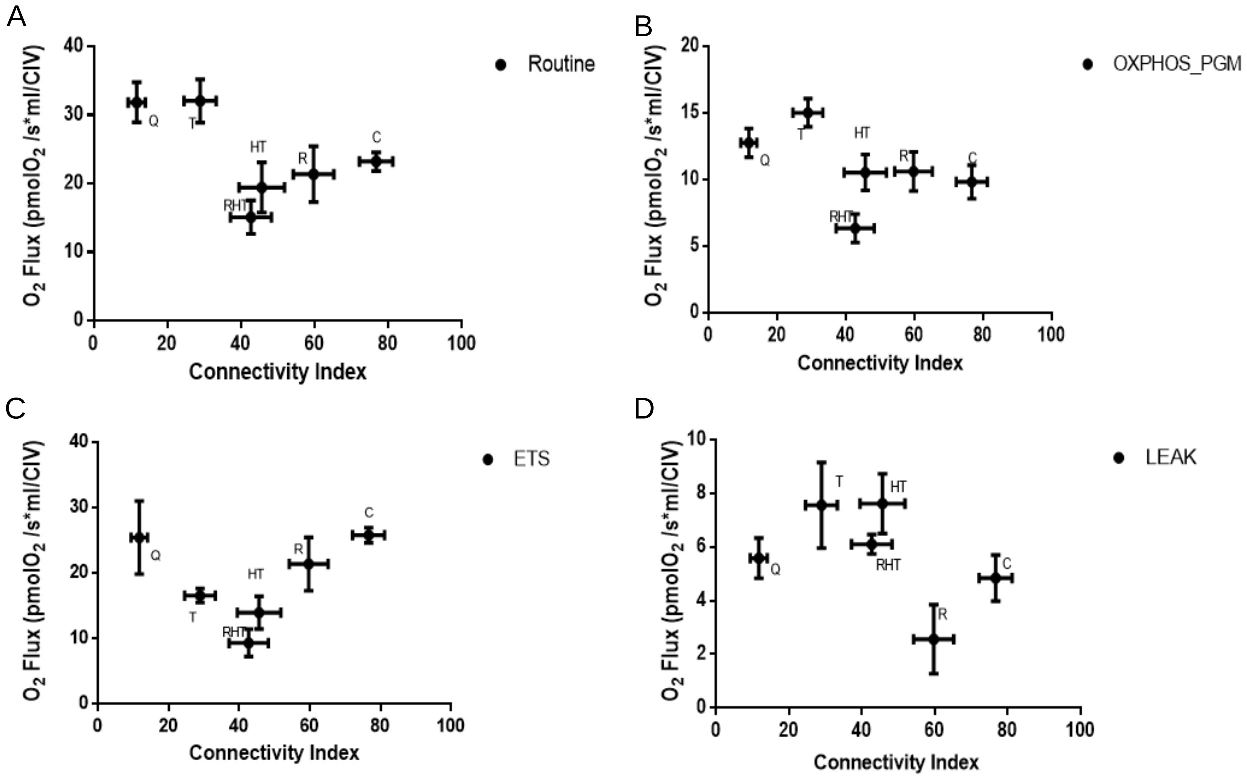

Figure 3.40. Correlation of O_2 flux with Connectivity Index for all groups of interest for A) Routine B) OXPHOS through Complex I C) ETS and D) LEAK states.

Correlating O_2 flux with the Connectivity Index (Fig. 3.40) indicates that although the HCQ and TMZ groups presented with the least amount of connectivity, their Routine and OXPHOS (Fig. 3.40 A and B) associated respiration was above that of healthy control cells. Importantly, the two intermediately connected groups HT and RHT produced the least effective ETS response (Fig. 3.40 C) and also had high Leak associated oxygen consumption rates (Fig. 3.40 D). These data suggest that attributing bioenergetic efficiency to morphological changes in isolation of respiratory analysis can be misleading and may mask the true cellular stress response.

Chapter 4: Discussion

The capacity of GBM to resist cell death onset through chemotherapy is currently an active area of investigation in the field of molecular neuro-oncology. Initial attempts to identify the key genetic markers associated with resistance lead to the identification of enhanced DNA repair through MGMT mediated signalling in highly malignant tumours (Hegi *et al*., 2005). Cell cycle and angiogenesis related molecular regulators such as AKT, PTEN and Ras have also shown to be mutated in these tumours (Yan *et al*., 2009). However, combining growth factor receptor inhibitors or anti-angiogenic reagents with chemotherapy have not been able to enhance mean patient survival time. Furthermore, excessive exposure to chemotherapy and radiation has been shown to decrease patient quality of life following treatment, further contributing to decreased patient survival time (Stupp *et al*., 2009).

This has led to a recent resurgence in studies focussing on the metabolic upkeep of GBM pathogenesis (Seyfried *et al*., 2015). Challenging Warburg's theory, current evidence suggests that both oxidative and glycolytic metabolic pathways are involved in glioma progression, depending on their level of malignancy (Griguer *et al*., 2013; Marin-Valencia *et al*., 2012; Kennedy *et al*., 2013). The involvement of the autophagic protein degradation pathway in metabolism has also garnered much interest with regards to its role in tumour bioenergetics. In this regard, autophagy induction has been observed in response to treatment of glioma cells with the standard of care chemotherapeutic TMZ (Zou *et al*., 2014). However, given the molecular crosstalk between regulators of apoptosis and autophagy, enhanced cell death onset has been observed in studies combining either autophagy inducers (such as Rapamycin or Temsirilomus) or inhibitors (such as Hydroxychloroquine of Bafilomycin) with chemotherapy. Therefore, it remains to be elucidated which degree of autophagy modulation is required to optimally enhance cell death onset in GBM. Furthermore, the effect of altered autophagy mediated protein degradation on oxidative phosphorylation (OXPHOS) and glycolysis in the context of GBM metabolism has yet to be explored.

The mitochondrial network is a highly motile reticulum which is maintained through constant fission and fusion events. Although evidence exists for the involvement of OXPHOS in glioma metabolism, much controversy surrounds the diagnostic attributes of mitochondrial morphology. Fragmented mitochondrial networks are characteristic in Parkin-deficient cells, wherein impaired clearance of damaged mitochondria causes an increase in the amount of individual mitochondrial subunits (Narendra *et al*., 2008). Conversely, enhanced fragmentation has been observed in cells exposed to excessive glucose concentrations (Yu *et al*., 2006). Importantly, it remains unresolved whether altered mitochondrial morphology and dynamics are directly associated with glioma OXPHOS capacity.

We therefore attempted to elucidate whether autophagy modulation would impair GBM metabolism to the extent of initiating cell death. In contrast to previous *in vitro* models and current clinical trials, combined autophagy induction with subsequent inhibition was hypothesised to debilitate glioma metabolism most prominently in terms of both OXPHOS and glycolytic activity compared to autophagy inhibition only, combined with chemotherapy. Autophagic flux was assessed in terms of LC3 and p62 expression, with expression of cleaved Caspase 3 and cleaved PARP taken as indicative of apoptosis onset. Extensive investigation of mitochondrial morphology and dynamics was conducted through photoactivation and live cell microscopy and contextualised with markers for mitochondrial fission (DRP1) and fusion (MFN1, MFN2 and OPA1). In this regard, we constructed and employed image processing algorithms capable of determining the amount of mitochondrial connectivity and compared the degree of scaling between mitochondrial networks in terms of their area and perimeter measurements.

4.1 Coordinated autophagy modulation combined with chemotherapy decreased cell viability and enhanced cell death onset

The autophagy modulators chosen for this study were Rapamycin, which induces autophagy through mTOR inhibition, and Hydroxychloroquine (HCQ), which impairs autophagic activity through lysosomal deacidification. Our viability and Western Blot data indicate that the chosen concentrations of autophagy modulators were not able to induce apoptotic cell death in glioma cells. An increase in reductive capacity was observed following 50 nM Rapamycin treatment (Fig. 3.1) and only a 20% decrease was caused by incubation with 50 µM HCQ (Fig. 3.2 A). Cleavage of caspase 3 results from apoptosome formation and is responsible for PARP cleavage, which leads to DNA fragmentation and ultimately apoptosis onset. Expression of both cleaved-caspase 3 (Fig. 3.8) and cleaved-PARP (Fig. 3.9) remained unperturbed in these groups, leading us to conclude that these concentrations were non-lethal in terms of apoptosis onset and therefore suitable to assess sensitisation effects to overcome glioma chemoresistance.

Co-treatment of glioma cells with HCQ for 6 hours in the presence of TMZ, followed by TMZ treatment for 18 hours (HT) decreased reductive capacity, but not to a greater extent than that of solitary TMZ incubation (Fig. 3.5). Comparing these data with cell death marker expression, cleaved-caspase 3 expression was not enhanced compared to Control (Fig. 3.8), although a significant increase in cleaved-PARP expression was indeed observed (Fig.3.9). Pre-treatment with Rapamycin for 6hours, followed by the HT regiment significantly decreased reductive capacity by 50%, thereby proving to be considerably more lethal than either the TMZ or HCQ pre-treatment group. This is further supported by our Western Blot data, indicating increased expression of both cleaved-caspase 3 (Fig. 3.8) and cleaved-PARP (Fig. 3.9). Although a recent phase I dose escalation study by Rangwala *et al*., (2014) has assessed the combination of mTOR inhibition through temsirolimus with HCQ and TMZ in patients with advanced solid tumours, temsirolimus was administered weekly following combined HCQ and TMZ treatment. Our observation that inducing autophagy prior to inhibition and chemotherapy enhanced cell death onset in GBM cells is therefore, to the best of our knowledge, a novel finding and warrants further investigation.

4.2 Coordinated modulation impaired autophagic degradative activity

Assessing the amount LC3-II protein expression (Fig. 3.6) revealed a high basal autophagic flux for glioma cells under control conditions. LC3-II associates with mature autophagosomal membranes and has been shown to play a role in selecting proteins for degradation. Although Rapamycin treatment did not alter LC3-II expression significantly compared to the control, a large increase in autophagosomal accumulation was induced by Bafilomycin A1 (Baf) treatment, signifying a high rate of autophagosomal production in the presence of Rapamycin (Fig. 3.6). This confirms the notion of cancer cells having enhanced autophagic activity, also deemed as autophagy addiction (Mathew & White, 2011). Enhanced LC3-II protein levels were observed after HCQ treatment, although accumulation following Baf treatment was non-significant, indicating decreased autophagic flux (Fig. 3.6). As a further measure of functional autophagy, p62 expression was assessed, as it associates with ubiquitinated proteins marked for degradation. Comparing the LC3-II data with p62 protein levels (Fig. 3.7) indicates that, although LC3-II expression was moderately impaired by HCQ treatment, the significant accumulation of p62 following Baf treatment suggests that protein degradation was either not disrupted or an increase in synthesis of p62 was induced.

A decrease in LC3-II expression for the Baf untreated group was observed following TMZ treatment. Given that protein extraction occurred at a single time point, regardless of the rate of autophagic degradation, the decrease in initial LC3-II expression can be indicative of an already enhanced flux and not necessarily a decrease in autophagosomal production (Barth *et al*., 2010). This is supported by the significant increase in expression caused by Baf treatment, indicating an increase in autophagic flux. Markedly enhanced LC3-II expression was caused by both HT and RHT treatment, with unaltered expression following Baf treatment (Fig. 3.6).

Therefore, although autophagosomal production was enhanced, clearance of the autophagosomal pool was likely impaired. Conversely, significantly enhanced p62 expression was observed for both the HT and RHT Baf treatment groups, suggesting that protein degradation through autophagy was not diminished. Sahani *et al*., (2014) have shown that, although p62 accumulation is associated with impaired autophagic degradation, its synthesis following transcriptional upregulation is also highly dependent on amino-acid availability. In MEF cells under prolonged starvation, p62 synthesis was shown to be restored by both autophagy derived and exogenous amino acids (Sahani *et al*., 2014). Therefore, under optimal growth conditions, impaired autophagy would not necessarily lead to unaltered p62 levels following Baf treatment. The *in vitro* model presented in our study made use of serum and amino-acid supplemented growth medium, therefore making *de novo* synthesis of p62 possible even when autophagy was impaired.

The robust response in LC3-II accumulation following HT treatment strengthens the notion that TMZ enhanced autophagic flux (Fig. 3.6). Given an increased degradative activity, the capacity to provide autophagy derived substrates is enhanced, which may serve as an adaptive response to meet cellular metabolic demands. If lysosomal deacidification was to occur prior to this induction, the subsequent increase in autophagolysosomes would present with impaired degradative ability, thereby inhibiting clearance of the already increased autophagosomal poolsize. Our results support this view (Fig. 3.6), and indicate that enhanced autophagosomal flux through Rapamycin exacerbated this effect. By increasing the autophagosomal pool size with Rapamycin before lysosomal deacidification (HCQ mediated), it is possible that autophagosome production was enhanced beyond its maximum capacity, rendering the TMZ response ineffective. Furthermore, it is possible that enhanced degradation before TMZ treatment decreased the amount of free amino acids necessary for anaplerosis of key TCA cycle intermediates to facilitate chemotherapeutic resistance (Mizushima & Klionsky 2007).

4.3 Autophagy modulation affects mitochondrial dynamics and morphometrics

In order to elucidate whether mitochondrial bioenergetics were indeed affected by autophagy modulation, the mitochondrial phenotype was assessed in terms of its fission and fusion dynamics. The regulation of both fission and fusion events have previously been implicated in metabolic efficiency. We therefore utilised a unique photoactivation protocol, as first described by Karbowski *et al*. (2004), to quantify the rate at which fission and fusion occurs. Furthermore, we designed image processing algorithms to assess the amount of mitochondrial network connectivity present in glioma cells. Morphometric data were then contextualised with the expression of outer mitochondrial membrane (OMM) fusion proteins MFN1 and MFN2, the inner mitochondrial membrane (IMM) fusion protein OPA1 and the fission protein DRP1.

4.3.1 Impaired autophagic degradation activity decreased mitochondrial fission and fusion rate

Gradual loss of signal intensity was observed over time for cells under control conditions and following treatment with Rapamycin (Fig. 3.10 A and B, Fig. 3.11 A and B), with stable signal intensity reached after 10 minutes, indicative of a highly motile network. In accordance with Karbowski *et al*., (2004), network fragmentation did indeed impair the rate of mitochondrial fusion (Fig. 3.17). This is evident from Fig. 3.12, where the spread of signal intensity out of the indicated region of interest (ROI) was impaired after incubation with HCQ. Interestingly, the photoactivated ROI in the TMZ treated mitochondrial network displayed the same decay slope as that for HCQ treated cells, although a more tubular network structure was present (Fig. 3.13). A decreased rate of fusion was also observed for HT and RHT treated cells (Fig. 3.14 and 3.15), indicating that combined autophagy modulation with chemotherapy impaired mitochondrial fission and fusion dynamics.

Although linear regression through these slopes indicate that signal decay was significantly slower for the HCQ, TMZ, HT and RHT groups compared to the control and Rapamycin, membrane fusion was not completely inhibited (Fig. 3.17). Stable expression of MFN1 and MFN2 across all treatment groups corroborate this observation, with decreased expression only observed following RHT treatment, albeit not deleteriously (Fig. 3.26 and 3.27). Therefore, outer membrane fusion was likely not affected. A similar trend was observed for DRP1 expression, staying consistent until Rapamycin pre-treatment occurred, indicating that fission was also occurred in an unperturbed manner (Fig. 3.29). Notably, decreased OPA1 protein expression was observed for the TMZ, HT and RHT groups, which signifies a loss in

IMM mediated fusion (Fig. 3.28). Given that the mito-PA-GFP was associated with the OMM, signal decay was possibly the result of OMM fusion and subsequent fission events, with impaired IMM membrane fusion inhibiting complete refusion to neighbouring mitochondria which resulted in a decreased rate of fusion. These findings are in accordance with that of Mishra *et al*. (2014) where decreased OPA1 expression was also shown to decrease mitochondrial fusion rate. Moreover, our results partly contradict that of Chen *et al*. (2003) as neither a decrease in MFN1 or MFN2 was observed for the treatment groups that displayed a decreased mitochondrial fusion rate, with the exception being the RHT treatment group. However, our observation that both an increase and decrease in autophagic degradation activity in response to TMZ and coordinated adjuvant autophagy modulation (Fig. 3.6) is associated with decreased mitochondrial fission and fusion rate is, to the best of our knowledge, a novel finding.

Although the individual amount of fission and fusion events were not quantified in this study, the loss of IMM fusion is indicative of a state of transient fusion, first characterised by Liu *et al*. (2009), wherein brief fusion events take place, followed by an immediate fission event. Given that DRP-1 expression was observed, OMM fusion through solitary mitofusin activity could promote transient fusion, resulting in decreased sub-distribution of mito-PA-GFP. Furthermore, given the speed at which these processes occur, image acquisition only took place within a single focal plane. It is therefore possible that fusion in the z-region occurred, masking the true rate of signal decay.

4.3.2 Coordinated autophagy modulation resulted in intermediately connected mitochondrial networks

Morphological analysis was conducted on 3D rendered live cell images. Although relatively few images could be acquired in the z-region during live cell time lapse acquisition, it allowed for a more accurate depiction of mitochondrial network distribution. Consequently, loss of network connectivity was observed for all treatment groups associated with impaired mitochondrial motility (Fig. 3.17 and 3.25). A large population of network clusters presented with small area and perimeter values in control cells, indicating that healthy glioma mitochondrial bioenergetics is characterised by the existence of both fragmented and tubular mitochondria (Fig. 3.18). Although a decrease in the mean number of clusters increased area/perimeter values following Rapamycin treatment suggests more hyperfused clusters, the average amount of connectivity over time did not differ significantly from the control (Fig. 3.19 and 3.25). This is supported by the same fission/fusion rate observed between these groups (Fig. 3.17). A substantial decrease in connectivity was observed in HCQ and TMZ treated cells

(Fig. 3.25), with both displaying a large amount of individually fragmented cluster populations (Fig. 3.20, 3.21). Of importance is that an intermediate degree of network connectivity was identified for HT and RHT treated cells (Fig. 3.25). Surprisingly, less membrane structures were identified in RHT treated cells, with many clusters yielding large area and perimeter values (Fig. 3.24). As a result, the degree of scaling was noticeably more linear in the RHT group compared to all other groups. Therefore, although an impaired fusion rate was associated with decreased connectivity, the morphology of individual mitochondrial network clusters differed between excessively fragmented and intermediately connected networks. In this regard, the image processing algorithms employed in this study proved to be a more sensitive method in comparison to previous studies relying only on the length of mitochondrial subunits (Rossignol *et al*., 2004) or measuring the degree of branching (Mortiboys *et al*., 2008).

4.3.4 Loss of network connectivity in mitochondrial networks is due to decreased fusion and not increased fission

Unaltered mitofusin protein expression (MFN1 and MFN2) was found for treatment groups that displayed the least amount of connectivity, indicating that outer membrane fusion was not impaired. Similarly, DRP1 protein levels were not enhanced in these groups (HCQ and TMZ), indicating that enhanced fission was not solely responsible for enhanced fragmentation. However, decreased OPA1 protein levels were found for fragmented and intermediately connected networks, indicating that diminished inner membrane fusion resulted in incomplete fusion. Therefore, loss of OPA1 protein levels proved a better indicator of decreased network connectivity than a decrease in DRP1 protein levels. Thus, the possibility exists that decreased connectivity was more likely attributable to decreased inner membrane fusion and not increased fission. In this regard, RHT treatment caused a significant decrease in both OPA1 and DRP1 expression (Fig. 3.28 and 3.29). Therefore, it is possible that decreased fission regulation altered morphological distribution, given that larger individual clusters were observed to a greater extent in RHT treated cells compared to TMZ and HT (Fig. 3.24).

Neither decreased OPA1 nor increased DRP1 was observed following HCQ treatment, yet these cells displayed the highest degree of fragmentation (Fig. 3.24 and 3.25). The mechanism through which HCQ induces fragmentation therefore remains to be elucidated, although it is possible that other fission related proteins such as mitochondrial fission factor (MFF) or Fis1 could have been upregulated (Losón *et al*., 2013).

4.4 Decreased degradation through autophagy impaired ETS coupling and OXPHOS efficiency

Previous studies have indicated mitochondrial and autophagic dysfunction as necessary for cancer progression. Although this holds true for early stage cancer pathogenesis, established solid tumours such as GBM have been shown to be dependent on OXPHOS for metabolic proficiency. Furthermore, initial research in this field was conducted under the assumption that autophagy operates as a mode of cell death in the same way as apoptosis or necrosis does. More recent studies have challenged this view, indicating that autophagy is metabolically regulated and assists rather than executes cell death (Rabinowitz & White 2010; Degenhardt *et al*., 2006; Rosenfeld *et al*., 2014; Galluzzi *et al*., 2015). In the context of cancer metabolism, autophagy has been implicated in glioma metabolic efficiency and found to be upregulated in response to cytotoxic stress.

Previous work by Pasdois *et al*., (2003) has indicated the importance of Complex I associated respiration during the growth phase of C6 glioma cells. Under control conditions, U-118MG cells were found to utilise most of their ETS capacity to maintain endogenous routine respiration, displaying a high amount of complex I&II associated respiration. This indicates a high basal metabolic demand (Fig. 3.30), which correlates well with control LC3-II protein levels which represent a high basal autophagic flux (Fig. 3.6). Upregulation of autophagy increased phosphorylation associated respiration (Fig. 3.31) beyond its maximal ETS capacity and expressed a large increase in LC3-II expression following Baf treatment. Of note, the same outcome was observed following HCQ treatment, for which partial inhibition of autophagy was shown (Fig. 3.6). Therefore, glioma cells were able to adapt to autophagy modulation through partial uncoupling of the ETS.

Oliva *et al*., (2011) have demonstrated that TMZ resistant glioma cells displayed a greater amount of mitochondrial coupling than commercially available U-251 cell lines in response to chemotherapy. Our data indicate increased dependence on complex I associated OXPHOS in response to TMZ, although an increased amount of proton leak and decreased ETS capacity was displayed by the U-118MG cell line (Fig. 3.33). Therefore, although TMZ could be tolerated, ETS coupling was still decreased. Importantly, a significant increase in OXPHOS through Complex I was found in response to TMZ as well as increased autophagic flux (Fig. 3.6 and 3.38 A). Autophagy could therefore have been upregulated as a metabolic stress response, enhancing TCA cycling and thereby promoting glioma survival through complex I associated respiration. Importantly, this occurred at a TMZ concentration that was not inherently lethal to cell viability (Fig. 3.5, 3.8 and 3.9), suggesting that impairment of autophagy could diminish this response.

Partial inhibition of autophagy combined with TMZ did however not impair OXPHOS, although it was still maintained at control levels (Fig. 3.38 A). Furthermore, decreased ETS coupling efficiency was observed for the HT group (Fig. 3.34 and 3.37). Importantly, both the ETS and OXPHOS capacity of the individual HCQ treatment group remained the same as control levels. Given the viability and protein expression results (Fig. 3.5, 3.8 and 3.9), combining partial HCQ mediated autophagy inhibition with TMZ (HT) did not alter glioma mitochondrial respiratory output considerably, though oxidative respiration was maintained at the expense of ETC uncoupling.

Cells exposed to autophagy upregulation prior to HT treatment (RHT) presented with a substantially decreased OXPHOS (Fig. 3.38 A) and ETS (Fig. 3.37) coupling capacity, as well as low endogenous Routine respiration (Fig. 3.36). Since treatment group displayed both an accumulation in LC3-II (Fig. 3.6) and enhanced cell death markers (Fig. 3.8 and 3.9), dual autophagy modulation proved to effectively decrease glioma chemotherapeutic resistance by decreasing autophagic flux and mitochondrial respiratory efficiency.

Evidence for the exact anaplerotic relationship between autophagic degradation and the production of key intermediates for TCA cycling is scarce. Though it is possible that free amino acids can enter the TCA cycle at various points to replenish metabolites such as acetyl-CoA, glutamate (for conversion to alpha-ketoglutarate), succinyl-CoA and fumarate (Mathew & White 2011), it remains to be proven whether all or only certain metabolites are replenished in the context of GBM. The coupling control protocol utilised in our study assessed ADP phosphorylation capacity in the presence of pyruvate, malate, glutamate and succinate. It is therefore possible that the enhanced ADP response in TMZ treated cells was the result of cytosolic depletion of amino acids through enhanced autophagic degradation (Fig. 3.6), resulting in a considerable increase in utilisation of pyruvate, glutamate and malate. Importantly, this response was decreased in RHT treated cells, raising the possibility that Rapamycin pre-treatment decreased the availability of free amino acids, with subsequent lysosomal impairment combined with TMZ treatment leading to inefficient TCA cycling. Apoptosis onset through caspase activation therefore further impaired both Complex I and II activity, compromising the utilisation of TCA cycle derived NADH after addition of pyruvate, malate, glutamate and succinate (Fig. 3.35).

4.5 Coordinated autophagy modulation decreased lactate production

Our results demonstrate that in response to TMZ, lactate production remained unperturbed (Fig. 3.39), with preference given to OXPHOS through Complex I (Fig. 3.38). Of note, decreased OXPHOS capacity did not result in enhanced glycolysis. In contrast, cells treated with HT and RHT also produced substantially less lactate, demonstrating decreased glucose oxidation through glycolysis (Fig. 3.39). Decreased autophagic flux possibly resulted in less pyruvate availability, resulting in decreased glycolytic cycling and subsequently less lactate production. Targeting GBM metabolism in the clinical setting has been centred predominantly around the assumption that glucose oxidation is suppressed *in vivo* (Michelakis *et al*., 2010; Lin *et al*., 2014; Park *et al*., 2013). However, C^{13} NMR spectroscopy based studies have revealed that GBM tumours display both an oxidative and glycolytic metabolic profile (Marin-Valencia *et al*., 2012; Maher *et al*., 2012). Whether or not glucose is metabolised preferentially through the TCA cycle or glycolysis in response to coordinate autophagy modulation together with chemotherapy in GBM has not yet been established.

4.6 Elucidating the relationship between mitochondrial morphology and metabolic efficiency in GBM

4.6.1 Decreased mitochondrial coupling was found for intermediately connected, but not fragmented mitochondrial networks

Contrary to Mortiboys *et al*. (2008), increased fragmentation was not associated with decreased respiratory capacity. In fact, OXPHOS capacity remained unaltered in HCQ treated cells that displayed the largest amount of fragmentation (Fig. 3.25, 3.38 A). More surprisingly is that an increase in OXPHOS was observed in TMZ treated cells that also displayed decreased connectivity (Fig. 3.33 and 3.37). Therefore, it is possible that mitochondrial fragmentation could serve as an adaptive mechanism to chemotherapy in glioma cells.

Decreased ETS capacity was found for both intermediately connected HT and RHT treatment groups (Fig. 3.37), although only RHT treated cells displayed substantially decreased OXPHOS (Fig. 3.38). With regards to autophagy modulation, Gomes *et al*. (2011) have correlated the induction of autophagy under starvation with mitochondrial elongation, hypothesising it to be a method of evading mitophagy. The results presented in this study contradict this and indicate that morphological changes could be dependent on the manner in which autophagy is induced in terms of signalling mechanisms involved.

Functionally, fragmented mitochondrial networks have been observed in cell types with defective OXPHOS (Koopman *et al*., 2005; Kwong *et al*., 2007; Sauvanet *et al*., 2010). Moreover, Yu *et al*., (2006) have shown that in glucose rich contexts, when pyruvate must be catabolised at a high rate, DRP-1 dependent fragmentation is observed in cardiac cells. Surprisingly, inactivation of Drp1 dramatically inhibited pyruvate uptake, decreased respiration and enhanced ROS production. With regards to fusion, enhanced tubulation has been reported in response to metabolite restriction in various mammalian cell lines (Rossignol *et al*., 2004). However, paradoxical results have complicated this relationship, as certain cell types present with no morphological alterations under the same conditions (Rossignol *et al*., 2004). Furthermore, OXPHOS impaired primary human fibroblasts also display no apparent morphological changes. (Guillery *et al*., 2008a; Handran *et al*., 1997; Huckriede *et al*., 1995; Sauvanet *et al*., 2010).

4.6.2 Decreased expression of both DRP1 and OPA1 is associated with decreased ETS and OXPHOS efficiency

MFN1 and MFN2 expression remained unaltered in OXPHOS capable treatment groups (Fig. 3.29 and 3.38), although RHT treated cells presented with decreased MFN1 and MFN2 expression. In accordance with Mishra *et al*. (2014), decreased OPA1 expression was associated with impaired ETS capacity (Fig 3.37). Interestingly, although TMZ treatment did not impair the ETS capacity of glioma cells significantly, decreased OPA1 (Fig. 3.28) and increased proton leak was observed (Fig. 3.37). Given that DRP1 expression in TMZ treated cells remained much the same as that of the control, the disrupted membrane integrity associated with the enhanced LEAK state could be indicative of enhanced fission without effective fusion. DRP1 expression also remained unaltered for the Rapamycin, HCQ and HT treatment groups (Fig. 3.29).

Although these data seemed conflicting, given that network fragmentation was observed following HCQ, TMZ and HT treatment, these groups displayed efficient OXPHOS capacity, strengthening the case for DRP1 as an important metabolic regulator. Consequently, decreased OXPHOS, ETC and Routine respiration were observed for RHT treated cells.

Extensive investigation has recently been conducted on the involvement of fission and fusion proteins in metabolic sensing and mitochondrial efficiency. Mishra *et al*. (2014) have reported that mouse embryonic fibroblast (MEF) cells devoid of MFN1 did not decrease their OXPHOS capacity. However, by altering growth media substrates, Mishra *et al*. (2014) did show OPA1 cleavage to be affected by altered OXPHOS requirements, suggesting that inner membrane fusion is more critical to electron transport chain efficiency than outer membrane fusion. Xie *et al*. (2015) observed that silencing DRP1 impaired growth, decreased oxygen consumption and induced apoptosis in brain tumour initiating cells (BTICs). Furthermore, AMPK activation was shown in BTICs under these conditions, indicating that impaired DRP1 expression can lead to metabolic stress in cancer cells (Xie *et al*., 2015).

4.7 Mitochondrial respiration and glycolysis was impaired to the extent of promoting cell death onset

Our results demonstrate that GBM is dependent on both autophagy and oxidative phosphorylation to maintain chemotherapeutic resistance. Furthermore, impaired autophagic activity was associated with decreased lactate production. Importantly, U-118MG cells that displayed diminished OXPHOS and glycolysis were also found to have enhanced cleaved caspase 3 and cleaved PARP protein levels. This indicates that cells were metabolically compromised to the extent of inducing cell death. In this regard, Ricci *et al*. (2004) have shown that following MOMP, caspase 3 is capable of cleaving the p75 subunit of complex I, decreasing its respiratory efficiency in HeLa cells. Our results support these findings, as an increase in caspase3 and decrease in OXPHOS through complex I was observed for the RHT treatment group.

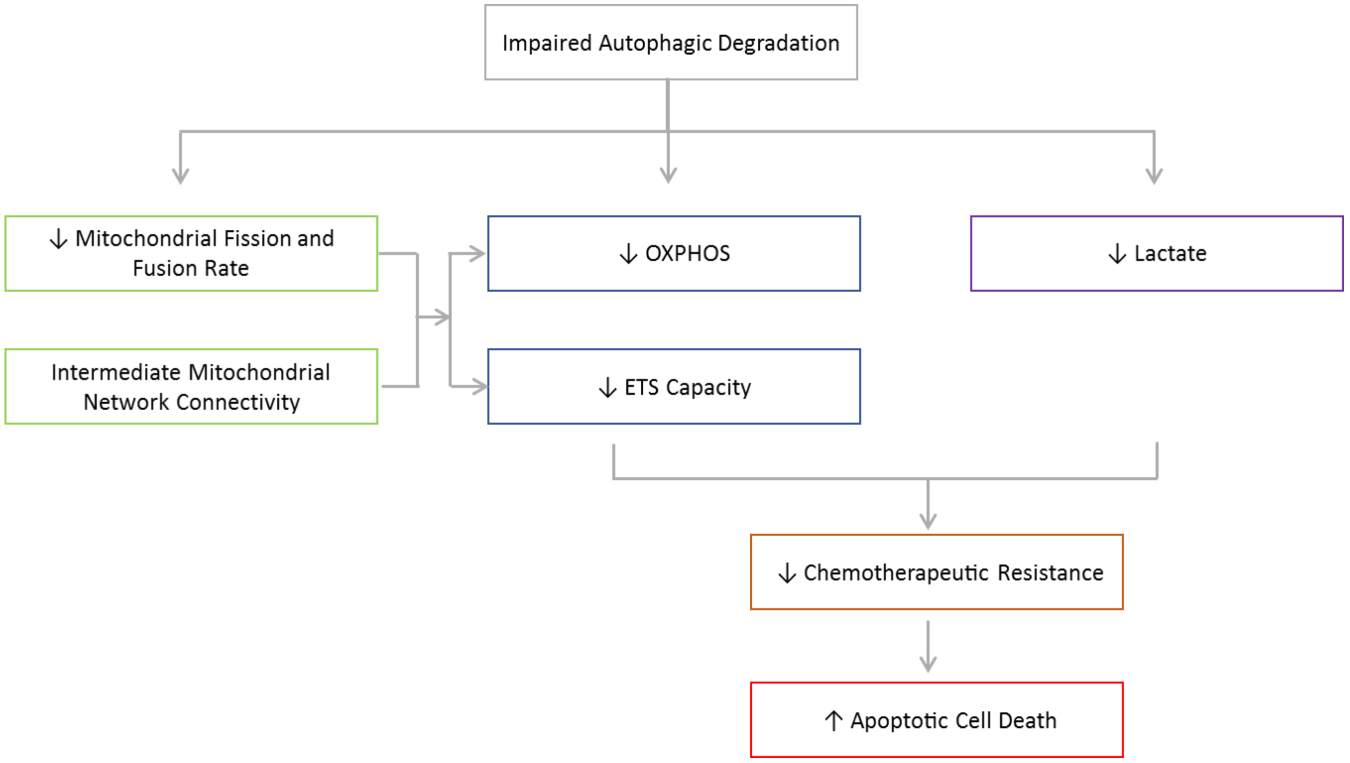

Figure 4.1. Summary of key findings.

4.8 Conclusion

The mechanism through which GBM evades cell death onset in response to chemotherapy remains largely unclear. Evidence exists that its metabolic phenotype consists of both oxidative and glycolytic components, although the effect of autophagy modulation in this context has not been fully elucidated (Marin-Valencia *et al*., 2012; Maher *et al*., 2012). Recent clinical trials utilising either autophagy inhibitors or inducers as adjuvants to chemotherapy have shown a moderate increase in patient survival time, however patient quality of life still remains poor (Rosenfeld *et al*., 2014; Rangwala, *et al*., 2014). Pioneering work by Mizushima *et al*. (2004) has shown that different organ types contain varying basal levels of autophagic flux, with studies on various cancer cell types indicating that autophagy is enhanced following exposure to chemotherapy (Kanzawa *et al*., 2004). Given the cross talk between the apoptotic and autophagic machinery, it is believed that an increase in autophagic flux beyond a defined point is necessary to facilitate cell death onset. Conversely, autophagy has been shown to be of great metabolic importance, with its inhibition leading to enhanced cell death as a result of toxic protein aggregation. Whether a direct relationship between altered autophagic flux and GBM metabolic efficiency exists has yet to be coherently investigated.

This study therefore attempted to identify the extent to which autophagy modulation in conjunction with chemotherapy affects the mitochondrial bioenergetics of GBM in relation to cell death onset *in vitro*. It was hypothesised that upregulation of autophagy prior to its inhibition would sensitise glioma cells to cell death more efficiently than only inhibition. To enhance translational value, inherently non-lethal concentrations of autophagy modulators were used in conjunction with the chemotherapeutic reagent TMZ allowing to attribute cell death sensitisation primarily to altered autophagic flux. Additionally, oxidative respiration, fission and fusion dynamics as well as network morphology was assessed. In light of the currently conflicting evidence surrounding the relationship between mitochondrial morphology and oxidative phosphorylation efficiency, we attempted to construct and employ more sensitive image analysis algorithms to distinguish between the different levels of connectivity within mitochondrial networks.

The first aim of this study was to determine the amount of autophagy modulation necessary to sensitise glioma cells to cell death. Although only a relative estimation of autophagic flux can be derived from LC3-II immunoblot data, our results demonstrate that an increase in autophagic degradation followed by partial inhibition through lysosomal deacidification successfully sensitised GBM cells to chemotherapy (Fig. 4.1). Of note, this was achieved utilizing clinically available compounds at inherently non-lethal concentrations, consisting of pre-treatment with the autophagy inducer Rapamycin, followed by inhibition with HCQ and subsequent treatment with TMZ (RHT). It was observed that, although combined partial inhibition (HT) decreased viability and autophagic flux, only cells exposed to RHT treatment displayed an increase in the apoptosis associated proteins cleaved caspase 3 and cleaved PARP, indicative of apoptosis onset. The next objective was to elucidate whether a relationship exists between impaired autophagic flux and mitochondrial bioenergetics in terms of topology, dynamics and ETS efficiency. RHT cells displayed a striking decrease in both OXPHOS efficiency and ETS capacity, whereas HCQ combined with TMZ did not impair OXPHOS capacity. To our surprise, cells that presented with impaired autophagic flux and OXPHOS displayed intermediately connected mitochondrial networks, whereas completely fragmented networks yielded a functional OXPHOS capacity. Of note, the direct relationship between impaired autophagic flux, decreased mitochondrial respiration and altered mitochondrial morphology in RHT treated cells is, to the best of our knowledge, novel and not present in current literature.

Moreover, it was observed that altered expression levels of mitochondrial morphology regulators are associated with decreased metabolic efficiency, especially with regards to the fission regulator DRP1 and the IMM fusion mediator OPA1. A decrease in both DRP1 and OPA1 protein levels was associated with impaired OXPHOS to the extent of causing cell death sensitisation. Unaltered OMM fusion protein levels were observed for MFN1 and MFN2, suggesting that although membrane fusion could occur, these events were likely transient, which possibly enhanced fission through DRP1. This was apparent in the TMZ treatment group, where decreased network connectivity was associated with decreased OPA-1 protein levels. Of note, the increased OXPHOS ability associated with enhanced fragmentation observed in the TMZ treatment group indicates that chemotherapeutic resistance is mediated through a mitochondrially associated stress response. The impairment of this response through coordinated autophagy modulation allowed us to determine extent of mitochondrial respiratory impairment necessary to achieve cell death sensitisation. In addition, we also demonstrated that impaired degradation through autophagy resulted in decreased lactate production as well as oxidative phosphorylation (Fig. 4.1).

These findings are of great clinical importance, as the inability of GBM cells to undergo efficient metabolic adaptation is impaired by coordinated autophagy modulation. Furthermore, the effect that increased autophagic flux had on cell viability highlights the importance of taking the basal metabolic flux of patient tumours into account when constructing adjuvant treatment strategies.

4.9 Recommendations and Future Outlook

Although this study demonstrated that cell death sensitisation can be achieved through coordinated autophagy modulation, the exact amount of flux perturbation necessary to achieve this remains to be elucidated. Recent work by Loos *et al*. (2014) has indicated that the same kinetic principles of multistep biochemical pathways can be applied to that of the autophagic pathway. Subsequently, the exact rate of autophagic flux can be calculated, yielding a more accurate depiction of the rate and degradative capacity of the autophagic system. Such characterisation is crucial in diseases such as cancer which, as shown in this study, is metabolically regulated. Furthermore, the anaplerotic contribution of autophagy to synthesis of TCA cycle intermediates remains to be elucidated. Understanding the nature of autophagy specific substrate preference in the context of mitochondrially associated diseases would yield great benefit in terms of predicting the outcome of adjuvant cancer therapy in the clinical setting. Moreover, prediction models have been constructed in terms of caspase activation and apoptotic regulation (Murphy *et al*., 2013). Integrating substrate provision through autophagy in such models in relation to ETS capacity and lactate production would yield many novel insights into the regulation of cell death through autophagy.

It is evident from our results that the diagnostic capability of current experimental procedures to assess autophagy and mitochondrial dysfunction calls for future research and further development of novel technologies to better characterise these processes so as to enhance clinical translation to overcome glioma cell death resistance.

References

Aki, T. et al., 2013. Impairment of autophagy: From hereditary disorder to drug intoxication. *Toxicology*, 311(3), pp.205–215.

Amaravadi, R.K. et al., 2011. Principles and current strategies for targeting autophagy for cancer treatment. *Clinical Cancer Research*, 17(4), pp.654–666.

Amaravadi, R.K. & Thompson, C.B., 2007. The roles of therapy-induced autophagy and necrosis in cancer treatment. *Clinical Cancer Research*, 13(24), pp.7271–7279.

Araque, A. et al., 1999. Tripartite synapses: Glia, the unacknowledged partner. *Trends in Neurosciences*, 22(5), pp.208–215.

Arcella, A. et al., 2013. Rapamycin inhibits the growth of glioblastoma. *Brain Research*, 1495, pp.37–51.

Arias, E. & Cuervo, A.M., 2011. Chaperone-mediated autophagy in protein quality control. *Current opinion in cell biology*, 23(2), pp.184–189.

Benard, G. & Karbowski, M., 2009. Mitochondrial fusion and division: Regulation and role in cell viability. *Seminars in cell & developmental biology*, 20(3), pp.365–374.

Bouchier-Hayes, L. et al., 2008. Measuring apoptosis at the single cell level. *Methods*, 44(3), pp.222–228.

Boya, P. et al., 2005. Inhibition of macroautophagy triggers apoptosis. *Molecular and cellular biology*, 25(3), pp.1025–1040.

Bradford, M.M., 1976. A rapid and sensitive method for the quantitation of microgram quantities of protein utilizing the principle of protein-dye binding. *Analytical Biochemistry*, 72(1-2), pp.248–254.

Bushong, E. a et al., 2002. Protoplasmic astrocytes in CA1 stratum radiatum occupy separate anatomical domains. *The Journal of neuroscience : the official journal of the Society for Neuroscience*, 22(1), pp.183–192.

Chang, C.-R. & Blackstone, C., 2007. Cyclic AMP-dependent protein kinase phosphorylation of Drp1 regulates its GTPase activity and mitochondrial morphology. *The Journal of biological chemistry*, 282(30), pp.21583–7.

Chen, H. et al., 2003. Mitofusins Mfn1 and Mfn2 coordinately regulate mitochondrial fusion and are essential for embryonic development. *Journal of Cell Biology*, 160(2), pp.189–200.

Deighton, R.F. et al., 2014. Interactions among mitochondrial proteins altered in glioblastoma. *Journal of Neuro-Oncology*, 118(2), pp.247–256.

Devin, A. & Rigoulet, M., 2007. Mechanisms of mitochondrial response to variations in energy demand in eukaryotic cells. *American Journal of Physiology - Cell Physiology*, 292(1), p.C52 LP – C58.

Dixon, S.J. et al., 2016. Ferroptosis: An Iron-Dependent Form of Nonapoptotic Cell Death. *Cell*, 149(5), pp.1060–1072.

Dunn, G.P. et al., 2012. Emerging insights into the molecular and cellular basis of glioblastoma. , pp.756–784.

De Duve, C. & Wattiaux, R., 1966. Functions of lysosomes. *Annual review of physiology*, 28, pp.435–492.

Edinger, A.L. & Thompson, C.B., 2002. Akt Maintains Cell Size and Survival by Increasing mTOR-dependent Nutrient Uptake M. Raff, ed. *Molecular Biology of the Cell*, 13(7), pp.2276–2288.

Engelman, J.A., Luo, J. & Cantley, L.C., 2006. The evolution of phosphatidylinositol 3-kinases as regulators of growth and metabolism. *Nature reviews. Genetics*, 7(8), pp.606–619.

Esteller, M., 2008. Epigenetics in cancer. *The New England journal of medicine*, 358(11), pp.1148–1159.

Galeffi, F. & Turner, D.A., 2012. Exploiting metabolic differences in glioma therapy. *Current drug discovery technologies*, 9(4), pp.280–293.

Galloway, C.A., Lee, H. & Yoon, Y., 2012. Mitochondrial morphology-emerging role in bioenergetics. *Free Radical Biology and Medicine*, 53(12), pp.2218–2228.

Galluzzi, L. et al., 2014. Metabolic control of autophagy. *Cell*, 159(6), pp.1263–76.

Galluzzi, L. et al., 2010. Mitochondrial gateways to cancer. *Molecular Aspects of Medicine*, 31(1), pp.1–20.

Galluzzi, L., Kepp, O. & Kroemer, G., 2016. Mitochondrial regulation of cell death: a phylogenetically conserved control. *Microbial Cell*, 3(3), pp.101–108.

Gomes, L.C., Di Benedetto, G. & Scorrano, L., 2011. During autophagy mitochondria elongate, are spared from degradation and sustain cell viability. *Nature cell biology*, 13(5), pp.589–98.

Gong, C. et al., 2012. Beclin 1 and autophagy are required for the tumorigenicity of breast cancer stem-like/progenitor cells. *Oncogene*, (June 2012), pp.2261–2272.

González-Polo, R.-A. et al., 2005. The apoptosis/autophagy paradox: autophagic vacuolization before apoptotic death. *Journal of cell science*, 118(14), pp.3091–3102.

Green, D.R., Galluzzi, L. & Kroemer, G., 2014. Metabolic control of cell death. *Science*, 345(6203), pp.1250256–1250256.

Green, D.R. & Levine, B., 2014. To be or not to be? How selective autophagy and cell death govern cell fate. *Cell*, 157(1), pp.65–75.

Griguer, C.E. et al., 2013. Prognostic Relevance of Cytochrome c Oxidase in Primary Glioblastoma Multiforme. *PLoS ONE*, 8(4), pp.8–13.

Guillery, O. et al., 2008. Metalloprotease-mediated OPA1 processing is modulated by the mitochondrial membrane potential. *Biology of the cell / under the auspices of the European Cell Biology Organization*, 100(5), pp.315–325.

Hegi, M.E. et al., 2005. MGMT gene silencing and benefit from temozolomide in glioblastoma. *The New England journal of medicine*, 352(10), pp.997–1003.

Hermisson, M. et al., 2006. O6-methylguanine DNA methyltransferase and p53 status predict temozolomide sensitivity in human malignant glioma cells. *Journal of neurochemistry*, 96(3), pp.766–776.

Hertz, L., Peng, L. & Dienel, G. a, 2007. Energy metabolism in astrocytes: high rate of oxidative metabolism and spatiotemporal dependence on glycolysis/glycogenolysis. *Journal of cerebral blood flow and metabolism : official journal of the International Society of Cerebral Blood Flow and Metabolism*, 27(2), pp.219–249.

Ibebuike, K., Ouma, J. & Gopal, R., 2013. Meningiomas Among Intracranial Neoplasm in Johannesburg, South Africa: Prevalence, Clinical Observations and Review of the Literature. *African Health Sciences*, 13(1), pp.118–121.

Ishihara, N. et al., 2009. Mitochondrial fission factor Drp1 is essential for embryonic development and synapse formation in mice. *Nature cell biology*, 11(8), pp.958–966.

Jose, C., Bellance, N. & Rossignol, R., 2011. Choosing between glycolysis and oxidative phosphorylation: A tumor's dilemma? *Biochimica et Biophysica Acta - Bioenergetics*, 1807(6), pp.552–561.

Kanzawa, T. et al., 2004. Role of autophagy in temozolomide-induced cytotoxicity for malignant glioma cells. *Cell death and differentiation*, 11(4), pp.448–457.

Karantza-Wadsworth, V. et al., 2007. Autophagy mitigates metabolic stress and genome damage in mammary tumorigenesis. *Genes and Development*, 21(13), pp.1621–1635.

Karbowski, M. et al., 2004. Quantitation of mitochondrial dynamics by photolabeling of individual organelles shows that mitochondrial fusion is blocked during the Bax activation phase of apoptosis. *Journal of Cell Biology*, 164(4), pp.493–499.

Karbowski, M., Neutzner, A. & Youle, R.J., 2007. The mitochondrial E3 ubiquitin ligase MARCH5 is required for Drp1 dependent mitochondrial division. *Journal of Cell Biology*, 178(1), pp.71–84.

Kennedy, C.R. et al., 2013. Differential sensitivities of glioblastoma cell lines towards metabolic and signaling pathway inhibitions. *Cancer Letters*, 336(2), pp.299–306.

Kitange, G.J. et al., 2009. Induction of MGMT expression is associated with temozolomide resistance in glioblastoma xenografts. *Neuro-oncology*, 11(3), pp.281–91.

Komatsu, M. & Ichimura, Y., 2010. Physiological significance of selective degradation of p62 by autophagy. *FEBS Lett*, 584(7), pp.1374–1378.

Kroemer, G., Mari??o, G. & Levine, B., 2010. Autophagy and the Integrated Stress Response. *Molecular Cell*, 40(2), pp.280–293.

Larsen, S. et al., 2012. Biomarkers of mitochondrial content in skeletal muscle of healthy young human subjects. *The Journal of physiology*, 590(Pt 14), pp.3349–60.

Lefranc, F. & Kiss, R., 2006. Autophagy, the Trojan horse to combat glioblastomas. *Neurosurgical focus*, 20(4), p.E7.

Liesa, M. & Shirihai, O.S., 2013. Mitochondrial dynamics in the regulation of nutrient utilization and energy expenditure. *Cell Metabolism*, 17(4), pp.491–506.

Lin, G. et al., 2014. Dichloroacetate induces autophagy in colorectal cancer cells and tumours. *British journal of cancer*, 111(2), pp.375–85.

Liu, X. et al., 2009. Mitochondrial “kiss-and-run”: interplay between mitochondrial motility and fusion-fission dynamics. *The EMBO Journal*, 28(20), pp.3074–3089.

Liu, Y. & Levine, B., 2015. Autosis and autophagic cell death: the dark side of autophagy. *Cell death and differentiation*, 22(3), pp.367–76.

Loos, B. et al., 2013. The variability of autophagy and cell death susceptibility: Unanswered questions. *Autophagy*, 9(9), pp.1270–1285.

Loos, B. & Engelbrecht, A.-M., 2009. Cell death: a dynamic response concept. *Autophagy*, 5(5), pp.590–603.

Loos, B., du Toit, A. & Hofmeyr, J.-H.S., 2014. Defining and measuring autophagosome flux—concept and reality. *Autophagy*, 10(11), pp.2087–96.

Losón, O.C. et al., 2013. Fis1, Mff, MiD49, and MiD51 mediate Drp1 recruitment in mitochondrial fission. *Molecular Biology of the Cell*, 24(5), pp.659–667.

Maher, E.A. et al., 2012. Metabolism of [U-13 C]glucose in human brain tumors in vivo. *NMR in biomedicine*, 25(11), pp.1234–1244.

Maiuri, M.C. et al., 2009. Stimulation of autophagy by the p53 target gene Sestrin2. *Cell cycle (Georgetown, Tex.)*, 8(10), pp.1571–1576.

Manning, B.D. & Cantley, L.C., 2007. AKT/PKB Signaling: Navigating Downstream. *Cell*, 129(7), pp.1261–1274.

Marin-Valencia, I. et al., 2012. Analysis of tumor metabolism reveals mitochondrial glucose oxidation in genetically diverse human glioblastomas in the mouse brain in vivo. *Cell metabolism*, 15(6), pp.827–37.

Mathew, R., Karantza-Wadsworth, V. & White, E., 2007. Role of autophagy in cancer.

Nature reviews. Cancer, 7(12), pp.961–7.

Mathew, R. & White, E., 2011. Autophagy, stress, and cancer metabolism: What doesn’t kill you makes you stronger. *Cold Spring Harbor Symposia on Quantitative Biology*, 76, pp.389–396.

Matsuda, N. et al., 2010. PINK1 stabilized by mitochondrial depolarization recruits Parkin to damaged mitochondria and activates latent Parkin for mitophagy. *Journal of Cell Biology*, 189(2), pp.211–221.

Michelakis, E.D. et al., 2010. Metabolic Modulation of Glioblastoma with Dichloroacetate. *Science Translational Medicine*, 2(31), p.31ra34 LP – 31ra34.

Mihaylova, M.M. & Shaw, R.J., 2011. The AMPK signalling pathway coordinates cell growth, autophagy and metabolism. *Nature cell biology*, 13(9), pp.1016–1023.

Miracco, C. et al., 2007. Protein and mRNA expression of autophagy gene Beclin 1 in human brain tumours. *International journal of oncology*, 30(2), pp.429–436.

Mishra, P. et al., 2014. Proteolytic cleavage of Opa1 stimulates mitochondrial inner membrane fusion and couples fusion to oxidative phosphorylation. *Cell Metabolism*, 19(4), pp.630–641.

MITCHELL, P., 1961. Coupling of Phosphorylation to Electron and Hydrogen Transfer by a Chemi-Osmotic type of Mechanism. *Nature*, 191(4784), pp.144–148.

Mizushima, N. et al., 2004. In vivo analysis of autophagy in response to nutrient starvation using transgenic mice expressing a fluorescent autophagosome marker. *Molecular biology of the cell*, 15(3), pp.1101–1111.

Mizushima, N. & Klionsky, D.J., 2007. Protein turnover via autophagy: implications for metabolism. *Annual Review of Nutrition*, 27, pp.19–40.

Mortiboys, H. et al., 2008. Mitochondrial function and morphology are impaired in parkin-mutant fibroblasts. *Annals of Neurology*, 64(5), pp.555–565.

Murphy, Á.C. et al., 2013. Activation of executioner caspases is a predictor of progression-free survival in glioblastoma patients: a systems medicine approach. *Cell death & disease*, 4, p.e629.

Narendra, D. et al., 2008. Parkin is recruited selectively to impaired mitochondria and promotes their autophagy. *The Journal of cell biology*, 183(5), pp.795–803.

Newman, E.A., 2003. New roles for astrocytes: Regulation of synaptic transmission. *Trends in Neurosciences*, 26(10), pp.536–542.

Oliva, C.R. et al., 2011. Acquisition of chemoresistance in gliomas is associated with increased mitochondrial coupling and decreased ROS production. *PLoS ONE*, 6(9), pp.9–13.

Palmer, C.S. et al., 2011. The regulation of mitochondrial morphology: Intricate mechanisms and dynamic machinery. *Cellular Signalling*, 23(10), pp.1534–1545.

Park, J.M. et al., 2013. Metabolic response of glioma to dichloroacetate measured in vivo by spectroscopic imaging. *Neuro-Oncology*, 15(4), pp.433–441.

Pasdois, P. et al., 2003. Contribution of the Phosphorylable Complex I in the Growth Phase-Dependent Respiration of C6 Glioma Cells in Vitro. *Journal of Bioenergetics and Biomembranes*, 35(5), pp.439–450.

Pattingre, S. et al., 2005. Bcl-2 antiapoptotic proteins inhibit Beclin 1-dependent autophagy. *Cell*, 122(6), pp.927–939.

Perea, G., Navarrete, M. & Araque, A., 2009. Tripartite synapses: astrocytes process and control synaptic information. *Trends in Neurosciences*, 32(8), pp.421–431.

Pich, S. et al., 2005. The Charcot-Marie-Tooth type 2A gene product, Mfn2, up-regulates fuel oxidation through expression of OXPHOS system. *Human molecular genetics*, 14(11), pp.1405–1415.

Plate, K.H. et al., 1992. Vascular endothelial growth factor is a potential tumour angiogenesis factor in human gliomas in vivo. *Nature*, 359(6398), pp.845–848.

Rangwala, R., Chang, Y.C., et al., 2014. Combined MTOR and autophagy inhibition: Phase I trial of hydroxychloroquine and temsirolimus in patients with advanced solid tumors and melanoma. *Autophagy*, 10(8), pp.1391–1402.

Rangwala, R., Chang, Y.C., et al., 2014. Combined MTOR and autophagy inhibition: phase I trial of hydroxychloroquine and temsirolimus in patients with advanced solid tumors and melanoma. *Autophagy*, 10(8), pp.1391–1402.

Ransom, B., Behar, T. & Nedergaard, M., 2003. New roles for astrocytes (stars at last). *Trends in Neurosciences*, 26(10), pp.520–522.

Ravikumar, B. et al., 2010. Regulation of mammalian autophagy in physiology and pathophysiology. *Physiological reviews*, 90(4), pp.1383–435.

Ricci, J.E. et al., 2004. Disruption of mitochondrial function during apoptosis is mediated by caspase cleavage of the p75 subunit of complex I of the electron transport chain. *Cell*, 117(6), pp.773–786.

Riedl, S.J. & Salvesen, G.S., 2007. The apoptosome: signalling platform of cell death. *Nature reviews. Molecular cell biology*, 8(5), pp.405–413.

Rosenfeld, M.R. et al., 2014. A phase I/II trial of hydroxychloroquine in conjunction with radiation therapy and concurrent and adjuvant temozolomide in patients with newly diagnosed glioblastoma multiforme. *Autophagy*, 10(8), pp.1359–68.

Rossignol, R. et al., 2004. Energy substrate modulates mitochondrial structure and oxidative capacity in cancer cells. *Cancer research*, 64(3), pp.985–993.

Saggioro, F.P. et al., 2014. Fas, FasL, and cleaved caspases 8 and 3 in glioblastomas: A tissue microarray-based study. *Pathology Research and Practice*, 210(5), pp.267–273.

Seyfried, T.N. et al., 2011. Metabolic management of brain cancer. *Biochimica et biophysica acta*, 1807(6), pp.577–594.

Seyfried, T.N. et al., 2015. Metabolic therapy: A new paradigm for managing malignant brain cancer. *Cancer Letters*, 356(2), pp.289–300.

Shimizu, S. et al., 2004. Role of Bcl-2 family proteins in a non-apoptotic programmed cell death dependent on autophagy genes. *Nature cell biology*, 6(12), pp.1221–1228.

Singh, R. & Cuervo, A.M., 2011. Autophagy in the cellular energetic balance. *Cell Metabolism*, 13(5), pp.495–504.

Soda, Y. et al., 2011. Transdifferentiation of glioblastoma cells into vascular endothelial cells. , 108(11).

Somjen, G.G., 1988. Nervenkitt: Notes on the history of the concept of neuroglia. *Glia*, 1(1), pp.2–9.

Sornette, D., 2000. *Critical phenomena in natural sciences : chaos, fractals, selforganization, and disorder : concepts and tools*, Berlin; New York: Springer.

Stupp, R. et al., 2009. Effects of radiotherapy with concomitant and adjuvant temozolomide versus radiotherapy alone on survival in glioblastoma in a randomised phase III study: 5-year analysis of the EORTC-NCIC trial. *The Lancet. Oncology*, 10(5), pp.459–466.

Twig, G. et al., 2008. Fission and selective fusion govern mitochondrial segregation and elimination by autophagy. *The EMBO Journal*, 27(2), pp.433–446.

Vannucci, S.J., Maher, F. & Simpson, I.A., 1997. Glucose transporter proteins in brain: Delivery of glucose to neurons and glia. *Glia*, 21(1), pp.2–21.

Wanka, C., Steinbach, J.P. & Rieger, J., 2012. Tp53-induced glycolysis and apoptosis regulator (TIGAR) protects glioma cells from starvation-induced cell death by up-regulating respiration and improving cellular redox homeostasis. *Journal of Biological Chemistry*, 287(40), pp.33436–33446.

Warburg, O., 1956. On the Origin of Cancer Cells. *Science*, 123(3191), pp.309–314.

Wen, P.Y. & Kesari, S., 2008. Malignant gliomas in . *The New England journal of medicine*, 359(5), pp.492–507.

Wesseling, P., Kros, J.M. & Jeuken, J.W.M., 2011. The pathological diagnosis of diffuse gliomas: Towards a smart synthesis of microscopic and molecular information in a multidisciplinary context. *Diagnostic Histopathology*, 17(11), pp.486–494.

Wilhelmsson, U. et al., 2006. Redefining the concept of reactive astrocytes as cells that remain within their unique domains upon reaction to injury. *Proceedings of the National Academy of Sciences of the United States of America*, 103(46), pp.17513–17518.

Yan, H. et al., 2009. Mutations in Gliomas. *New England Journal of Medicine*, 360(8), pp.765–773.

Yang, C. et al., 2009. Glioblastoma cells require glutamate dehydrogenase to survive impairments of glucose metabolism or Akt signaling. *Cancer research*, 69(20), pp.7986–93.

Yorimitsu, T. & Klionsky, D.J., 2005. Autophagy: molecular machinery for self-eating. *Cell death and differentiation*, 12 Suppl 2(Suppl 2), pp.1542–52.

Youle, R.J. & Strasser, A., 2008. The BCL-2 protein family: opposing activities that mediate cell death. *Nature Reviews Molecular Cell Biology*, 9(1), pp.47–59.

Yu, T., Robotham, J.L. & Yoon, Y., 2006. Increased production of reactive oxygen species in hyperglycemic conditions requires dynamic change of mitochondrial morphology. *Proceedings of the National Academy of Sciences of the United States of America* , 103 (8), pp.2653–2658.

Zhang, L. et al., 2015. FTY720 induces autophagy-related apoptosis and necroptosis in human glioblastoma cells. *Toxicology Letters*, 236(1), pp.43–59.

Zheng, H. et al., 2008. p53 and Pten control neural and glioma stem/progenitor cell renewal and differentiation. *Nature*, 455(7216), pp.1129–33.

Zhou, S. et al., 2012. Autophagy in tumorigenesis and cancer therapy: Dr. Jekyll or Mr. Hyde? *Cancer Letters*, 323(2), pp.115–127.

Zou, Y. et al., 2014. Temozolomide induces autophagy via ATM-AMPK-ULK1 pathways in glioma. *Molecular Medicine Reports*, 10(1), pp.411–416.

Aki, T. et al., 2013. Impairment of autophagy: From hereditary disorder to drug intoxication. *Toxicology*, 311(3), pp.205–215.

Amaravadi, R.K. et al., 2011. Principles and current strategies for targeting autophagy for cancer treatment. *Clinical Cancer Research*, 17(4), pp.654–666.

Amaravadi, R.K. & Thompson, C.B., 2007. The roles of therapy-induced autophagy and necrosis in cancer treatment. *Clinical Cancer Research*, 13(24), pp.7271–7279.

Araque, A. et al., 1999. Tripartite synapses: Glia, the unacknowledged partner. *Trends in Neurosciences*, 22(5), pp.208–215.

Arcella, A. et al., 2013. Rapamycin inhibits the growth of glioblastoma. *Brain Research*, 1495, pp.37–51.

Arias, E. & Cuervo, A.M., 2011. Chaperone-mediated autophagy in protein quality control. *Current opinion in cell biology*, 23(2), pp.184–189.

Benard, G. & Karbowski, M., 2009. Mitochondrial fusion and division: Regulation and role in cell viability. *Seminars in cell & developmental biology*, 20(3), pp.365–374.

Bouchier-Hayes, L. et al., 2008. Measuring apoptosis at the single cell level. *Methods*, 44(3), pp.222–228.

Boya, P. et al., 2005. Inhibition of macroautophagy triggers apoptosis. *Molecular and cellular biology*, 25(3), pp.1025–1040.

Bradford, M.M., 1976. A rapid and sensitive method for the quantitation of microgram quantities of protein utilizing the principle of protein-dye binding. *Analytical Biochemistry*, 72(1-2), pp.248–254.

Bushong, E. a et al., 2002. Protoplasmic astrocytes in CA1 stratum radiatum occupy separate anatomical domains. *The Journal of neuroscience : the official journal of the Society for Neuroscience*, 22(1), pp.183–192.

Chang, C.-R. & Blackstone, C., 2007. Cyclic AMP-dependent protein kinase phosphorylation of Drp1 regulates its GTPase activity and mitochondrial morphology. *The Journal of biological chemistry*, 282(30), pp.21583–7.

Chen, H. et al., 2003. Mitofusins Mfn1 and Mfn2 coordinately regulate mitochondrial fusion and are essential for embryonic development. *Journal of Cell Biology*, 160(2), pp.189–200.

Deighton, R.F. et al., 2014. Interactions among mitochondrial proteins altered in glioblastoma. *Journal of Neuro-Oncology*, 118(2), pp.247–256.

Devin, A. & Rigoulet, M., 2007. Mechanisms of mitochondrial response to variations in energy demand in eukaryotic cells. *American Journal of Physiology - Cell Physiology*, 292(1), p.C52 LP – C58.

Dixon, S.J. et al., 2016. Ferroptosis: An Iron-Dependent Form of Nonapoptotic Cell Death. *Cell*, 149(5), pp.1060–1072.

Dunn, G.P. et al., 2012. Emerging insights into the molecular and cellular basis of glioblastoma. , pp.756–784.

De Duve, C. & Wattiaux, R., 1966. Functions of lysosomes. *Annual review of physiology*, 28, pp.435–492.

Edinger, A.L. & Thompson, C.B., 2002. Akt Maintains Cell Size and Survival by Increasing mTOR-dependent Nutrient Uptake M. Raff, ed. *Molecular Biology of the Cell*, 13(7), pp.2276–2288.

Engelman, J.A., Luo, J. & Cantley, L.C., 2006. The evolution of phosphatidylinositol 3-kinases as regulators of growth and metabolism. *Nature reviews. Genetics*, 7(8), pp.606–619.

Esteller, M., 2008. Epigenetics in cancer. *The New England journal of medicine*, 358(11), pp.1148–1159.

Galeffi, F. & Turner, D.A., 2012. Exploiting metabolic differences in glioma therapy. *Current drug discovery technologies*, 9(4), pp.280–293.

Galloway, C.A., Lee, H. & Yoon, Y., 2012. Mitochondrial morphology-emerging role in bioenergetics. *Free Radical Biology and Medicine*, 53(12), pp.2218–2228.

Galluzzi, L. et al., 2014. Metabolic control of autophagy. *Cell*, 159(6), pp.1263–76.

Galluzzi, L. et al., 2010. Mitochondrial gateways to cancer. *Molecular Aspects of Medicine*, 31(1), pp.1–20.

Galluzzi, L., Kepp, O. & Kroemer, G., 2016. Mitochondrial regulation of cell death: a phylogenetically conserved control. *Microbial Cell*, 3(3), pp.101–108.

Gomes, L.C., Di Benedetto, G. & Scorrano, L., 2011. During autophagy mitochondria elongate, are spared from degradation and sustain cell viability. *Nature cell biology*, 13(5), pp.589–98.

Gong, C. et al., 2012. Beclin 1 and autophagy are required for the tumorigenicity of breast cancer stem-like/progenitor cells. *Oncogene*, (June 2012), pp.2261–2272.

González-Polo, R.-A. et al., 2005. The apoptosis/autophagy paradox: autophagic vacuolization before apoptotic death. *Journal of cell science*, 118(14), pp.3091–3102.

Green, D.R., Galluzzi, L. & Kroemer, G., 2014. Metabolic control of cell death. *Science*, 345(6203), pp.1250256–1250256.

Green, D.R. & Levine, B., 2014. To be or not to be? How selective autophagy and cell death govern cell fate. *Cell*, 157(1), pp.65–75.

Griguer, C.E. et al., 2013. Prognostic Relevance of Cytochrome c Oxidase in Primary Glioblastoma Multiforme. *PLoS ONE*, 8(4), pp.8–13.

Guillery, O. et al., 2008. Metalloprotease-mediated OPA1 processing is modulated by the mitochondrial membrane potential. *Biology of the cell / under the auspices of the European Cell Biology Organization*, 100(5), pp.315–325.

Hegi, M.E. et al., 2005. MGMT gene silencing and benefit from temozolomide in glioblastoma. *The New England journal of medicine*, 352(10), pp.997–1003.

Hermisson, M. et al., 2006. O6-methylguanine DNA methyltransferase and p53 status predict temozolomide sensitivity in human malignant glioma cells. *Journal of neurochemistry*, 96(3), pp.766–776.

Hertz, L., Peng, L. & Dienel, G. a, 2007. Energy metabolism in astrocytes: high rate of oxidative metabolism and spatiotemporal dependence on glycolysis/glycogenolysis. *Journal of cerebral blood flow and metabolism : official journal of the International Society of Cerebral Blood Flow and Metabolism*, 27(2), pp.219–249.

Ibebuike, K., Ouma, J. & Gopal, R., 2013. Meningiomas Among Intracranial Neoplasm in Johannesburg, South Africa: Prevalence, Clinical Observations and Review of the Literature. *African Health Sciences*, 13(1), pp.118–121.

Ishihara, N. et al., 2009. Mitochondrial fission factor Drp1 is essential for embryonic development and synapse formation in mice. *Nature cell biology*, 11(8), pp.958–966.

Jose, C., Bellance, N. & Rossignol, R., 2011. Choosing between glycolysis and oxidative phosphorylation: A tumor’s dilemma? *Biochimica et Biophysica Acta - Bioenergetics*, 1807(6), pp.552–561.

Kanzawa, T. et al., 2004. Role of autophagy in temozolomide-induced cytotoxicity for malignant glioma cells. *Cell death and differentiation*, 11(4), pp.448–457.

Karantza-Wadsworth, V. et al., 2007. Autophagy mitigates metabolic stress and genome damage in mammary tumorigenesis. *Genes and Development*, 21(13), pp.1621–1635.

Karbowski, M. et al., 2004. Quantitation of mitochondrial dynamics by photolabeling of individual organelles shows that mitochondrial fusion is blocked during the Bax activation phase of apoptosis. *Journal of Cell Biology*, 164(4), pp.493–499.

Karbowski, M., Neutzner, A. & Youle, R.J., 2007. The mitochondrial E3 ubiquitin ligase MARCH5 is required for Drp1 dependent mitochondrial division. *Journal of Cell Biology*, 178(1), pp.71–84.

Kennedy, C.R. et al., 2013. Differential sensitivities of glioblastoma cell lines towards metabolic and signaling pathway inhibitions. *Cancer Letters*, 336(2), pp.299–306.

Kitange, G.J. et al., 2009. Induction of MGMT expression is associated with temozolomide resistance in glioblastoma xenografts. *Neuro-oncology*, 11(3), pp.281–91.

Komatsu, M. & Ichimura, Y., 2010. Physiological significance of selective degradation of p62 by autophagy. *FEBS Lett*, 584(7), pp.1374–1378.

Kroemer, G., Mari??o, G. & Levine, B., 2010. Autophagy and the Integrated Stress Response. *Molecular Cell*, 40(2), pp.280–293.

Larsen, S. et al., 2012. Biomarkers of mitochondrial content in skeletal muscle of healthy young human subjects. *The Journal of physiology*, 590(Pt 14), pp.3349–60.

Lefranc, F. & Kiss, R., 2006. Autophagy, the Trojan horse to combat glioblastomas. *Neurosurgical focus*, 20(4), p.E7.

Liesa, M. & Shirihai, O.S., 2013. Mitochondrial dynamics in the regulation of nutrient utilization and energy expenditure. *Cell Metabolism*, 17(4), pp.491–506.

Lin, G. et al., 2014. Dichloroacetate induces autophagy in colorectal cancer cells and tumours. *British journal of cancer*, 111(2), pp.375–85.

Liu, X. et al., 2009. Mitochondrial “kiss-and-run”: interplay between mitochondrial motility and fusion-fission dynamics. *The EMBO Journal*, 28(20), pp.3074–3089.

Liu, Y. & Levine, B., 2015. Autosis and autophagic cell death: the dark side of autophagy. *Cell death and differentiation*, 22(3), pp.367–76.

Loos, B. et al., 2013. The variability of autophagy and cell death susceptibility: Unanswered questions. *Autophagy*, 9(9), pp.1270–1285.

Loos, B. & Engelbrecht, A.-M., 2009. Cell death: a dynamic response concept. *Autophagy*, 5(5), pp.590–603.

Loos, B., du Toit, A. & Hofmeyr, J.-H.S., 2014. Defining and measuring autophagosome flux—concept and reality. *Autophagy*, 10(11), pp.2087–96.

Losón, O.C. et al., 2013. Fis1, Mff, MiD49, and MiD51 mediate Drp1 recruitment in mitochondrial fission. *Molecular Biology of the Cell*, 24(5), pp.659–667.

Maher, E.A. et al., 2012. Metabolism of [U-13 C]glucose in human brain tumors in vivo. *NMR in biomedicine*, 25(11), pp.1234–1244.

Maiuri, M.C. et al., 2009. Stimulation of autophagy by the p53 target gene Sestrin2. *Cell cycle (Georgetown, Tex.)*, 8(10), pp.1571–1576.

Manning, B.D. & Cantley, L.C., 2007. AKT/PKB Signaling: Navigating Downstream. *Cell*, 129(7), pp.1261–1274.

Marin-Valencia, I. et al., 2012. Analysis of tumor metabolism reveals mitochondrial glucose oxidation in genetically diverse human glioblastomas in the mouse brain in vivo. *Cell metabolism*, 15(6), pp.827–37.

Mathew, R., Karantza-Wadsworth, V. & White, E., 2007. Role of autophagy in cancer. *Nature reviews. Cancer*, 7(12), pp.961–7.

Mathew, R. & White, E., 2011. Autophagy, stress, and cancer metabolism: What doesn't kill you makes you stronger. *Cold Spring Harbor Symposia on Quantitative Biology*, 76, pp.389–396.

Matsuda, N. et al., 2010. PINK1 stabilized by mitochondrial depolarization recruits Parkin to damaged mitochondria and activates latent Parkin for mitophagy. *Journal of Cell Biology*, 189(2), pp.211–221.

Michelakis, E.D. et al., 2010. Metabolic Modulation of Glioblastoma with Dichloroacetate. *Science Translational Medicine*, 2(31), p.31ra34 LP – 31ra34.

Mihaylova, M.M. & Shaw, R.J., 2011. The AMPK signalling pathway coordinates cell growth, autophagy and metabolism. *Nature cell biology*, 13(9), pp.1016–1023.

Miracco, C. et al., 2007. Protein and mRNA expression of autophagy gene Beclin 1 in human brain tumours. *International journal of oncology*, 30(2), pp.429–436.

Mishra, P. et al., 2014. Proteolytic cleavage of Opa1 stimulates mitochondrial inner membrane fusion and couples fusion to oxidative phosphorylation. *Cell Metabolism*, 19(4), pp.630–641.

MITCHELL, P., 1961. Coupling of Phosphorylation to Electron and Hydrogen Transfer by a Chemi-Osmotic type of Mechanism. *Nature*, 191(4784), pp.144–148.

Mizushima, N. et al., 2004. In vivo analysis of autophagy in response to nutrient starvation using transgenic mice expressing a fluorescent autophagosome marker. *Molecular biology of the cell*, 15(3), pp.1101–1111.

Mizushima, N. & Klionsky, D.J., 2007. Protein turnover via autophagy: implications for metabolism. *Annual Review of Nutrition*, 27, pp.19–40.

Mortiboys, H. et al., 2008. Mitochondrial function and morphology are impaired in parkin-mutant fibroblasts. *Annals of Neurology*, 64(5), pp.555–565.

Murphy, Á.C. et al., 2013. Activation of executioner caspases is a predictor of progression-free survival in glioblastoma patients: a systems medicine approach. *Cell death & disease*, 4, p.e629.

Narendra, D. et al., 2008. Parkin is recruited selectively to impaired mitochondria and promotes their autophagy. *The Journal of cell biology*, 183(5), pp.795–803.

Newman, E.A., 2003. New roles for astrocytes: Regulation of synaptic transmission. *Trends in Neurosciences*, 26(10), pp.536–542.

Oliva, C.R. et al., 2011. Acquisition of chemoresistance in gliomas is associated with increased mitochondrial coupling and decreased ROS production. *PLoS ONE*, 6(9), pp.9–13.

Palmer, C.S. et al., 2011. The regulation of mitochondrial morphology: Intricate mechanisms and dynamic machinery. *Cellular Signalling*, 23(10), pp.1534–1545.

Park, J.M. et al., 2013. Metabolic response of glioma to dichloroacetate measured in vivo by spectroscopic imaging. *Neuro-Oncology*, 15(4), pp.433–441.

Pasdois, P. et al., 2003. Contribution of the Phosphorylable Complex I in the Growth Phase-Dependent Respiration of C6 Glioma Cells in Vitro. *Journal of Bioenergetics and Biomembranes*, 35(5), pp.439–450.

Pattingre, S. et al., 2005. Bcl-2 antiapoptotic proteins inhibit Beclin 1-dependent autophagy.

Cell, 122(6), pp.927–939.

Perea, G., Navarrete, M. & Araque, A., 2009. Tripartite synapses: astrocytes process and control synaptic information. *Trends in Neurosciences*, 32(8), pp.421–431.

Pich, S. et al., 2005. The Charcot-Marie-Tooth type 2A gene product, Mfn2, up-regulates fuel oxidation through expression of OXPHOS system. *Human molecular genetics*, 14(11), pp.1405–1415.

Plate, K.H. et al., 1992. Vascular endothelial growth factor is a potential tumour angiogenesis factor in human gliomas in vivo. *Nature*, 359(6398), pp.845–848.

Rangwala, R., Chang, Y.C., et al., 2014. Combined MTOR and autophagy inhibition: Phase I trial of hydroxychloroquine and temsirolimus in patients with advanced solid tumors and melanoma. *Autophagy*, 10(8), pp.1391–1402.

Rangwala, R., Chang, Y.C., et al., 2014. Combined MTOR and autophagy inhibition: phase I trial of hydroxychloroquine and temsirolimus in patients with advanced solid tumors and melanoma. *Autophagy*, 10(8), pp.1391–1402.

Ransom, B., Behar, T. & Nedergaard, M., 2003. New roles for astrocytes (stars at last). *Trends in Neurosciences*, 26(10), pp.520–522.

Ravikumar, B. et al., 2010. Regulation of mammalian autophagy in physiology and pathophysiology. *Physiological reviews*, 90(4), pp.1383–435.

Ricci, J.E. et al., 2004. Disruption of mitochondrial function during apoptosis is mediated by caspase cleavage of the p75 subunit of complex I of the electron transport chain. *Cell*, 117(6), pp.773–786.

Riedl, S.J. & Salvesen, G.S., 2007. The apoptosome: signalling platform of cell death. *Nature reviews. Molecular cell biology*, 8(5), pp.405–413.

Rosenfeld, M.R. et al., 2014. A phase I/II trial of hydroxychloroquine in conjunction with radiation therapy and concurrent and adjuvant temozolomide in patients with newly diagnosed glioblastoma multiforme. *Autophagy*, 10(8), pp.1359–68.

Rossignol, R. et al., 2004. Energy substrate modulates mitochondrial structure and oxidative capacity in cancer cells. *Cancer research*, 64(3), pp.985–993.

Saggioro, F.P. et al., 2014. Fas, FasL, and cleaved caspases 8 and 3 in glioblastomas: A tissue microarray-based study. *Pathology Research and Practice*, 210(5), pp.267–273.

Seyfried, T.N. et al., 2011. Metabolic management of brain cancer. *Biochimica et biophysica acta*, 1807(6), pp.577–594.

Seyfried, T.N. et al., 2015. Metabolic therapy: A new paradigm for managing malignant brain cancer. *Cancer Letters*, 356(2), pp.289–300.

Shimizu, S. et al., 2004. Role of Bcl-2 family proteins in a non-apoptotic programmed cell death dependent on autophagy genes. *Nature cell biology*, 6(12), pp.1221–1228.

Singh, R. & Cuervo, A.M., 2011. Autophagy in the cellular energetic balance. *Cell Metabolism*, 13(5), pp.495–504.

Soda, Y. et al., 2011. Transdifferentiation of glioblastoma cells into vascular endothelial cells. , 108(11).

Somjen, G.G., 1988. Nervenkitt: Notes on the history of the concept of neuroglia. *Glia*, 1(1), pp.2–9.

Sornette, D., 2000. *Critical phenomena in natural sciences : chaos, fractals, selforganization, and disorder : concepts and tools*, Berlin; New York: Springer.

Stupp, R. et al., 2009. Effects of radiotherapy with concomitant and adjuvant temozolomide versus radiotherapy alone on survival in glioblastoma in a randomised phase III study: 5-year analysis of the EORTC-NCIC trial. *The Lancet. Oncology*, 10(5), pp.459–466.

Twig, G. et al., 2008. Fission and selective fusion govern mitochondrial segregation and elimination by autophagy. *The EMBO Journal*, 27(2), pp.433–446.

Vannucci, S.J., Maher, F. & Simpson, I.A., 1997. Glucose transporter proteins in brain: Delivery of glucose to neurons and glia. *Glia*, 21(1), pp.2–21.

Wanka, C., Steinbach, J.P. & Rieger, J., 2012. Tp53-induced glycolysis and apoptosis regulator (TIGAR) protects glioma cells from starvation-induced cell death by up-regulating respiration and improving cellular redox homeostasis. *Journal of Biological Chemistry*, 287(40), pp.33436–33446.

Warburg, O., 1956. On the Origin of Cancer Cells. *Science*, 123(3191), pp.309–314.

Wen, P.Y. & Kesari, S., 2008. Malignant gliomas in . *The New England journal of medicine*, 359(5), pp.492–507.

Wesseling, P., Kros, J.M. & Jeuken, J.W.M., 2011. The pathological diagnosis of diffuse gliomas: Towards a smart synthesis of microscopic and molecular information in a multidisciplinary context. *Diagnostic Histopathology*, 17(11), pp.486–494.

Wilhelmsson, U. et al., 2006. Redefining the concept of reactive astrocytes as cells that remain within their unique domains upon reaction to injury. *Proceedings of the National Academy of Sciences of the United States of America*, 103(46), pp.17513–17518.

Yan, H. et al., 2009. Mutations in Gliomas. *New England Journal of Medicine*, 360(8), pp.765–773.

Yang, C. et al., 2009. Glioblastoma cells require glutamate dehydrogenase to survive impairments of glucose metabolism or Akt signaling. *Cancer research*, 69(20), pp.7986–93.

Yorimitsu, T. & Klionsky, D.J., 2005. Autophagy: molecular machinery for self-eating. *Cell death and differentiation*, 12 Suppl 2(Suppl 2), pp.1542–52.

Youle, R.J. & Strasser, A., 2008. The BCL-2 protein family: opposing activities that mediate cell death. *Nature Reviews Molecular Cell Biology*, 9(1), pp.47–59.

Yu, T., Robotham, J.L. & Yoon, Y., 2006. Increased production of reactive oxygen species in hyperglycemic conditions requires dynamic change of mitochondrial morphology. *Proceedings of the National Academy of Sciences of the United States of America* , 103 (8), pp.2653–2658.

Zhang, L. et al., 2015. FTY720 induces autophagy-related apoptosis and necroptosis in human glioblastoma cells. *Toxicology Letters*, 236(1), pp.43–59.

Zheng, H. et al., 2008. p53 and Pten control neural and glioma stem/progenitor cell renewal and differentiation. *Nature*, 455(7216), pp.1129–33.

Zhou, S. et al., 2012. Autophagy in tumorigenesis and cancer therapy: Dr. Jekyll or Mr. Hyde? *Cancer Letters*, 323(2), pp.115–127.

Zou, Y. et al., 2014. Temozolomide induces autophagy via ATM-AMPK-ULK1 pathways in glioma. *Molecular Medicine Reports*, 10(1), pp.411–416.

Appendix A

Supplementary Results

A1. Cell Permeabilisation

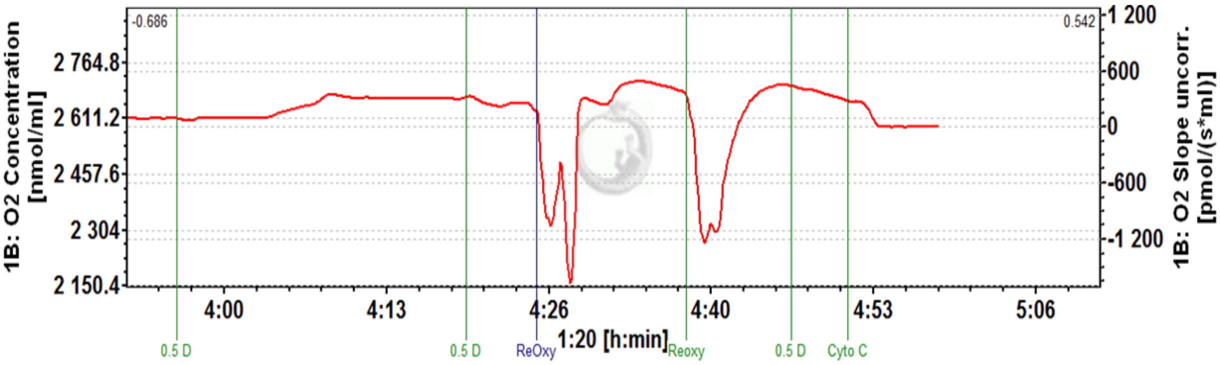

Fig. S1. Cell Permeabilisation. Determination of the concentration of Digitonin to achieve non-lethal cell permeabilisation. After 2 0.5mM Digitonin titrations, reoxygenation of the O2K chambers was required (Reoxy). After the third 0.5 mM Digitonin titration, 1mM Cytochrome C (Cyto C) was added. Seeing as stabilisation occurred, and not a dramatic increase in O_2 consumption flux, 1.5mM was deemed a safe permeabilising concentration.

A2. Photoactivation

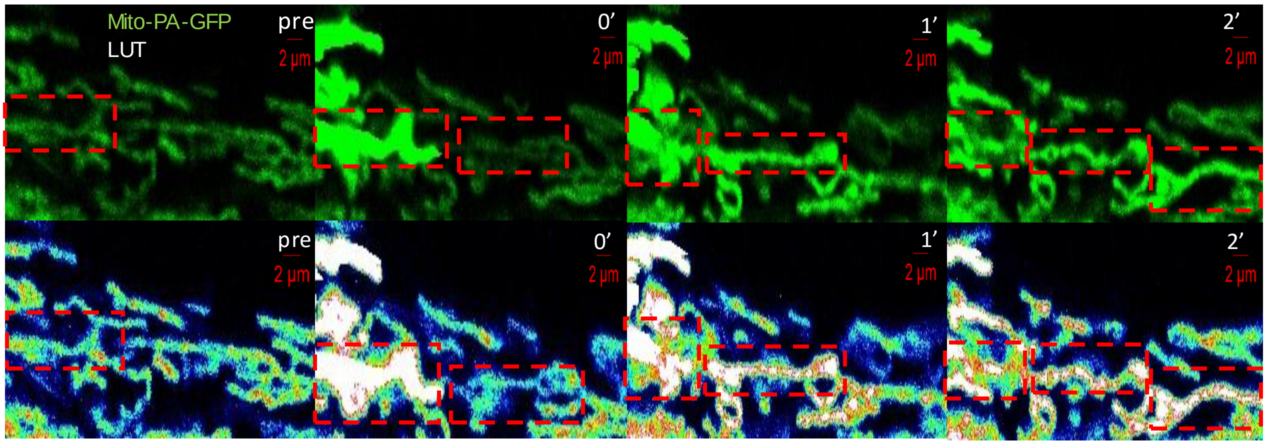

Fig. S2. Representative images of mito-PA-GFP transfer with corresponding look up table (LUT) intensities as a result of fusion events. Initial region of interest (ROI) signal intensity pre-activation was 90,41 (Pre). Following photoactivation, an increase in signal intensity was observed for the ROI (207,35 at time of activation/0 minutes), with the neighbouring region remaining 80.00. 1 min post-activation, spread of signal intensity was observed, with intensity values of 158,00 for the initial activated region and 128,92 for the neighbouring region. 2 min post activation, further transfer of signal intensity was observed, with intensity values of 133,59, 108,623 and 119,49 for the three ROIs respectively.

A3. Image Processing Functions

```
MorphoBin[imagelist_] := Table[MorphologicalBinarize[imagelist[[i]]],
  {i, 1, Length[imagelist]}]

ClusterCount[imagelist_] :=
 Table[Max[ComponentMeasurements[imagelist[[i]], "Count"][[All, 1]]],
  {i, 1, Length[imagelist]}]

ClusterAreas[imagelist_] :=
 Table[ComponentMeasurements[imagelist[[i]], "Count"][[All, 2]],
  {i, 1, Length[imagelist]}]

ClusterPerimeters1[imagelist_] :=
 Table[ComponentMeasurements[imagelist[[i]], "PerimeterLength"][[All, 2]],
  {i, 1, Length[imagelist]}]

ClusterPerimeters2[imagelist_] :=
 Table[ComponentMeasurements[imagelist[[i]], "PerimeterCount"][[All, 2]],
  {i, 1, Length[imagelist]}]

AreasAndPerimeters[imagelist_] :=
 Table[
  Transpose[Table[{ClusterAreas[imagelist][[i]], ClusterPerimeters2[imagelist][[i]]},
     {i, 1, Length[imagelist]}][[j]]], {j, 1, Length[imagelist]}]

ExtractLargestClusters[imagelist_, n_] :=
 Module[{distinctarealist = DistinctOrderedAreas[imagelist]},
  Table[SelectComponents[imagelist[[i]], "Count",
    # ≥ Reverse[distinctarealist[[i]]][[n]] &], {i, 1, Length[imagelist]}]]

Clear[DeleteSmallestClusters]

DeleteSmallestClusters1[imagelist_, n_] :=
 Module[{distinctarealist = DistinctOrderedAreas[imagelist]},
  Table[SelectComponents[imagelist[[i]], "Count", # > distinctarealist[[i]][[n]] &],
   {i, 1, Length[imagelist]}]]

DeleteSmallestClusters2[imagelist_, n_] :=
 Module[{distinctarealist = DistinctOrderedAreas[imagelist]},
  Table[SelectComponents[imagelist[[i]], "Count", # > n &], {i, 1, Length[imagelist]}]]

DeleteLargestClusters2[imagelist_, n_] :=
 Module[{distinctarealist = DistinctOrderedAreas[imagelist]},
  Table[SelectComponents[imagelist[[i]], "Count", # < n &], {i, 1, Length[imagelist]}]]


MakeMorphoGraph[imagelist_] :=
  Table[MorphologicalGraph[imagelist[[i]]], {i, 1, Length[imagelist]}];

GetConnectedComponents[imagelist_] :=
 Table[Length[ConnectedComponents[MorphologicalGraph[Thinning[imagelist[[i]]]]]],
  {i, 1, Length[imagelist]}]

CountVertices[graphlist_] :=
 Table[VertexCount[graphlist[[i]]], {i, 1, Length[graphlist]}]
```